Effects of upscaling and interpolation on log data.

Roger Bakke

Cand. Scient. thesis
Institutt for den faste jords fysikk
Universitetet i Bergen

March 2000

WORDS TO THE EXPLORER

There is a mine for silver and a place where gold is refined. Iron is taken from the earth, and copper is smelted from ore.

Man puts an end to the darkness; he searches the farthest recesses for ore in the blackest darkness. Far from where people dwell he cuts a shaft, in places forgotten by the foot of man; far from men he dangles and sways.

The earth, from which food comes, is transformed below as by fire; sapphires come from its rocks, and its dust contains nuggets of gold.

No bird of prey knows that hidden path, no falcon's eye has seen it. Proud beasts do not set foot on it, and no lion prowls there.

Man's hand assaults the flinty rock and lays bare the roots of the mountains. He tunnels through the rock; his eyes see all its treasures. He searches the sources of the rivers and brings hidden things to light.

But where can wisdom be found? Where does understanding dwell?

Job, ancient Hebrew

Preface

This thesis was written as part of my Cand. Scient. study at Institute of solid earth physics at the University of Bergen

I would like to thank a few great people who have helped me a lot in my work towards the completion of this thesis. Especially I want to thank my advisor at the institute, Tor Arne Johansen, for all the advice, help, support and patience during this period. I would also like to thank Åsmund Drottning for useful help on the required programming, and André Friis for help with running the FD-modelling. Also a great salute to fellow students at the institute for good memories.

To my friends who may not have seen me around that much lately: Thank you for your patience too! And finally: Thanks to my family for always being there!

Now as spring approaches, I will say with Bjørnson:

"Jeg velger meg april!"

Roger Bakke
Bergen, March 2000

Contents

Chapter 1

Introduction

Heterogeneities are found at all scales in nature, and the mapping of heterogeneities and the study of their effects on physical processes is a fundamental scientific activity. In geophysical prospecting, measured data is inverted to create a parameterized model, and this model can subsequently be applied in forward modelling for predicting data measurements (Menke, 1984). In popularized language, modelling may thus be regarded as the opposite procedure of data inversion. It is used to simulate processes found in nature based on the physical principles for the simulated process and a set of model parameters.

Wave propagation modelling is a principal and irreplacable tool for visualizing wave propagation and thus testing a model interpreted from real data. In petroleum geoscience, seismic data has traditionally been used primarily for geometric mapping of the extent and volume of possible hydrocarbon reservoirs. However, integration of rock physics modelling, where seismic parameters are calculated from physical rock parameters, also enables the modeller to study the seismic response of different quantifiable geologic properties such as sand – shale ratio, porosity, pore fluid composition and permeability. By perturbating such parameters and modelling the seismic response, a best fit to the measured seismic data can be found for such parameters. An increased understanding in this area of seismic modelling is required to develop effective and reliable methods for rock physics data inversion, recognized to have a great potential for improving the drilling success rate in petroleum industry.

In my thesis the focus will be on two main issues related to assigning property values to a spatial model utilized for seismic modelling. The first issue, which is discussed in chapter 3, is the topic of upscaling a small scale model representation, while the second issue, discussed in chapter 4, is that of interpolating between spatially confined data.

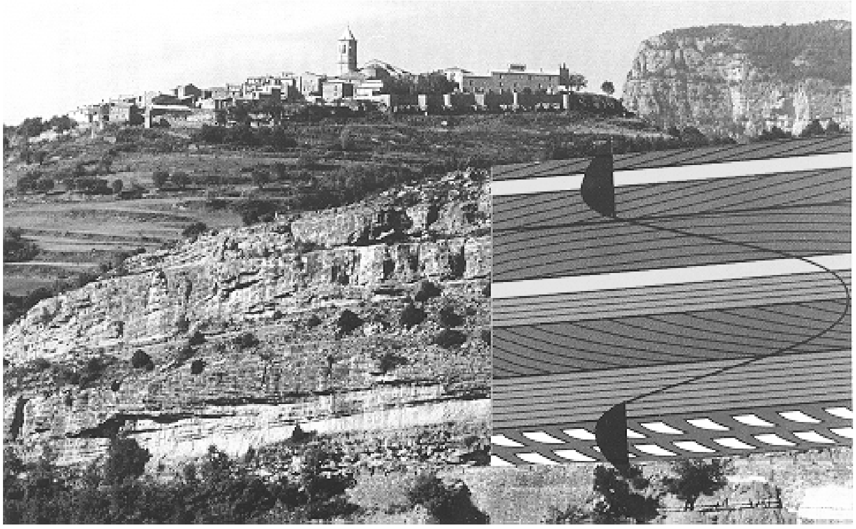

Figure 1.1: The issue of upscaling: Heterogeneous outcrop compared to scale of a seismic wave. (From Helbig, 1994)

The issue of property upscaling is illustrated by figure 1.1 (from Helbig, 1994) and is related to the different scales involved in the measurement. The minimum size of features of interest for geophysical mapping has decreased in scale as the resolution of seismic data has improved. From focusing on mapping large scale structures such as the divison of the earth into core, mantle and crust, now a great effort is put into the study of subtle and microscopic properties, important *e.g.* to optimize the oil production in stratigraphic reservoirs. In reservoir characterization the dimensions of individual heterogeneities are very small compared to the applied wavelength λ in a seismic study. Small scale heterogeneities may therefore not be discernable as distinct units. However, they may have joint effects on the measured wavefield that are detectable.

Effective medium theory states that a medium that displays property fluctuations when inspected on small scale, may behave like a nearly homogeneous media when measured on large scale, with the deterministic large scale properties given as functions of the local statistical averages of the small scale properties (Hudson, 1991).

Parameter upscaling thus involves mapping parameters from the small scale domain, where property values vary with high spatial frequencies, to a large scale domain that is more homogeneous and thus appropriate for efficient simulations of large scale processes. The objects upscaled in this thesis are well data logs, which are frequently provided with sampling density

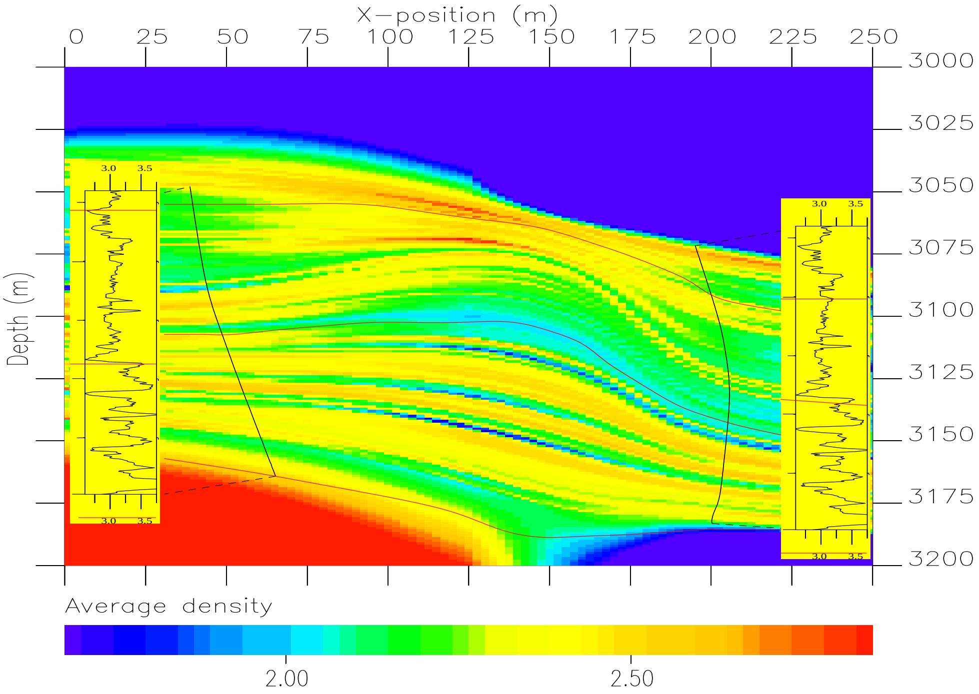

Figure 1.2: The issue of interpolation: Constructing spatial property models from field data and *a priori* information.

on the scale of decimeters. Since waves applied in seismic surveys often have wavelengths of tens of meters when they are probing the reservoir, it is of great interest to estimate the large scale properties of the well data. In this thesis I will interpret the log data as representing a thin-layered model, and I will consider different smoothing operations that may be applied to upscale such a model. One of these is the classic Backus smoothing (Backus, 1962), creating a transverse isotropic upscaled medium. I will simulate seismic wave propagation by finite difference modelling by using some of the small scale models and their associated upscaled medium versions, comparing the seismic response. Hence I will be able to make some conclusions regarding the validity of the different upscaling models.

The second issue of model parametrization, regarding aspects of parameter interpolation, is discussed in chapter 4 and illustrated by figure 1.2. When building a model, measured well data can be included in the model at the spatial locations where they are available. But well measurements are of course confined to the well trajectories, while the main objective of seismic mapping is to estimate how the parameters vary spatially *between* the wells. Forward modelling thus involves building a spatial model based on the available measurements in wells and necessarily also some *a priori* information regarding how these data are to be interpolated or extrapolated. Regarding the correlation geometry, the most frequent assumption is of course that the medium consists of horizontal strata, but other geometries should also be considered. In addition to the obvious effect related to different correlation geometries, effects will be considered related to the use of different interpolation functions to interpolate along these correlation lines between the wells.

Questions related to this last issue are, for example, what the effect on the resulting model is by linearly interpolating the seismic velocities versus interpolating the elastic constants, since these properties are related, and whether properties should be interpolated in the small scale or the small scale domain.

Preceding the two main chapters, my thesis contains a chapter 2 containing the fundamental elastic theory needed for describing wave propagation in a homogeneous and a thin-layered medium. This chapter also gives the theoretical basis for classifying the media used in the following chapters.

Rounding off my work, the most important conclusions from my observations in chapter 3 and 4 are stated in chapter 5, which is also brings some suggestions for further studies of the covered topics.

Chapter 2

Waves in homogeneous and thin-layered media

2.1 Introduction

Understanding the mechanisms and material properties related to wave propagation in a spatially invariant, *i.e.* a homogeneous, medium, is the fundamental basis for aquiring an understanding of seismic properties in more complex media. Such a medium is of course a simplification of any medium found in nature. Even sediments which to the naked eye look homogeneous, consist of packed grains of different minerals, grains which on the most microscopic level consist of crystals and atoms, being neither homogeneous nor continuous.

However, the overall behaviour of a small scale heterogeneous medium subjected to large scale waves can be described in terms of large scale properties which are locally homogeneous, socalled effective properties. The elastic properties and the related wave propagation behaviour in such an idealized effective medium is the focus of this chapter.

In the following, I will look at the fundamental elastic theory needed for describing wavepropagation in a completely elastic medium that is either homogeneous or thin-layered. The thread in this discourse starts at the definitions of stress and strain and ends at formulas describing how a wavefield excited from a point source spreads in a thin-layered medium.

Along this course, medium classification terms such as isotropy and transverse isotropy are explained, and the general elastic wave equation is presented and then solved for plane waves. From the solutions of this equation, and by observing how large scale properties of a thin-layered medium are related to the small scale constituents, the fundament for modelling a long

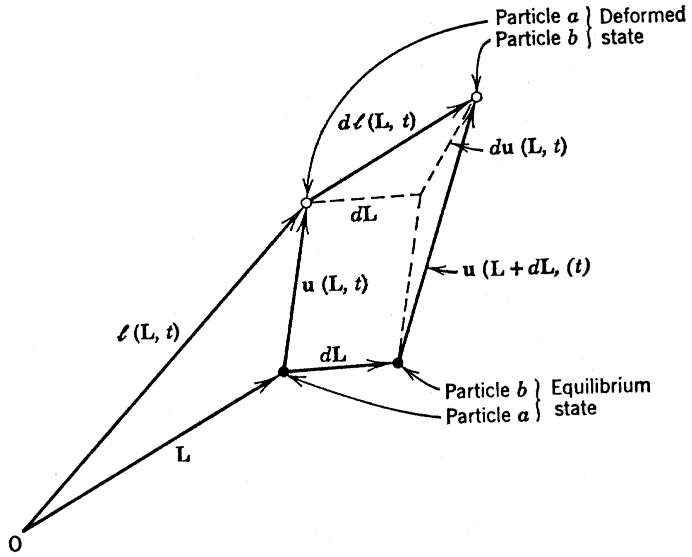

Figure 2.1: The defininition of differential particle displacement $d\mathbf{u}$ in a deformed medium. (From Auld, 1990).

wavelength elastic wave in a small scale layered medium is laid.

For a more in depth presentation of the given topics, see *e.g.* Auld (1990).

2.2 Principles of elasticity

2.2.1 Particle displacement and strain

The study of elastic waves is the study of time and space varying deformations in a continous matter. Forces applied to a particle with equilibrium position $\mathbf{L}$, gives it a particle displacement $\mathbf{u}\,(\mathbf{L}, t)$ from $\mathbf{L}$, giving it a new location $\mathbf{l}\,(\mathbf{L}, t)$. This displacement represents motion of rigid translation and rotation as well as deformation. To exclude the rigid translation, we consider the differential of $d\mathbf{u}$ for a fixed t, comparing the displacement of the particle with equilibrium point $\mathbf{L}$ with that of neigbouring particles with equilibrium points $\mathbf{L} + d\mathbf{L}$ (see figure (see figure 2.1), *i.e.*

$$d\mathbf{u}\,(\mathbf{L},t) = d\mathbf{l}\,(\mathbf{L},t) - d\mathbf{L} \tag{2.1}$$

In case of a rigid translation, this expression will vanish since the two differentials on the right hand side are equal. The explicit differential particle displacement in an orthogonal coordinate system where $\mathbf{u}\,(\mathbf{L},t) = \hat{\mathbf{x}}u_x+\hat{\mathbf{y}}u_y+\hat{\mathbf{z}}u_z$

is given by

$$d\mathbf{u} = \underbrace{\begin{bmatrix} \frac{\partial u_x}{\partial L_x} & \frac{\partial u_x}{\partial L_y} & \frac{\partial u_x}{\partial L_z} \\ \frac{\partial u_y}{\partial L_x} & \frac{\partial u_y}{\partial L_y} & \frac{\partial u_y}{\partial L_z} \\ \frac{\partial u_z}{\partial L_x} & \frac{\partial u_z}{\partial L_y} & \frac{\partial u_z}{\partial L_z} \end{bmatrix}}_{\varepsilon(\mathbf{L},t)} \begin{bmatrix} dL_x \\ dL_y \\ dL_z \end{bmatrix}. \tag{2.2}$$

$\varepsilon\left(\mathbf{L},t\right)$ in equation 2.2 is defined as the displacement gradient matrix, in symbolic notation written as $\varepsilon\left(\mathbf{L},t\right) = \nabla\mathbf{u}$. However, this displacement matrix does not separate between the effects of deformation and the effects of pure rotation. This separation is accomplished by defining the scalar deformation as the $\Delta' = dl^2\left(\mathbf{L},t\right) - \left(dL\right)^2$. It can be showed that (Auld, 1990)

$$\Delta'\left(\mathbf{L},t\right) = 2S_{ij}\left(\mathbf{L},t\right)dL_i dL_j, \tag{2.3}$$

with $[S]$ defined as strain:

$$S_{ij}\left(\mathbf{L},t\right) = \frac{1}{2}\left(\frac{\partial u_i}{\partial L_j} + \frac{\partial u_j}{\partial L_i} + \frac{\partial u_k}{\partial L_i}\frac{\partial u_k}{\partial L_j}\right), i,j,k = x,y,z, \tag{2.4}$$

where repeated indices imply summation[1]. When the displacement gradient is small, a linear approximation of the deformation is sufficient; cancelling all negligible quadratic and higher terms in S leads to

$$S_{ij} = \frac{1}{2}\left(\frac{\partial u_i}{\partial L_j} + \frac{\partial u_j}{\partial L_i}\right). \tag{2.5}$$

Following the same idea of linear approximation, the distinction between the equilibrium point vector $\mathbf{L}$ and the vector $\mathbf{l}$ representing the position of the deformed material when calculating the differentials can be neglected.

By decomposing the displacement gradient matrix into its symmetric and its antisymmetric part,

$$[\mathcal{E}] = \underbrace{\frac{1}{2}\left([\mathcal{E}] + \widetilde{[\mathcal{E}]}\right)}_{\text{symmetric}} + \underbrace{\frac{1}{2}\left([\mathcal{E}] - \widetilde{[\mathcal{E}]}\right)}_{\text{antisymmetric}}, \tag{2.6}$$

it can be shown that the symmetric part of $[\mathcal{E}]$ is equivalent with the linear approximation of $[S]$, while the antisymmetric part of the matrix gives a description of the rotational component of the differential displacement. In symbolic writing, strain defined as the symmetric part of the displacement gradient matrix is often written as $[S] = \nabla_s\mathbf{u}$. Because of the symmetry of

---

[1] Summation over repeated indices is assumed from now on. For example: $u'_i = a_{ij}u_j$ means $u'_i = \sum_{j=1}^{3} a_{ij}u_j$

$[S]$, this 3×3 matrix can be represented in abbreviated form as the 6×1 vector $\mathbf{S} = (S_1, S_2, S_3, S_4, S_5, S_6)^T$. The relationship between the elements in this vector and those in the strain matrix is simply:

$$[S] = \begin{bmatrix} S_{xx} & S_{xy} & S_{xz} \\ S_{xy} & S_{yy} & S_{yz} \\ S_{xz} & S_{yz} & S_{zz} \end{bmatrix} = \begin{bmatrix} S_1 & \frac{1}{2}S_6 & \frac{1}{2}S_5 \\ \frac{1}{2}S_6 & S_2 & \frac{1}{2}S_4 \\ \frac{1}{2}S_5 & \frac{1}{2}S_4 & S_3 \end{bmatrix} \leftrightarrow \mathbf{S} = \begin{bmatrix} S_1 \\ S_2 \\ S_3 \\ S_4 \\ S_5 \\ S_6 \end{bmatrix}. \tag{2.7}$$

This abbreviated vector notation will be seen to be beneficient when strain is related to stress, the other fundamental property of elasticity, by Hooke's law, issues covered in the following sections.

When strain is given in vector notation, the measure of strain $\mathbf{S} = \nabla_S \mathbf{u}$ is easily found by defining the symmetric gradient operator ∇_S as the matrix:

$$\nabla_S \rightarrow \nabla_{Ij} = \begin{bmatrix} \frac{\partial}{\partial x} & 0 & 0 \\ 0 & \frac{\partial}{\partial y} & 0 \\ 0 & 0 & \frac{\partial}{\partial z} \\ 0 & \frac{\partial}{\partial z} & \frac{\partial}{\partial y} \\ \frac{\partial}{\partial z} & 0 & \frac{\partial}{\partial x} \\ \frac{\partial}{\partial y} & \frac{\partial}{\partial x} & 0 \end{bmatrix}, \tag{2.8}$$

thus $S_I = \nabla_{Ij} u_j$.

2.2.2 Stress

The forces exciting elastic vibrations in a medium may be of two kinds: Body forces and surface or traction forces. Body forces may be caused by gravitational, electric and magnetic fields, and they act directly on any particles in the interior of the body. Traction forces, on the other hand, are forces applied on the boundary of the medium and submitted to the interior by traction forces between the interior elements. The traction forces are called stress, and stress is measured in directional force per unit area, while volume forces are measured in force per unit volume.

In a given stress field, the stress acting on the outer surface of a given body element is a function of the actual orientation of this surface, given by its outwards pointing normal $\mathbf{n}$.

The *reference stresses* $\mathbf{T}_x, \mathbf{T}_y, \mathbf{T}_z$ are the stresses acting on surfaces oriented normal to the coordinate axes used for defining orientations, and it can be shown that the stress $\mathbf{T}_n$ acting on the surface with orientation

$\mathbf{n} = (n_x, n_y, n_z)$ is given by the linear combination $n_x\mathbf{T}_x + n_y\mathbf{T}_y + n_z\mathbf{T}_z$. The reference stresses may be used to define the stress acting on any surface at the given location. The matrix $[T] = [\mathbf{T}_x\,|\mathbf{T}_y|\,\mathbf{T}_z]$ is called the stress tensor, and from the above discussion, the element T_{ij} represents the ith component of the traction force density acting on the $+j$ face of an infinitesimal volume element at the given spatial location. Thus, $T_{in} = T_{ij}n_j$. As will be shown in section 2.3.1, the stress tensor is symmetric, *i.e.* $T_{ij} = T_{ji}$, as long as no volume torque forces acts on the medium.

Since we have that

$$\mathbf{T}_n = [T] \cdot \mathbf{n}, \tag{2.9}$$

and since $[T]$ is symmetric, if follows from elementary linear algebra that for three orthogonal directions $\mathbf{n}_x^{'}, \mathbf{n}_y^{'}$ and $\mathbf{n}_z^{'}$, the stresses acting on the corresponding surfaces are purely normal, *i.e.* for these $\mathbf{n}$:

$$\mathbf{T}_n = [T] \cdot \mathbf{n} = \lambda\,\mathbf{n}. \tag{2.10}$$

These directions correspond to the directions of the eigenvectors of $[T]$. For a given stress field, rotating the coordinate system so that the axes coincide with the orientations of these eigenvectors, the new reference stresses will be pure normal stresses and the stress tensor may be written as

$$[T]' = \begin{bmatrix} T_{xx}^{'} & 0 & 0 \\ 0 & T_{yy}^{'} & 0 \\ 0 & 0 & T_{zz}^{'} \end{bmatrix}. \tag{2.11}$$

For a surface with an arbitrary orientation $\left(n_x^{'}, n_x^{'}, n_z^{'}\right)$ in this new system, the acting stress is thus given by

$$\mathbf{T}_n' = T_{xx}'n_x^{'}\hat{\mathbf{x}}'{+}T_{yy}^{'}n_y'\hat{\mathbf{y}}'{+}T_{zz}n_z\hat{\mathbf{z}}'. \tag{2.12}$$

Regarding the representation of the stress field, similar to the way the symmetric strain-matrix $[S]$ is reduced to the vector $\mathbf{S}$, the symmetric stress matrix $[T]$ may be represented by a vector $\mathbf{T} = (T_1, T_2, T_3, T_4, T_5, T_6)^T$ by the following relationship between the matrix and vector elements:

$$[T] = \begin{bmatrix} T_{11} & T_{12} & T_{13} \\ T_{21} & T_{22} & T_{23} \\ T_{31} & T_{32} & T_{33} \end{bmatrix} = \begin{bmatrix} T_1 & T_6 & T_5 \\ T_6 & T_2 & T_4 \\ T_5 & T_4 & T_3 \end{bmatrix} \leftrightarrow \mathbf{T} = \begin{bmatrix} T_1 \\ T_2 \\ T_3 \\ T_4 \\ T_5 \\ T_6 \end{bmatrix}. \tag{2.13}$$

2.2.3 Hooke's law

Hooke's law states that for the case of small derformations, there is a linear relationship between stress and strain given by fourth rank elasticity tensors $[c]$ or $[s]$ by: $T_{ij} = c_{ijkl}S_{kl}$ or inversely $S_{ij} = s_{ijkl}T_{kl}$. Focusing on the *stiffness tensor* $[c]$ — the equivalent can be stated for the inverse *compliance tensor* — Hooke's law can be written in symbolic writing as $\mathbf{T} = \mathbf{c} : \mathbf{S}$, where the double dot product means summations over pairs of subscripts. Alltogether $[c]$ contains 81 elements, but due to the mentioned symmetries of $[T]$ and $[S]$, $[c]$ has the following properties:

$$c_{ijkl} = c_{jikl} = c_{ijlk}. \tag{2.14}$$

The number of independent linear parameters is hence reduced to 36. We have shown that the stress and strain matrices can be expressed as 6×1 vectors. Observing this, the fourth rank stiffness coefficients c_{ijkl} can be expressed as a second rank tensor $[c_{IJ}]$, a 6×6 matrix. The elements of this matrix correspond to those of the fourth rank tensor by:

$$c_{ijkl} \leftrightarrow c_{IJ},$$

where the pairs ij and kl relates to I and J by:

ij or kl	11	22	33	32 or 23	13 or 31	12 or 21
$\updownarrow$			$\updownarrow$			
I or J	1	2	3	4	5	6

.

In this abbreviated notation, the socalled Voigt notation, the expression of Hooke's law is:

$$T_I = c_{IJ}S_J, \tag{2.15}$$

or inversely

$$S_I = s_{IJ}T_J. \tag{2.16}$$

From considerations of the elastic potential energy in the medium, (see Auld, 1990), it can be shown that $[c_{IJ}]$ is symmetric, *i.e.* $c_{IJ} = c_{JI}$. This further reduces the number of independent elastic constants to maximum 21 for any medium.

2.2.4 Tensor transformations

I have stated that particle displacement $\mathbf{u}$, strain S_{ij} and stress T_{ij} must be related to a given coordinate system. If this coordinate system is rotated, these parameters will be transformated according to the conventions for first and second rank tensors. Similarly it can be shown that the stiffness and compliance coefficients can be transformed by regular 4th rank transformations.

The regular transformation of a nth rank tensor due to a rotation of coordinate axes, is given by

$$P'_{x_1x_2\ldots x_i} = a_{x_1y_1}a_{x_2y_2}\cdots a_{x_iy_i}P_{y_1y_2\ldots y_i}, \tag{2.17}$$

where a_{ij} is the directional cosine of the angle between the new axis $\widehat{\mathbf{i}}'$ and the old axis $\widehat{\mathbf{j}}$. Thus the transformations for the given parameters, given by their full tensor notation form, are:

$$\begin{aligned} u'_i &= a_{ij}u_j, && (2.18)\\ T'_{ij} &= a_{ik}a_{jl}T_{kl}, && (2.19)\\ S'_{ij} &= a_{ik}a_{jl}S_{kl}, && (2.20)\\ c'_{ijkl} &= a_{im}a_{jn}a_{ko}a_{lp}c_{mnop}. && (2.21) \end{aligned}$$

Evidently these calculations are rather elaborate. For example, the calculation of any element of $[c]$ involves 81 summations. However, by using the Voigt notation for stress, strain and the stiffness tensor, the transformation can be performed by using the Bond transformation matrix $[M]$, defined as (Auld, 1990):

$$[M] = \begin{bmatrix} a_{11}^2 & a_{12}^2 & a_{13}^2 & 2a_{12}a_{13} & 2a_{13}a_{11} & 2a_{11}a_{12} \\ a_{21}^2 & a_{22}^2 & a_{23}^2 & 2a_{22}a_{23} & 2a_{23}a_{21} & 2a_{21}a_{22} \\ a_{31}^2 & a_{32}^2 & a_{33}^2 & 2a_{32}a_{33} & 2a_{33}a_{31} & 2a_{31}a_{32} \\ a_{21}a_{31} & a_{22}a_{32} & a_{23}a_{33} & a_{22}a_{33}+a_{23}a_{32} & a_{21}a_{33}+a_{23}a_{31} & a_{22}a_{31}+a_{21}a_{32} \\ a_{31}a_{11} & a_{32}a_{12} & a_{33}a_{13} & a_{12}a_{33}+a_{13}a_{32} & a_{11}a_{33}+a_{13}a_{31} & a_{11}a_{32}+a_{12}a_{31} \\ a_{11}a_{21} & a_{12}a_{22} & a_{13}a_{23} & a_{22}a_{13}+a_{12}a_{23} & a_{11}a_{23}+a_{13}a_{21} & a_{22}a_{11}+a_{12}a_{21} \end{bmatrix} \tag{2.22}$$

The transformation formulas are then expressed in Voigt notation as

$$\mathbf{T}' = [M]\cdot\mathbf{T} \tag{2.23}$$

and

$$[c]' = [M]\,[c]\,[M]^T, \tag{2.24}$$

or in index notation:

$$\begin{aligned} T'_H &= M_{HI}T_I, \\ c'_{IJ} &= M_{IK}M_{JL}c_{KL}. \end{aligned}$$

2.2.5 Symmetric media

With respect to the coordinate dependent elastic properties, rotating the studied medium is equivalent to rotating the coordinate axes in the opposite direction. Usually the elastic constants c_{ij} of a medium change when they are subject to a coordinate transformation. However, when there are symmetries in the elastic properties of the medium for certain transformations, the parameters remain unchanged. If the elastic constants obey some symmetries, i.e. they are invariant for certain rotations of the media, the same counts for the elastic wavepropagation in directions and polarizations according to these symmetries.

The medium containing the most extensive symmetry properties, is the isotropic medium, where the elastic constants are completely independent of the orientation of the coordinate system, that is, the medium can be rotated in any direction and will still provide the same parameters as the original. It can be shown that such a system contains only two independent elastic constants, the Lamè's constants λ and μ:

$$c_{ij} = \begin{bmatrix} \lambda+2\mu & \mu & \mu & 0 & 0 & 0 \\ \mu & \lambda+2\mu & \mu & 0 & 0 & 0 \\ \mu & \mu & \lambda+2\mu & 0 & 0 & 0 \\ 0 & 0 & 0 & \mu & 0 & 0 \\ 0 & 0 & 0 & 0 & \mu & 0 \\ 0 & 0 & 0 & 0 & 0 & \mu \end{bmatrix}. \qquad (2.25)$$

Transverse isotropic media constitutes another frequently encountered symmetry class. Such media have one axis of rotational symmetry, and it can be shown that to have such symmetry the stiffness matrix must contain the following constants:

$$c_{IJ} = \begin{bmatrix} c_{11} & c_{12} & c_{13} & 0 & 0 & 0 \\ c_{12} & c_{11} & c_{13} & 0 & 0 & 0 \\ c_{13} & c_{13} & c_{33} & 0 & 0 & 0 \\ 0 & 0 & 0 & c_{44} & 0 & 0 \\ 0 & 0 & 0 & 0 & c_{44} & 0 \\ 0 & 0 & 0 & 0 & 0 & c_{66} \end{bmatrix}, \qquad (2.26)$$

where $c_{12} = c_{11} - 2c_{66}$. Thus, for an elastic transverse isotropic medium, the elastic properties are given by five independent parameters.

2.3 Elastodynamic considerations

2.3.1 The general elastodynamic relations

Consider an infinite small elastic element with volume δV, surface area δS, density ρ, acted upon by a bodyforce $\mathbf{F}$ and by traction forces from the adjoining medium. Newtons law gives:

$$\int_{\delta S} \mathbf{T} \cdot \mathbf{n}\, dS + \int_{\delta V} \mathbf{F}\, dV = \int_{\delta V} \rho \frac{\partial^2 \mathbf{u}}{\partial t^2} dV. \tag{2.27}$$

Letting the volume decrease towards zero, the following limiting formulae is reached:

$$\nabla \cdot \mathbf{T} = \rho \frac{\partial^2 \mathbf{u}}{\partial t^2} - \mathbf{F}, \tag{2.28}$$

where

$$\nabla \cdot \mathbf{T} = \lim_{\delta V \to 0} \frac{\int_{\delta S} \mathbf{T} \cdot \hat{\mathbf{n}}\, dS}{\delta V}.$$

For an orthogonal system, the divergence of the stress matrix can be written as (Auld, 1990)

$$\nabla \cdot \mathbf{T} = \left(\frac{\partial}{\partial x} \mathbf{T}_x + \frac{\partial}{\partial y} \mathbf{T}_y + \frac{\partial}{\partial z} \mathbf{T}_z \right), \tag{2.29}$$

or in index notation

$$(\nabla \cdot \mathbf{T})_i = \frac{\partial}{\partial x_j} T_{ij}. \tag{2.30}$$

The translational equation of motion can thus be written as

$$\frac{\partial}{\partial x_j} T_{ij} = \rho \frac{\partial^2}{\partial t^2} u_i - F_i, \tag{2.31}$$

or even more compact

$$T_{ij,j} = \rho \ddot{u}_i - F_i. \tag{2.32}$$

In a similar way, the rotational equation of motion can be deduced, based on the principles of torque. The moment of inertia vanishes faster than the volume of the element, thus the applied torques are constrained by the requirement that

$$T_{ji} - T_{ij} + G_k = 0, \tag{2.33}$$

where T_{ij} are shear traction forces and G_k is the volume body torque force in the direction normal to the traction forces. We observe from equation 2.33 that when no body torques are present, the stress matrix is symmetric, a result that was utilized in the previous sections.

Combining the translational equation with Hooke's law,

$$T_{ij}\left(\mathbf{x},t\right) = c_{ijkl}\left(\mathbf{x}\right) S_{kl}\left(\mathbf{x},t\right),$$

the partial differential equation governing wave motion is given as (Aki & Richards, 1980):

$$\rho\left(\mathbf{x}\right) \frac{\partial^2}{\partial t^2} u_i\left(\mathbf{x},t\right) - \frac{\partial}{\partial x_j} c_{ijpq}\left(\mathbf{x},t\right) \frac{\partial}{\partial x_p} u_q\left(\mathbf{x},t\right) = f_i\left(\mathbf{x},t\right), \tag{2.34}$$

or

$$\rho\left(\mathbf{x}\right) \partial_t^2 u_i\left(\mathbf{x},t\right) - \partial_j c_{ijpq}\left(\mathbf{x},t\right) \partial_p u_q\left(\mathbf{x},t\right) = f_i\left(\mathbf{x},t\right). \tag{2.35}$$

In abbreviated notation, like the strain-tensor $\mathbf{S}$ can be found by the multiplication of the matrix operator ∇_S and $\mathbf{u}$, the divergence $\nabla \cdot \mathbf{T}$ can be found by multiplying the following matrix operator $[\nabla\cdot]$ with the vector $\mathbf{T}$:

$$\nabla\cdot \rightarrow \nabla_{iJ} = \begin{bmatrix} \frac{\partial}{\partial x} & 0 & 0 & 0 & \frac{\partial}{\partial z} & \frac{\partial}{\partial y} \\ 0 & \frac{\partial}{\partial y} & 0 & \frac{\partial}{\partial z} & 0 & \frac{\partial}{\partial x} \\ 0 & 0 & \frac{\partial}{\partial z} & \frac{\partial}{\partial y} & \frac{\partial}{\partial x} & 0 \end{bmatrix}. \tag{2.36}$$

Here we note that this matrix operator is the transposed of the matrix operator for ∇_s.

Thus in abbreviated notation

$$\nabla \cdot \mathbf{T} = \nabla_{iJ} T_J. \tag{2.37}$$

In this notation, where Hooke's law is given by $T_i = c_{ij} S_j$ and the strain is given by $S_I = \nabla_{Ij} u_j$, the wave equation

$$\nabla_{iK} T_K = \rho \frac{\partial^2 u_i}{\partial t^2} - F_i \tag{2.38}$$

can be written as

$$\nabla_{iK} c_{KL} \nabla_{Lj} u_j = \rho \frac{\partial^2 u_i}{\partial t^2} - F_i. \tag{2.39}$$

It can be noted that for the left side of equation 2.39, the matrix $[A]_{ij} = \nabla_{iK} c_{KL} \nabla_{Lj}$ is symmetric since c_{KL} is symmetric and the divergence operator matrix is the transposed of the symmetric gradient operator. This symmetry will be utilized in the discussion in section 2.3.3, where I will solve the wave equation for plane waves.

2.3.2 The general wave solution

Any time-harmonic wavefield with time-independent amplitudes may be expressed by

$$\mathbf{u}(\mathbf{x}, t) = \mathbf{U}_0(\mathbf{x}) e^{i\omega(t-\tau(\mathbf{x}))}. \tag{2.40}$$

Here surfaces where the phase $\tau(\mathbf{x})$ is constant constitutes socalled waveplanes where the phase given by the exponential is constant for a given time t. Assuming that $\tau(\mathbf{x})$ is differentiable we have that $\tau(\mathbf{x}+d\mathbf{x}) = \nabla\tau(\mathbf{x}) \cdot d\mathbf{x}$. Thus, for the phase of the wave-function to be the same at $\mathbf{x}$ at time t and $\mathbf{x}+d\mathbf{x}$ at time $t + dt$, it is required that

$$dt - \nabla\tau(\mathbf{x}) \cdot d\mathbf{x} = 0, \tag{2.41}$$

which implies that

$$\nabla\tau \cdot \frac{d\mathbf{x}}{dt} = 1. \tag{2.42}$$

The $\frac{d\mathbf{x}}{dt}$-vector denotes the phase velocity of the wave, and equation 2.42 gives that

$$|\mathbf{V}| = \frac{1}{|\nabla\tau|}. \tag{2.43}$$

For plane waves, $\tau(\mathbf{x})$ may be written as $(\mathbf{k} \cdot \mathbf{x})/\omega$, thus $\nabla\tau$ equals $\mathbf{k}/\omega$ and the phase velocity is given by $V = \omega/|\mathbf{k}|$. The wave number vector $\mathbf{k}$ thus gives the direction of wave propagation and the wavelength λ by $k = |\mathbf{k}| = 2\pi/\lambda$. The direction of $\mathbf{k}$ may also be expressed by the unit vector $\hat{\mathbf{l}}$, letting $\mathbf{k} = k\,\hat{\mathbf{l}}$. The components of $\hat{\mathbf{l}}$ is the direction cosines of the wavenumber vector, *i.e.* $\hat{\mathbf{l}} = (l_x, l_y, l_z) = \mathbf{k}/|\mathbf{k}| = (k_x, k_y, k_z)/k$.

The wave equation is usually solved for plane waves, which approximately resembles the far-field of a seismic source. Any plane wave propagating in the direction of $\hat{\mathbf{l}}$ may be given as a superposition of harmonic waves with constant frequency and wavenumber. Each component can be written as

$$\mathbf{u}(\mathbf{x},t) = \mathbf{U}_0(\omega, \mathbf{k}) e^{i(\omega t - \mathbf{k}\cdot\mathbf{x})}, \tag{2.44}$$

where the amplitude and phase of the constant $\mathbf{U}_0$ is found by Fourier transforming the signal to the ω-k domain. If the wavefield represents the particle displacement, the polarization is given by the direction of the $\mathbf{U}_0$-vector. Solving the wave equation for a given medium then involves finding the relation between ω and $\mathbf{k}$ for possible time independent polarization directions. This relation can be expressed in terms of *e.g.* the phase velocity.

I will now deduce the Christoffel equation which will be used for solving the wave equation for the time-and-space harmonic waves.

2.3.3 The Christoffel equation

The general plane wave solution to the wave equation is given on the form

$$\mathbf{u}\left(\mathbf{x},\mathbf{t}\right)=\mathbf{U}_0 e^{i\omega-\mathbf{k}\cdot\mathbf{x}},\tag{2.45}$$

and represents the time- and space harmonic wave with polarization in the direction of $\mathbf{U}_0$. In component form for the abbreviated Voigt notation, the wave equation was given in equation 2.39 by

$$\nabla_{iK}c_{KL}\nabla_{Lj}u_j=\rho\frac{\partial^2 u_i}{\partial t^2}-F_i,\tag{2.46}$$

corresponding to the vector equation

$$\nabla\cdot\mathbf{c}:\boldsymbol{\nabla}_s\mathbf{u}=\rho\frac{\partial^2\mathbf{u}}{\partial t^2}-\mathbf{F}.\tag{2.47}$$

When the wavenumber vector is directed in direction $\hat{\mathbf{l}}$, so that $\mathbf{k}=k\,\hat{\mathbf{l}}=k\left(l_x,l_y,l_z\right)$, the scalar product in the exponential factor of the wavefield expression is given by $\mathbf{k}\cdot\mathbf{x}=k\left(l_x x_1+l_y x_2+l_z x_3\right)$. Accordingly, the partial derivatives involved in the operators operators above are given by

$$\frac{\partial\mathbf{u}}{\partial x_i}=-ikl_i\mathbf{u}\tag{2.48}$$

and

$$\frac{\partial^2\mathbf{u}}{\partial t^2}=-\omega^2\mathbf{u}.\tag{2.49}$$

Thus in the two matrix operators corresponding to the divergence and symmetric gradient, the expressions ∂/dx_i may be replaced by the expression $-ikl_i$. The operators ∇_{iK} and ∇_{Lj} in equation 2.39 may then be replaced by the matrices $-ikl_{iK}$ and $-ikl_{Lj}$ respectively, where

$$l_{iK}=\begin{bmatrix} l_x & 0 & 0 & 0 & l_z & l_y\\ 0 & l_y & 0 & l_z & 0 & l_x\\ 0 & 0 & l_z & l_y & l_x & 0\end{bmatrix}\tag{2.50}$$

and

$$l_{Lj}=\begin{bmatrix} l_x & 0 & 0\\ 0 & l_y & 0\\ 0 & 0 & l_z\\ 0 & l_z & l_y\\ l_z & 0 & l_x\\ l_y & l_x & 0\end{bmatrix}.\tag{2.51}$$

Assuming that the body force $\mathbf{F}$ is zero, the wave equation then reduces to

$$k^2 \left(l_{iK} c_{KL} l_{Lj}\right) u_j = k^2 \Gamma_{ij} u_j = \rho \omega^2 u_i. \tag{2.52}$$

Equation 2.52 is called the Christoffel equation, and the matrix on the left side,

$$\Gamma_{ij} = \left(l_{iK} c_{KL} l_{Lj}\right), \tag{2.53}$$

is called the Christoffel matrix. The Christoffel matrix $\mathbf{\Gamma}$ is symmetric, since $l_{iK} = l_{Ki}$ in the two matrix operators and c_{KL} is symmetric (see section 2.3.1). The solution to the wave equation can thus be found by solving the eigenvalue-problem given by

$$\mathbf{\Gamma}\, \mathbf{u} = \gamma\, \mathbf{u}, \tag{2.54}$$

simplified to

$$\mathbf{\Gamma}\, \mathbf{U}_0 = \gamma\, \mathbf{U}_0 \tag{2.55}$$

by cancelling the exponentials. Here $\gamma = \rho\omega^2/k^2$ and $\mathbf{U}_0$ represents the direction of wave polarization.

The symmetric 3×3 Christoffel matrix always has a set of orthonormal eigenvectors $\mathbf{U}_1, \mathbf{U}_2, \mathbf{U}_3$ with corresponding eigenvalues $\gamma_1, \gamma_2, \gamma_3$. If *all* the eigenvalues are different, the corresponding $\mathbf{U}_1$, $\mathbf{U}_2$, and $\mathbf{U}_3$ define three different wave modes with phase velocities given by

$$V_i = \omega/k = \sqrt{\frac{\gamma_i}{\rho}}. \tag{2.56}$$

For any displacement vector in such a medium, the components parallel to the corresponding eigenvectors will propagate with different velocities. This phenomena is called *birefringence*. On the other hand, if two of the eigenvalues are equal, waves with any particle displacement vector in the eigenspace plane spanned by the eigenvectors of this eigenvalue, forming socalled *degenerate* waves, will propagate with the same velocity. Degeneracy provides the basis for superposition of waves to generate waves propagating with the same velocity but having different polarizations. Contrary to the constituting waves which have a 1-D linear polarization, the displacement vector of the composite wave may also have a circular or elliptical polarization within the eigenspace, polarization shapes occurring when there is a phase shift between the constituting waves.

The Christoffel equation may be rewritten as

$$\left(\mathbf{\Gamma} - \gamma \mathbf{I}\right) \mathbf{U}_0 = 0, \tag{2.57}$$

where the eigenvalues for the given direction of propagation are found by setting the characteristic determinant Ω equal to zero, *i.e.*

$$\Omega\left(\omega, k, l_x, l_y, l_z\right) = \left|k^2 \Gamma_{ij}\left(l_x, l_y, l_z\right) - \rho\omega^2 \delta_{ij}\right| = 0, \tag{2.58}$$

where δ_{ij} is the Kroeneker delta defined as

$$\delta_{ij} = \begin{array}{ll} 1, & j = i \\ 0, & j \neq i \end{array}. \tag{2.59}$$

We will now look at the solutions of this equation in the isotropic and transverse isotropic case.

2.3.4 Solutions for the isotropic medium

With the properties of the stiffness tensor for an isotropic medium, the Christoffel matrix for a wave propagating in the direction of $\hat{\mathbf{l}}$ is given by

$$\mathbf{\Gamma} = \left[\begin{array}{ccc} c_{11} l_x^2 + c_{44}\left(1 - l_x^2\right) & \left(c_{11} - c_{44}\right) l_x l_y & \left(c_{11} - c_{44}\right) l_x l_z \\ \left(c_{11} - c_{44}\right) l_x l_y & c_{11} l_y^2 + c_{44}\left(1 - l_y^2\right) & \left(c_{11} - c_{44}\right) l_y l_z \\ \left(c_{11} - c_{44}\right) l_x l_z & \left(c_{11} - c_{44}\right) l_y l_z & c_{11} l_z^2 + c_{44}\left(1 - l_z^2\right) \end{array}\right]. \tag{2.60}$$

Since the medium is isotropic, the same set of eigenvalues are expected from any choice of $\hat{\mathbf{l}}$, and these values can easily be shown to be

$$\gamma_1 = c_{11}, \tag{2.61}$$

$$\gamma_2 = c_{44}. \tag{2.62}$$

The eigenvector γ_2 is a double root, with corresponding eigenvectors normal to the direction of $\hat{\mathbf{l}}$, while the corresponding eigenvector of γ_1 points in the direction of $\hat{\mathbf{l}}$. The wave with polarization in the direction of $\hat{\mathbf{l}}$ thus has a phase velocity given by

$$V_P = \sqrt{\frac{c_{11}}{\rho}}, \tag{2.63}$$

while the wave with polarization normal to direction of polarization has the velocity

$$V_S = \sqrt{\frac{c_{44}}{\rho}}. \tag{2.64}$$

The P-wave, called the primary wave because this wave propagates faster than the S-wave, *i.e.* the secondary wave, has a curl-free wavefield, $\nabla \times \mathbf{u}_S = \mathbf{0}$, while the S-wave field is dilatational-free, *i.e.* $\nabla \cdot \mathbf{u}_S = 0$. Among alternative names for the P- and S-waves are compressional and shear waves respectively, since forces acting on a small volume element exposed to the corresponding wave fields, are purely compressional and shear stresses respectively.

2.3.5 Solutions for the transverse isotropic medium

In a similar way the Christoffel equation can be solved for a transverse isotropic medium with the symmetry axis along the z-axis. For waves propagating in the direction of $\hat{\mathbf{l}} = (l_x, l_y, l_z)$ in such a media, the Christoffel matrix is given by

$$\mathbf{\Gamma} = \begin{bmatrix} c_{11}l_x^2 + c_{66}l_y^2 + c_{44}l_z^2 & (c_{12}+c_{66})\,l_xl_y & (c_{13}+c_{44})\,l_xl_z \\ (c_{12}+c_{66})\,l_xl_y & c_{66}l_x^2 + c_{11}l_y^2 + c_{44}l_z^2 & (c_{13}+c_{44})\,l_yl_z \\ (c_{13}+c_{44})\,l_xl_z & (c_{13}+c_{44})\,l_yl_z & c_{44}l_x^2 + c_{44}l_y^2 + c_{33}l_z^2 \end{bmatrix}. \tag{2.65}$$

For any direction of propagation $\hat{\mathbf{l}}$, the eigenvectors and eigenvalues of $\mathbf{\Gamma}$ defines the different wave modes in the medium in terms of the associated allowed displacement polarizations and dispersion relations, *i.e.* the required relationship between $\mathbf{k}$ and ω expressed as phase velocity $\mathbf{V} = \omega/k\,\hat{\mathbf{l}}$ or by phase slowness $\mathbf{k}/\omega = 1/V\,\hat{\mathbf{l}}$.

For most directions of $\hat{\mathbf{l}}$ all the eigenvalues $\gamma_1\left(\hat{\mathbf{l}}\right)$, $\gamma_2\left(\hat{\mathbf{l}}\right)$ and $\gamma_3\left(\hat{\mathbf{l}}\right)$ will be different, thus defining three independent wave modes. These modes will here be described first in terms of polarization and then in terms of velocity. Prior to this description, however, it can be noted that since the medium is symmetric about the z-axis, the wave properties of the medium can be fully described by considering waves propagating in the x-z plane. The unit wave vector $\hat{\mathbf{l}}$ is then fully described by its x- and z-coordinate, which may be written as $\hat{\mathbf{l}} = (\pm\sin\theta, \pm\cos\theta)$ where θ is the angle between $\hat{\mathbf{l}}$ and the vertical direction in the range $[0, \pi/2]$. Obviously waves with wavenumber vectors $\hat{\mathbf{l}}$ and $-\hat{\mathbf{l}}$, *i.e.* waves propagating in opposite directions, have the same dispersion relation, and this also is valid for vectors symmetric about the z-axis because of the transverse isotropy. By inspecting the $\mathbf{\Gamma}$-matrix, the possible negative signs in the $\hat{\mathbf{l}}$-components and may thus be ignored. Accordingly, the dispersion functions plotted as polar plots in the x-z plane are symmetric about both the z-axis and the x-axis.

For the appropriate numbering of the eigenvalue functions, for all directions $\hat{\mathbf{l}}$ in the x-z plane the function $\gamma_3\left(\hat{\mathbf{l}}\right)$ will have a eigenspace containing an eigenvector parallel to the y-axis. This vector is always normal to the direction of propagation and thus represents a pure shear wave mode. This wave-mode is called the SH-wave due to the horizontal polarization.

For a few directions $\hat{\mathbf{l}}$, in specific where $\theta = 0°, \theta = 45°$ and $\theta = 90°$, the eigenvector of the eigenfunction $\gamma_1\left(\hat{\mathbf{l}}\right)$ will be parallel to $\hat{\mathbf{l}}$. This resembles the behaviour of the P-wave in the isotropic case. However, for most directions of $\hat{\mathbf{l}}$, the eigenvector associated to that eigenvalue is not parallel to the direction of $\hat{\mathbf{l}}$, thus this wave mode is denoted the quasi-P-wave.

The polarization of the third wave mode is orthogonal to the other two polarizations. Thus this polarization is also confined to the x-z plane. For the propagation directions where the quasi-P-wave is polarized in the direction of the wave vector, this third wave mode is a pure shear wave. Therefore this wave is called the quasi-S-wave, often denoted the SV-wave, since its polarization is in the vertical plane.

Due to the symmetry about the z-axis, vertically shear waves with a displacement polarization in any direction in the x-y plane must propagate with identical velocities. Thus, the SH- and SV-wave are degenerate for this orientation of propagation. It can also be shown from solving the Christoffel equation, that vertically and horizontally propagating SV-wave must always travel with identical velocities, still assuming a vertical symmetry axis.

By finding the eigenvectors γ_1, γ_2 and γ_3 from the Christoffel-matrix as a function of θ, where θ is the mentioned angle between $\hat{\mathbf{l}}$ and the symmetry axis, the phase velocities are given by the following equations (Thomsen, 1994):

$$\begin{aligned} V_{qP}(\theta) &= \left(\frac{1}{2\rho}\left[c_{33} + c_{44} + (c_{11} - c_{33})\sin^2\theta + D(\theta)\right]\right)^{\frac{1}{2}}, && (2.66)\\ V_{SV}(\theta) &= \left(\frac{1}{2\rho}\left[c_{33} + c_{44} + (c_{11} - c_{33})\sin^2\theta - D(\theta)\right]\right)^{\frac{1}{2}}, && (2.67) \end{aligned}$$

and

$$V_{SH}(\theta) = \left(\frac{1}{\rho}\left(c_{66}\sin^2\theta + c_{44}\cos^2\theta\right)\right)^{\frac{1}{2}}, \qquad (2.68)$$

where

$$\begin{aligned} D(\theta) = \; & \left\{(c_{33} - c_{44})^2\right.\\ & +2\left[2(c_{13} + c_{44})^2 - (c_{33} - c_{44})(c_{11} + c_{33} - 2c_{44})\right]\sin^2\theta\\ & \left.+\left[(c_{11} + c_{33} - 2c_{44})^2 - 4(c_{13} + c_{44})^2\right]\sin^4\theta\right\}^{1/2}. \qquad (2.69) \end{aligned}$$

Plotting the velocities as polar functions of θ, where

$$(V_x, V_z) = V(\theta)(\sin(\theta), \cos(\theta)),$$

defines the phase velocity curve or surface for the given medium. Such velocity curves are plotted in figure 2.2 a), where the elastic constants of the medium is given in the figure. A different but frequently used representation of the dispersion relation is the slowness curve or surface. The slowness curve

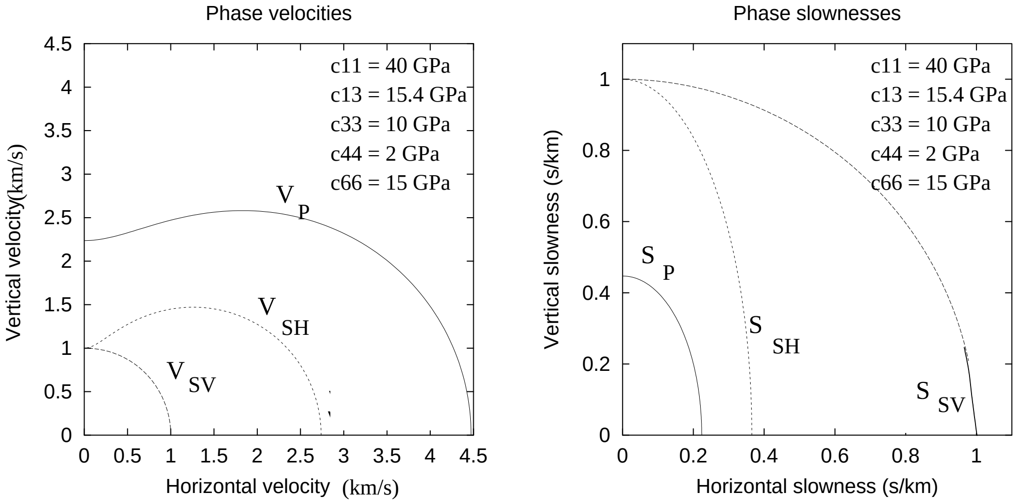

a) b)

Figure 2.2: The (a) phase velocity and (b) phase slowness curves in the symmetry plane of a transverse isotropic medium symmetric about the z-axis.

is simply given by $(S_x, S_z) = (1/V_x, 1/V_z)$. In figure 2.2 the corresponding slowness curve is plotted in panel b).

The phase velocity describes the velocity the wave-surface of a *plane* wave propagates in the direction perpendicular to the wave surface, *i.e.* parallel to $\hat{\mathbf{l}}$. Now let us look at the properties of a wave generated by a point source in the given medium.

The velocity of which a generated wave propagates away from the point source location, can be defined as the group velocity V_g.

The corresponding group velocity surface may thus be viewed as a snapshot of an expanding wave phase surface generated at origo. Using the formulas that will be given shortly for deriving V_g, figure 2.3 presents the group velocities of the transverse isotropic medium of which corresponding phase velocity curves were plotted in figure 2.2 a). As we notice immediately, the shape of the phase- and group velocity surfaces are different.

Now let us look at an explanation of the relationship between the phase and group velocities. A point source may be viewed as a device exciting plane waves uniformly in all directions. That is – the plane waves has the same amplitude and polarization mode in all directions $\hat{\mathbf{l}}$. From this point of view, the closed wave surface generated from this excitation, is the constructive interference of these plane waves.

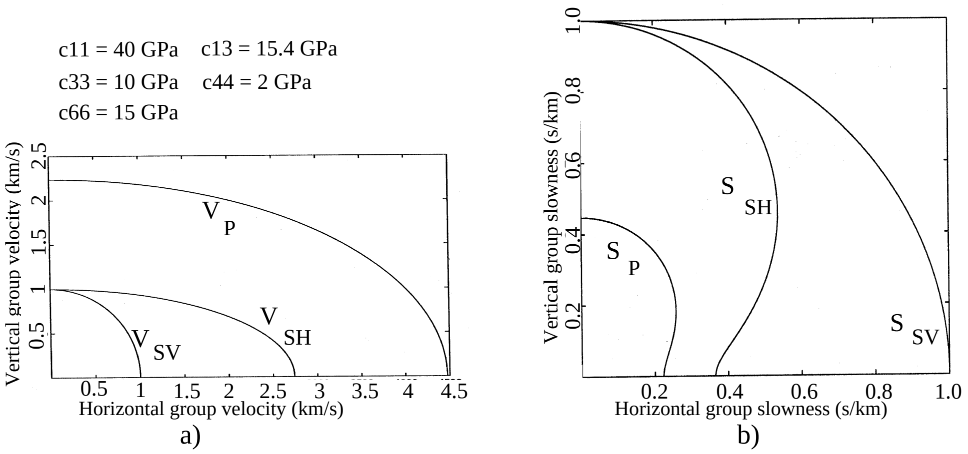

a) b)

Figure 2.3: The group (a) velocity and (b) slownesses for the anisotropic medium of which dispersion relations were given in figure 2.2.

In an isotropic medium, these plane waves radiate with identical velocity for all propagation directions $\hat{\mathbf{l}}$. The constructive interference of the plane waves is thus normal to $\hat{\mathbf{l}}$, generating a circular wave curve identical to the phase velocity curve. For the isotropic medium, the phase- and group velocities are thus identical, *i.e.* $V\left(\hat{\mathbf{l}}\right) = V_g\left(\hat{\mathbf{r}}\right)$, and $\hat{\mathbf{l}} = \hat{\mathbf{r}}$, where $\hat{\mathbf{r}}$ is the vector pointing in the direction where the plane wave with wave vector $\mathbf{k} = k\hat{\mathbf{l}}$ contributes to the group velocity curve.

In the anisotropic case the result is different, since phase velocities changes with $\hat{\mathbf{l}}$.

Figure 2.4 displays how plane waves, with wavefronts normal to the directions of propagation $\hat{\mathbf{l}}$ given by the dashed lines and located from origo according to the phase velocity surface, generate the corresponding group velocity surface. The point on the group velocity surface corresponding to each visualized $\hat{\mathbf{l}}$, is indicated by small circles.

The surfaces represents a generalized TI medium. It is seen that for directions perpendicular and parallel to the symmetry axis the phase and group velocities are equal, and the angle ϕ between $\hat{\mathbf{l}}$ and $\hat{\mathbf{r}}$ is zero. For other directions of $\hat{\mathbf{l}}$, as indicated in panel a) of this figure, $V\left(\hat{\mathbf{l}}\right) = V_g\left(\hat{\mathbf{r}}\right)\cos\phi$ by simple trigonometry.

Assuming that the energy triggered by the source is distributed uniformly to the plane waves for all $\hat{\mathbf{l}}$, a segment of length dS on the group velocity curve corresponding to a large angular range of corresponding plane-waves will contain more energy than a different dS-interval on the same curve cor-

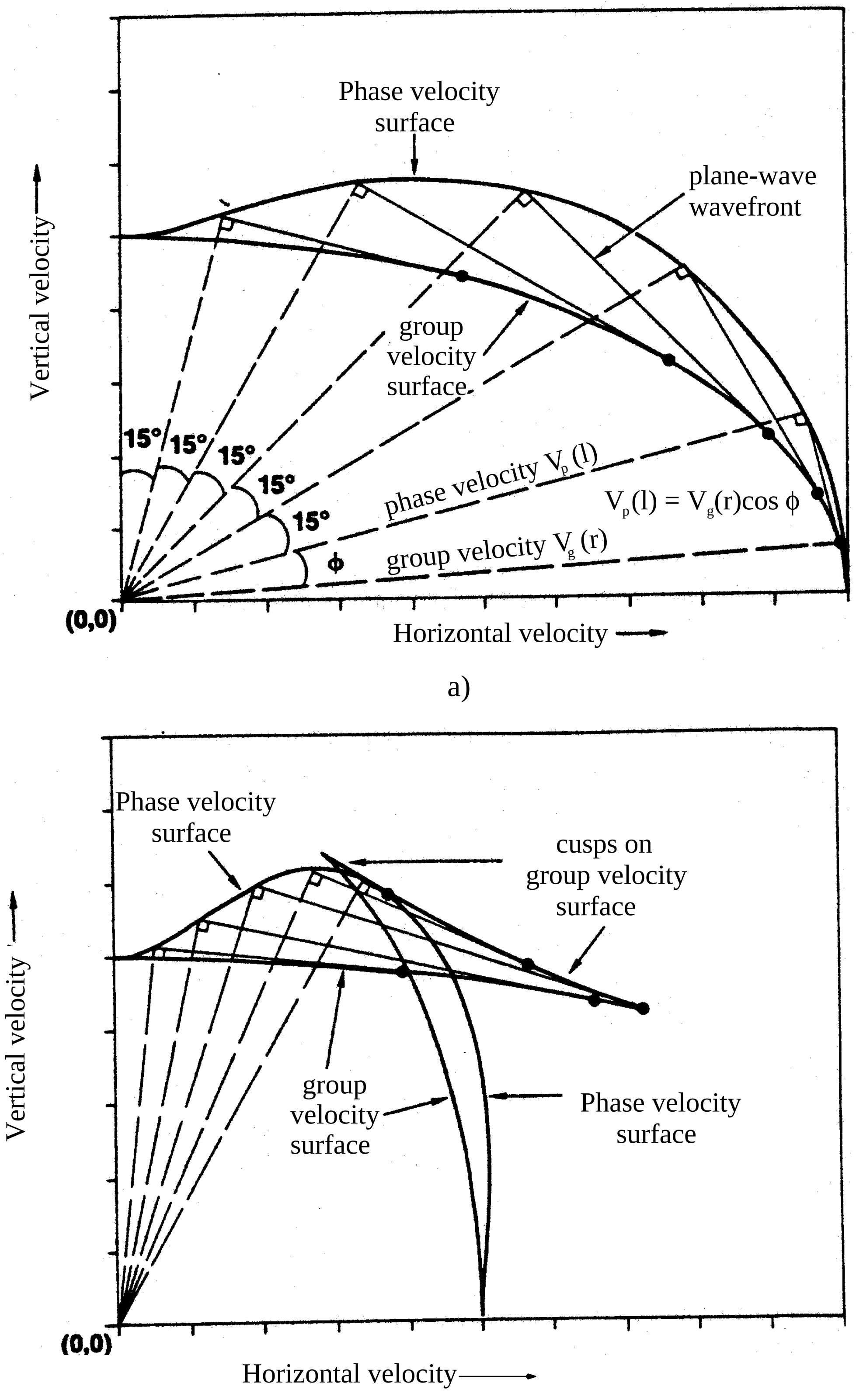

a)

b)

Figure 2.4: Relationship between phase velocity and group velocity. (Winterstein, 1990).

responding to a smaller range of corresponding plane-waves. As stated by Winterstein (1990), consequently the energy triggered by a point source in a homogeneous but anisotropic medium is not necessarily spread uniformly in all directions. This point is illustrated by the varying spatial density of the mentioned circles on the group velocity curve in panel a) in figure 2.4.

Obviously the group velocity can also be derived numerically from the dispersion relation $\Omega(\mathbf{k},\omega)=0$ which the phase velocity and slowness surfaces are variations of. This characteristic equation implicitely gives ω as a function of $\mathbf{k}=k\hat{\mathbf{l}}$, and the group velocity is given as the gradient of this function, *i.e.* (Mavko et al., 1993):

$$\mathbf{V}_g\left(\hat{\mathbf{l}}\right)=\nabla\omega_k=\hat{\mathbf{x}}\frac{\partial\omega}{\partial k_x}+\ldots+\hat{\mathbf{z}}\frac{\partial\omega}{\partial k_z}. \tag{2.70}$$

Equation 2.70 implicates that the direction of the group velocity associated to a given wavenumber vector $\mathbf{k}$, is given by the normal vector to the corresponding point on the slowness-surface, which gives ω as a function of $\mathbf{k}$.

Numerically, the gradient in equation 2.70 is given by the implicit function

$$\mathbf{V}_g=-\frac{\nabla_k\Omega}{\partial\Omega/\partial\omega} \tag{2.71}$$

where Ω is the characteristic equation 2.58.

It can be shown from equation 2.70 that the relationships between the phase velocity $V\left(\hat{\mathbf{l}}\right)$ and the associated group velocity $V_g\left(\hat{\mathbf{r}}\right)$ is given by (Thomsen, 1986):

$$V_g^2\left(\psi(\theta)\right)=V_p\left(\theta\right)^2+\left(\frac{dV_P}{d\theta}\right)^2, \tag{2.72}$$

where ψ is the angle between the z-axis and $\hat{\mathbf{r}}$, and θ is the angle between the z-axis and the wavenumber vector $\hat{\mathbf{l}}$, and where

$$\begin{aligned}\tan\left(\psi\left(\theta\right)\right) &= V_{g,x}/V_{g,z}=\frac{\partial\left(kV\right)/\partial k_x}{\partial(kV)/\partial k_z}\\ &= \left(\tan\theta+\frac{1}{V}\frac{dV}{d\theta}\right)/\left(1-\frac{\tan\theta}{V}\frac{dV}{d\theta}\right).\end{aligned} \tag{2.73}$$

2.3.6 Thomsen parameters for weak anisotropic media

Thomsen (1986) states that most composite rocks contain weak elastic transverse isotropy where the symmetry axis is the vertical axis, and that the related angular dispersion can be stated in terms of the vertical qP- and qS-velocity, α_0 and β_0 respectively, and three parameters describing the anisotropy, the socalled Thomsen-parameters, ε, δ and γ. The angular dispersion with these parameters are as follows, where θ is the angle between the wavenumber vector and the z-axis:

$$\begin{aligned} V_P(\theta) &= \alpha_0\left(1+\delta\sin^2\theta\cos^2\theta+\varepsilon\sin^4\theta\right), &(2.74)\\ V_{SV}(\theta) &= \beta_0\left(1+\frac{\alpha_0^2}{\beta_0^2}(\varepsilon-\delta)\sin^2\theta\cos^2\theta\right), &(2.75)\end{aligned}$$

and

$$V_{SH}(\theta)=\beta_0\left(1+\gamma\sin^2\theta\right), \tag{2.76}$$

where

$$\begin{aligned} \varepsilon &= \frac{c_{11}-c_{33}}{2c_{33}}=\frac{V_P(90^\circ)-\alpha_0}{\alpha_0}, &(2.77)\\ \gamma &= \frac{c_{66}-c_{44}}{2c_{44}}=\frac{V_{SH}(90^\circ)-\beta_0}{\beta_0}, &(2.78)\end{aligned}$$

and

$$\delta=\frac{\left(c_{13}+c_{44}\right)^2-\left(c_{33}-c_{44}\right)^2}{2c_{33}\left(c_{33}-c_{44}\right)}. \tag{2.79}$$

Even though ε and γ are the traditional measurements for transverse isotropy, since these give the difference between vertical and horizontal velocity of the P- and S-wave, for small angles θ the parameter δ is by far the most significant on the waveshape, relevant to analysis of near-vertical waves, which are studied in most seismic surveys. For interested readers, see Thomsen (1986).

For weak anisotropy, Thomsen shows that the group velocity is given by:

$$V_g(\phi)=V(\theta) \tag{2.80}$$

where the group- and phase velocities are pairs of the same polarization. The corresponding angle $\phi=\phi(\theta)$ is for weak anisotropy given by the relation

$$\tan\phi=\tan\theta\left[1+\frac{1}{\sin\theta\cos\theta}\frac{1}{V(\theta)}\frac{dV}{d\theta}\right], \tag{2.81}$$

which fully linearized leads to

$$\begin{aligned} \tan\phi_P &= \tan\theta_p\left[1+2\delta+4(\varepsilon-\delta)\sin^2\theta_p\right], &(2.82)\\ \tan\phi_{SV} &= \tan\theta_{SV}\left[1+2\frac{\alpha_0^2}{\beta_0^2}(\varepsilon-\delta)\left(\varepsilon-2\sin^2\theta_{SV}\right)\right], &(2.83)\end{aligned}$$

and

$$\tan\phi_{SH}=\tan\theta_{SH}\left(1+2\gamma\right). \tag{2.84}$$

The procedure for finding the group velocity surface is thus greatly simplified compared to the general case for anisotropic media.

2.3.7 Backus upscaling

Thus far we have considered wave propagation in only a homogeneous medium. What is really of interest in this study, however, is the behaviour of a thin-layered medium. As stated by Helbig (1984), for all layer thicknesses, the wavefield in the composite medium can be calculated by solving the wave equation for each homogeneous layer and requiring continuous stresses and displacements across all layer boundaries. Such exact solutions forms the basis for the use of propagator matrices, which is discussed briefly in the following section.

For very long wave lengths, *i.e.* $\lambda/d >> 1$, it is assumed that the stress-strain state in a representative volume element, containting the different thin layers, is nearly homogeneous. Thus it should be possible to approximate its elastodynamic behaviour for such wavelengths by calculating its static stress-strain relationship. This is the basis idea of the Backus averaging (Backus, 1962). Instead of solving the wave equaton for the composite medium, a replacement medium is calculated that is valid for the long wavelength to layer thickness case.

Backus showed that a horizontally thin layered medium, made up of isotropic or transverse isotropic layers with symmetry axis perpendicular to the layering, can be replaced by an effective large scale medium that is transverse isotropic.

Backus averaging is an averaging process where the effective, or upscaled, parameters are found by an averaging over functions of the elastic constants of the individual layers to form similar functions of the effective constants of the upscaled medium. to represent a vertically heterogenous medium as a long-wave-equivalent transverse isotropic medium.

As explained in Mæland (1993) , such averaging is equivalent to convolving the the functions of the small scale parameterization, $\mathbf{f}(z)$, with an averaging window $w(z)$. This average at location z is given by $\langle \mathbf{f}(z) \rangle$ is found by:

$$\langle \mathbf{f}(z) \rangle = \int_{-A/2}^{A/2} \mathbf{f}(z' - z)\, w(z')\, dz', \tag{2.85}$$

where the averaging window has the properties

$$\int_{-\infty}^{+\infty} w(z)\, dz = 1, \tag{2.86}$$

$$\int_{-\infty}^{+\infty} z \cdot w(z)\, dz = 0, \tag{2.87}$$

and

$$w(z) = 0 \text{ for } |z| > A/2. \tag{2.88}$$

The effective elastic parameters are found by applying the above mentioned averaging on algebraic combinations of the elastic coefficients of the original medium, and consequently operating on these averages. Given the stiffness tensor for each single layer by:

$$\begin{bmatrix} c_{11} & c_{12} & c_{13} & 0 & 0 & 0 \\ c_{12} & c_{11} & c_{13} & 0 & 0 & 0 \\ c_{13} & c_{13} & c_{33} & 0 & 0 & 0 \\ 0 & 0 & 0 & c_{44} & 0 & 0 \\ 0 & 0 & 0 & 0 & c_{44} & 0 \\ 0 & 0 & 0 & 0 & 0 & c_{66} \end{bmatrix}, \ c_{66} = \frac{1}{2}\left(c_{11} - c_{12}\right), \tag{2.89}$$

the effective transverse isotropic medium will have the stiffness tensor:

$$\begin{bmatrix} C_{11} & C_{12} & C_{13} & 0 & 0 & 0 \\ C_{12} & C_{11} & C_{13} & 0 & 0 & 0 \\ C_{13} & C_{13} & C_{33} & 0 & 0 & 0 \\ 0 & 0 & 0 & C_{44} & 0 & 0 \\ 0 & 0 & 0 & 0 & C_{44} & 0 \\ 0 & 0 & 0 & 0 & 0 & C_{66} \end{bmatrix}, \ C_{66} = \frac{1}{2}\left(C_{11} - C_{12}\right), \tag{2.90}$$

where

$$\begin{aligned} C_{11} &= \left\langle c_{11} - c_{13}^2 c_{33}^{-1} \right\rangle + \left\langle c_{33}^{-1} \right\rangle^{-1} \left\langle c_{13} c_{33}^{-1} \right\rangle^2, && (2.91) \\ C_{12} &= \left\langle c_{12} - c_{13}^2 c_{33}^{-1} \right\rangle + \left\langle c_{33}^{-1} \right\rangle^{-1} \left\langle c_{13} c_{33}^{-1} \right\rangle^2, && (2.92) \\ C_{33} &= \left\langle c_{33}^{-1} \right\rangle^{-1}, && (2.93) \\ C_{13} &= \left\langle c_{33}^{-1} \right\rangle^{-1} \left\langle c_{13} c_{33}^{-1} \right\rangle, && (2.94) \\ C_{44} &= \left\langle c_{44}^{-1} \right\rangle^{-1}, && (2.95) \end{aligned}$$

and

$$C_{66} = \left\langle c_{66} \right\rangle. \tag{2.96}$$

When the components are isotropic, they are described by Lamès constants λ and μ. $c_{11} = c_{33} = (\lambda + 2\mu)$, $c_{12} = c_{13} = \lambda$, $c_{44} = c_{66} = \mu$. This leads to:

$$\begin{aligned} C_{11} &= \left\langle 4\mu \frac{\lambda + \mu}{\lambda + 2\mu} \right\rangle + \left\langle \frac{1}{\lambda + 2\mu} \right\rangle^{-1} \left\langle \frac{\lambda}{\lambda + 2\mu} \right\rangle^2, && (2.97) \\ C_{12} &= \left\langle 2\lambda \frac{\mu}{\lambda + 2\mu} \right\rangle + \left\langle \frac{1}{\lambda + 2\mu} \right\rangle^{-1} \left\langle \frac{\lambda}{\lambda + 2\mu} \right\rangle^2, && (2.98) \end{aligned}$$

$$C_{33} = \left\langle \frac{1}{\lambda + 2\mu} \right\rangle^{-1}, \tag{2.99}$$

$$C_{13} = \left\langle \frac{1}{\lambda + 2\mu} \right\rangle^{-1} \left\langle \frac{\lambda}{\lambda + 2\mu} \right\rangle, \tag{2.100}$$

$$C_{44} = \left\langle \frac{1}{\mu} \right\rangle^{-1}, \tag{2.101}$$

and

$$C_{66} = \langle \mu \rangle . \tag{2.102}$$

If the small scale isotropic medium is given in terms of P- and S-velocity and density for each layer, Lamè's constants can easily be derived since

$$V_P = \sqrt{\frac{\lambda + 2\mu}{\rho}} \tag{2.103}$$

and

$$V_S = \sqrt{\frac{\mu}{\rho}}. \tag{2.104}$$

The input to the averaging is thus frequently found by

$$c_{11} = c_{33} = \left(\rho V_P^2\right), \tag{2.105}$$

$$c_{44} = c_{66} = \left(\rho V_S^2\right), \tag{2.106}$$

and

$$c_{12} = c_{13} = \left(\rho \left(V_P^2 - 2V_S^2\right)\right). \tag{2.107}$$

2.3.8 The propagator method

In the ray theory or short wavelength limit, the total traveltime for waves traveling perpendicular to the layering of a layered medium equals the sum of the traveltimes in each of its constituents. Given that the composite medium consists of k different types of media, and each material has vertical velocity V_k and constitutes the volume fraction f_k of the entire medium, the ray theory average velocity V_{RT} through the medium is given by

$$\frac{1}{V_{RT}} = \sum_k \frac{f_k}{V_k}. \tag{2.108}$$

This velocity is thus found by averaging the slownesses of the constituents.

For a thin-layered medium, *i.e.* where $\lambda >> d$, the Backus theory presented in the previous chapter led to an effective medium velocity V_{EMT} perpendicular to the layering given by

$$\frac{1}{\rho_{ave} V_{EMT}^2} = \sum_k \frac{f_k}{\rho_k V_k^2}. \tag{2.109}$$

which is equal to the velocity corresponding to the Reuss averaged small scale medium.

For intermediate ranges of λ/d, the complete waveform of the transmitted medium can be found by the use of propagator matrices (Aki and Richards, 1980). The wave variables of interest here are those at the top and bottom of a stack of layers. These are related by a product of propagator matrices, one matrix given for each layer. For waves travelling perpendicular through n layers, the relationship of the input and output wave is given by

$$\begin{bmatrix} S \\ W \end{bmatrix}_n = \Pi_{k=1}^n \mathbf{A}_k \begin{bmatrix} S \\ W \end{bmatrix}_1, \tag{2.110}$$

where S and W are the Fourier transforms of the wave variables σ and w, where these variables refer to different components of the displacement and stress variables depending on the polarization of the applied wave mode. For normal incidence P-waves, σ is interpreted as the normal stress across each interface, and w is the normal component of particle displacement velocity du_z/dt. For normal incidence S-waves, σ is the shear traction across each interface and w is the tangential component of particle velocity, du_x/dt or du_y/dt. Of course we are here assuming that the layering is horizontal.

For each layer k,the matrix $\mathbf{A}_k$ has the form

$$\mathbf{A}_k = \begin{bmatrix} \cos\left(\frac{\omega d_k}{V_k}\right) & i\sqrt{\rho_k M_k}\sin\left(\frac{\omega d_k}{V_k}\right) \\ i\frac{1}{\sqrt{\rho_k M_k}}\sin\left(\frac{\omega d_k}{V_k}\right) & \cos\left(\frac{\omega d_k}{V_k}\right) \end{bmatrix}, \tag{2.111}$$

where d_k is the thickness of the individual layer and M is the corresponding elastic modulus for the applied wave. Similar relations can be given for obliquely incidenting waves, see *e.g.* Aki and Richards, 1980).

The propagator theory has only been briefly covered in this section, and will not be used in the following chapter covering the large scale properties of well data interpreted as thin-layered layered media. However, some observations of differences between wavefields measured in the thin-layered model and in the homogeneous replacement medium in that chapter can be explained by referring to figure 2.5, showing how the wavelet in the measured signal varies from the small to the large λ/d-ratio models:

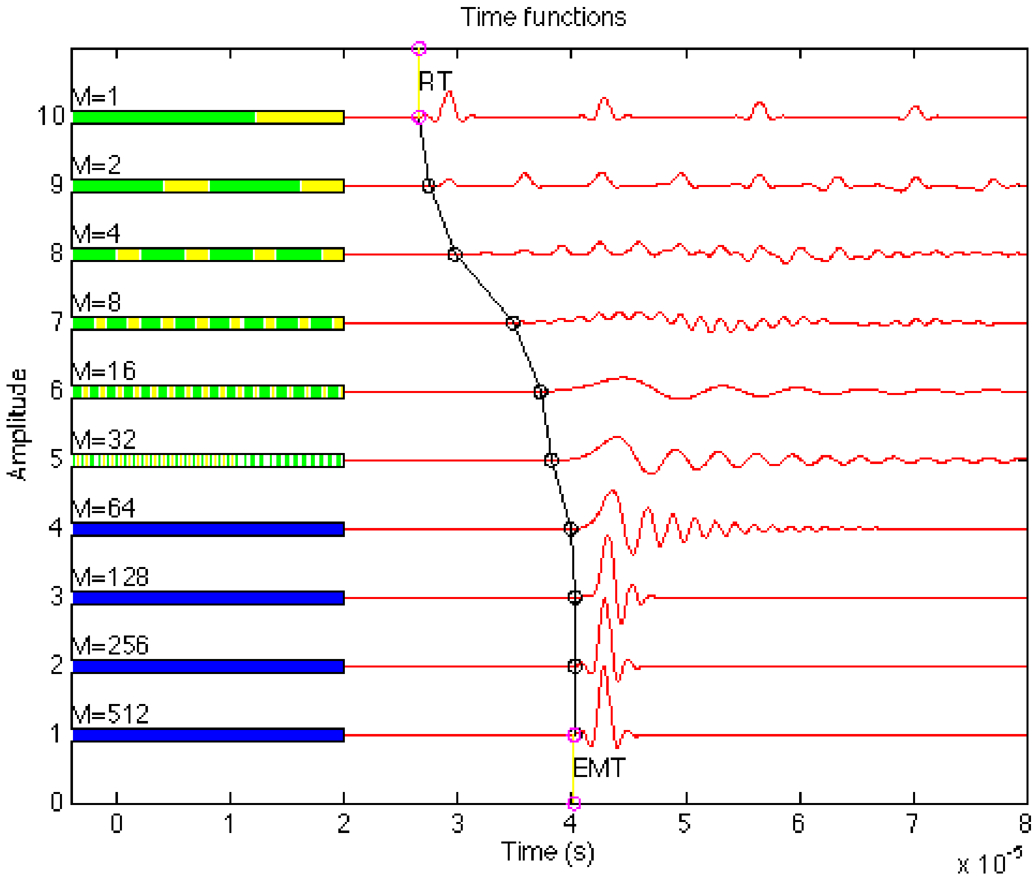

Figure 2.5: The transition from ray tracing velocity limit (average slowness) to effective medium velocity limit (iso-stress), modelled by the wave propagator operator on a two-phase layered medium with increasing λ/d ratio. (From Johansen, 1997).

All the two-phase layered models in this figure has the same ratio of the constituting two materials. From one model to the model below, each phase segment is cut in half and mixed, creating series of models where the layer thickness decreases exponentially.

For the upper thick-layered model, the recorded wave contains the directly transmitted wave and succeeding easily identifiable multiples or peg-legs caused by the intermediate interface. For the models below the number of internal interfaces increases, and for each added interface, more energy in the direct wave is reflected. As a result, the amplitude of the direct transmitted wave decreases, resulting in an energy transfer from the front of the wave and adding it back later in the signal. The result is a phase-change and time-delay of the recorded signal. For a more detailed description of this phenomena, see the classic article by O'Doherty and Anstey(1971). According to Marion et al. (1994), if the periodic spacing is a multiple of one-half wavelength, socalled Bragg scattering occurs, prohibiting the wave to propagate. Frequencies corresponding to such λ/d-ratios are thus filtered out. Bragg-filtering may explain some of the frequency changes observed in the received signal. Observing the models 1 to 4 in this figure, those with the largest λ/d-ratios, , it is seen that for all these models the received signal has a first arrival corresponding to the velocity of the Reuss-averaged medium. The recorded wavelet in model 1 is identical with the wavelet recorded in layer 10, except from a larger amplitude in the former due to of the lack of multiples. The signal wavelet recorded in model 4 has little similarity, however, with that of model 1. Variations in the recorded wavelet must therefore be taken into consideration as long as the λ/d-ratio does not exceed a sufficiently large value that is far below the λ/d-ratio where the Reuss-averaged velocity is a good estimate of the effective velocity.

Chapter 3

Upscaling of well data

3.1 Introduction

The medium representations in the previous chapter are all idealizations of reality. In the idealized case, the infinitesimal homogeneous volume is considered to be the fundamental element. From this simple medium more complex models are constructed by assigning different homogeneous properties to different subspaces, introducing interfaces, and allowing the functions within each subspace to vary as differential functions. But still, in the idealized case, when observing infinitesimal elements within any of the subspaces, such elements may be considered homogeneous.

In nature, this assumption of infinitesimal homogeneity is not obvious. Indeed, what is found, is that apparently homogeneous objects, when inspected on a finer scale, turn out to be heterogeneous. For example, a sample of siltstone appearing to be totally homogeneous to the naked eye, may reveal to consist of small quarts grains and thin mica flakes and display small-scale sedimentary structures when subjected to microscope inspection, as displayed in *e.g.* “Atlas of sedimentary rocks under the microscope” by Adams et al. (1984). Thus, whether a medium is considered homogeneous or heterogeneous depends on the resolution of the applied measurements. Large scale measurements record the average properties of the medium in large volumes or surfaces at the location of each measurement or *sample*. If these volumes contain an equal distribution of small scale heterogeneities in each sample, the resulting sample values in the large scale measurements indicate that the medium is homogeneous. Thus a given medium may be considered to be heterogeneous on small scale and at the same time homogeneous on large scale, where the small scale heterogeneities determines the large scale property, discussed in general by *e.g.* Hudson (1991).

Modelling and inversion thus involve considering *effective* media with a parameterization valid for the scale of measurements. The resolution in the mapping of effective parameters from seismic inversion is determined by the wavelength λ applied in the seismic survey. The Rayleigh resolution limit defines the minimum thickness for identifying a layer as a separate unit, discerning it from adjacent layers, to be $\lambda/4$. Alternatively the Widess limit of $\lambda/8$ may be considered to be the minimum discernable thickness. For any of these limits, with a dominant frequency in seismic data corresponding to wavelengths exceeding 100 m in a reservoir zone, the surveyor, interested in small scale features such as cracks and thin shale layers affecting the production properties of the reservoir, is clearly interested in how such features below the seismic resolution affect the overall properties of the large scale medium and whether it is possible to get information about the small-scale features by looking for associated characteristic properties in the large scale data.

The parameter mapping from small to large scale properties is the subject of upscaling and is the issue of the current chapter. Basically there are two reasons for upscaling. The first reason is to study the mentioned relation between small and large scale properties, making it possible to compare a model represented on a fine scale, generated *e.g.* from high resolution borehole measurements, with a model based on interpretation of large scale seismics. The second reason is the reduction of time and computer capacity needed for numerically simulating wave propagation through a spatial model of which the property resolution is reduced by upscaling.

The focus of the upscaling discussion in this chapter, is the transformation of borehole log data, which is sampled every few decimeters and where each sample is representative for an accordingly small volume of rock, to a scale that is more appropriate for low frequency seismic surveys.

For the input data, the discrete samples are interpreted as representing the properties of thin homogeneous layers. This layered medium may be smoothed by averaging functions to produce an upscaled medium. I will study the effect of smoothing the small scale properties in different domains, such as P- and S-velocity domain versus the domain of elastic constants, as well as discussing the effect on the upscaled parameters of selecting different shapes and sizes of averaging windows in the applied smoothing functions, comparing *e.g.* the box-car versus the triangle-shape Bartlett window. While the input media in the provided examples are isotropic, I will consider both isotropic and transverse isotropic versions of the resulting upscaled media. The transverse isotropic model is generated by Backus smoothing of the thin-layered model, of which procedure was discussed in the previous chapter.

Two data sets are operated on in this chapter. The first set is a borehole data set from an authentic well, where the given data log is described in the next section, while the second data set is entirely synthetic, generated to represent a periodic bi-layered medium. The effect on the effective parameters by choosing different smoothing window shapes will be shown on the real data set only, while both data sets will be used to display effects on the upscaled medium by choosing different parameter domains for the involved smoothing of the small scale data. The final part of the chapter contains data from wave field simulations in the original and the different replacement media to evaluate the validity of the different proposed upscaling functions. For this last part, I have chosen to focus on the upscaled models of the synthetic data, thus focusing on the evaluation of the different upscaling functions applied on this data, *i.e.* the comparison of the Reuss-, Voigt-, slowness- and velocity-smoothed isotropic replacement models and the Backus smoothed anisotropic replacement model.

3.2 The input borehole data

When wells are drilled, wire-line logs are acquired for a variety of physical parameters in the borehole. This procedure involves lowering a sonde with sensors down the hole by a cable, taking samples of electrical, acoustic and radioactive properties. Properties such as temperature and borehole size are also measured. The borehole data I will use in the current study are those directly associated to elastic wave propagation, *i.e.* the average density log and the measured P- and S-wave velocity.

Given input data is plotted in figure 3.1. In addition, the calculated V_P/V_S-ratio is plotted. The depth range of the plotted data is from 3570 to 3900 m, and as observed in the figure, parameter variations occur on several scales above the resolution limit given by the sampling density and the measuring tool. The smallest scale property variations, in terms of spatial frequency, which are visible in this figure, are those found *e.g.* in the density data in the deepest interval I-4. Compared to the rest of the data, this segment has a nearly constant density of 2.5 g/cm^3, except from the very short wavelength variations. In the depth interval I-3 the same characteristic small scale features are observed in the density data, but now superpositioned on a function that is slightly increasing with depth. These small scale variations will be further investigated shortly. Except from the sharp shift in density values at the interface between I-3 and I-4, the density log has no large-scale variations in the lower two segments. Large scale variations are however found in the P-velocity log for these two segments. Here the velocity function is seen to have a wave-like characteristic, with a wavelength

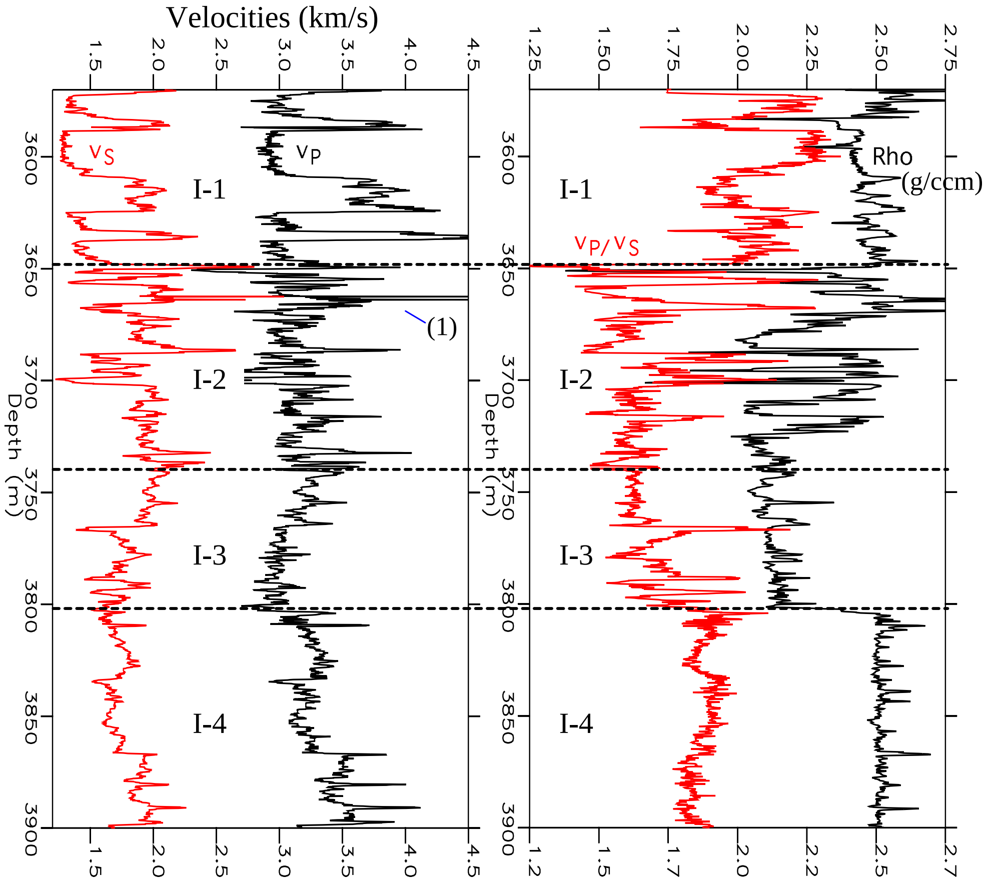

Figure 3.1: Original well data. The well is divided into four segments I-1 to I-4 based on the overall log appearance. The P-velocity data within box (1) is also plotted in figure 3.2.

of approximately 75 m. Observing the shallower segments, different shapes of large-scale variations are found. At about 3600 m, the two velocity logs indicate the presence of 25 m thick layers with alternating high and low velocities, on which the mentioned small scale variations are superpositioned.

For a geologic interpretation of the data, the V_P/V_S-log is a useful indicator for estimating the underlying rock properties. Contrary to the velocity-functions themselves, the V_P/V_S-ratio is a function solely of the bulk and shear moduli of the medium. These properties are determined by lithology as well as porefluid. For example, shales have low shear rigidity compared to sandstones, providing a higher V_P/V_S ratio for the former rocks (Tatham, 1982). Also a gas-filled rock has a lower V_P/V_S-ratio than an identical but brine-filled rock, since the fluid fill affects the effective compressibility of the rock but leaves the shear modulus unaffected.

Inspecting the displayed V_P/V_S-log, this ranges in value from 1.5 to 1.7 in the intervals I-2 and I-3, indicating possible reservoir properties, while the ratios in intervals I-1 and I-2 are at values of about 2.0, indicating a different lithology. Some high amplitude peaks, with a few meters wave length, , are found in interval I-2. A possible explanation for these peaks would be the occurence of shale layers present here in the elsewise sand-dominated interval.

The P-velocity for the 6 m interval contained in box (1) in figure 3.1 is also displayed in figure 3.2, now with the input sample points plotted in addition to the connecting lines that constituted figure 3.1. As seen in this figure, the sampling density is 8 samples per meter, *i.e.* a sampling interval of 12.5 cm. The figure shows that on this small scale, the log data has variations on the scale of individual log samples as well as on the scale of a few meters. The variations on the smallest scale may be observed on the left portion of the figure, in the depth range from 3662 to 3664.5 m. On the larger scale increase of parameter values in this interval, high frequency oscillations are imposed with an approximate wavelength of two sample intervals, the maximum frequency possible to represent in any discrete data. To the right of this segment the data show a smoother decrease in property values, lasting for 1.5 m or approximately 12 sample points. Then at 3666 m the log sharply increases in value before decreasing to the very right in a similar manner as the function increased to the very left.

The conclusion of the small and large scale log inspections is that the data may contain variations on decimeter scale, on the scale of a couple of meters and on the scale of tens of meters. The measured sediments may also have heterogeneities on smaller scales, but as stated in the introduction of this chapter, such heterogeneities are impossible to infer from the log data due to the sampling density and the measurement procedure. According to the sampling theorem, the spatial sampling density limits the maximum frequency

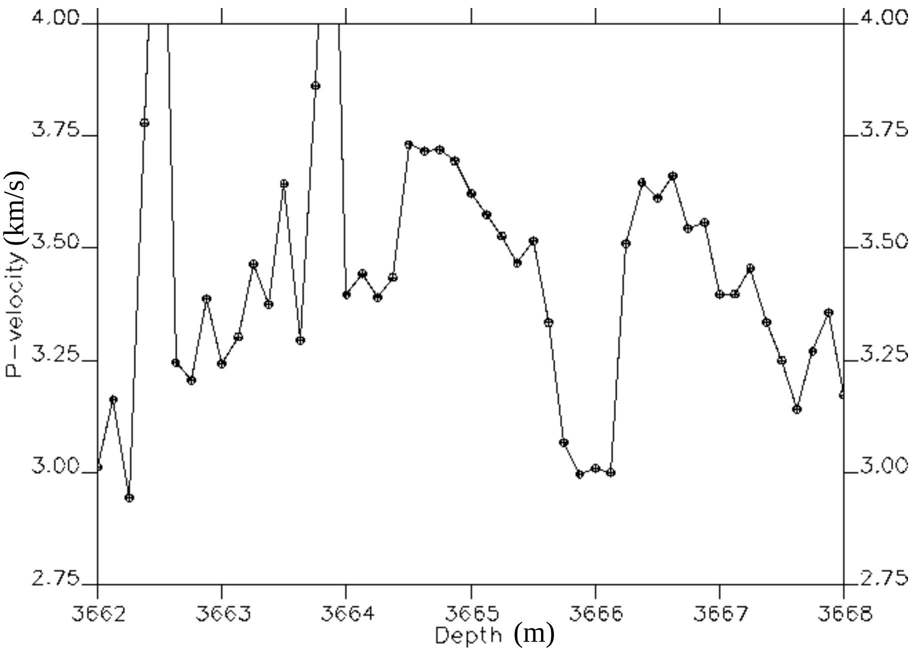

Figure 3.2: A close-up plot of the P-velocity data plotted within box (1) in figure 3.1.

of the sampled function. The minimum allowed wavelength of the sampled function is two times the sampling interval (Stark et al., 1988), corresponding to the Nyquist frequency. In cases where the input function contains spatial frequencies exceeding the Nyquist frequency, this must be low-pass filtered, or *anti-aliased*, to avoid distortion of the sampled data. It should be noted, however, that the input signal is already a band-limited signal, with maximum frequency given by the receiver distance Δz used when measuring the seismic traveltimes, or the bulk density for that matter of fact. At each sampling location the measured velocity of the composite material results from an averaging of slownesses or appropriate inverse elastic constants over the interval Δz, depending on the applied wavelength, as discussed in chapter 2. I will discuss the significance of the applied wavelength in the sampling in subsections 3.3.3 and 3.3.4. As a final remark, it should be noted that from the given input data, it must be assumed that the medium to be modelled is isotropic on the scale of sampling, *i.e.* there is no preferential orientation of the smaller scale heterogeneities. In subsection 3.3.4 I will discuss the effect of omitting transverse isotropic properties, caused by smaller scale layering that *are* present on the scale of initial sampling. Such anisotropy, however, only occurs if a sufficient long wavelength is used in the sampling operation.

Thus, the applied wavelength in the initial sampling may influence both the measured velocity and the registration of anisotropy. The implications of this will be better understood after the two-step upscaling procedures performed in subsections 3.3.3 and 3.3.4. Before this, however, I will study the effect of the shape and size of the smoothing window applied in the upscaling. This matter is relevant also for the tuning of the spatial sampling density in the logging process with the receiver interval Δz in the logging tool.

3.3 From small to large scale model

3.3.1 On the interpretation of log data samples

According to the previous chapter, a sampled log represents a discretization of a continuous function, of which spatial frequencies are limited by the process of measurement. With a finite number of samples, this continuous function cannot be reproduced exactly by applying the sampling theorem (Stark et al., 1988), but a continuous approximation to this function may be generated by applying some kind of interpolation technique. However, for studying the effect of large scale seismic waves by numerical processing, I find it useful to preserve the discretization given by the provided sampling, and instead of interpreting the log as a smooth continuous property function, each sample is interpreted as representing a thin layer with homogeneous properties, with layer thickness equal to the sampling interval in the log data. In this way, theories assuming homogeneous subspaces may be applied to simulate wave field propagation and calculate effective properties on larger scales. Such a layered model corresponds well with the general assumption of layering and stratification of sedimentary basins. This layering may have various orientations, from horizontal sedimentation, which is usually observed, to crosslayering, easily incorporated in the numerical model by assigning dipmeter values to each sample point. Figure 3.3 displays two such 2-D geometric interpretations of the small log segment from 3662.5 to 3663.5 m, also included in the previous figure, now plotting the P-velocity samples and the interpreted corresponding layers in the x-z plane.

The physical response of a thin layered model approximation compared to that of a continuous property function model, may be compared to the difference between a finite integral of a continuous function in calculus compared to the corresponding Riemann sum of the discrete sampling. Clearly, the denser the function is sampled, the closer the Riemann sum approaches the finite integral. Similarly the denser the log is sampled, the more accurate the model and resulting simulations and upscaled parameters. The given

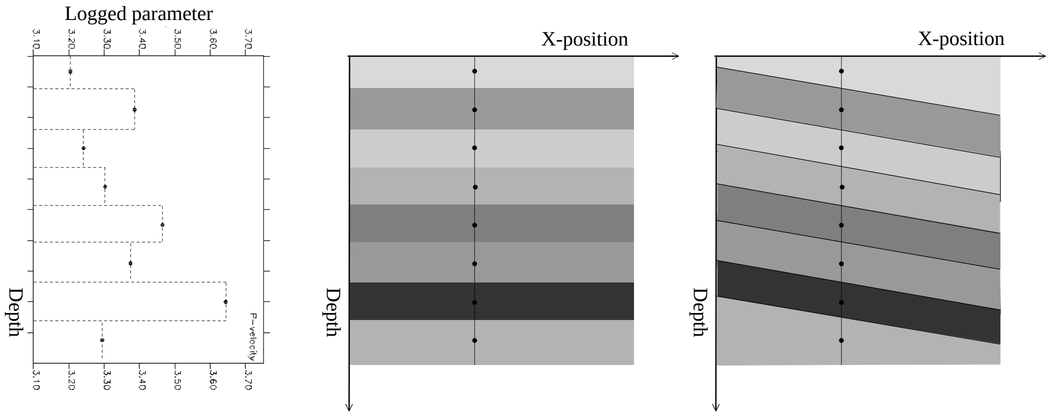

(a) 1-D thin layer interpretation. (b) 2-D horizontal layer interpretation (c) 2-D dipping layer interpretation

Figure 3.3: The samples are interpreted as thin layers in the x-z plane. In a) the layering is horizontal and in b) dipping.

log data may be resampled using an interpolation function to produce such a finer partition. However, for focusing on the effects of different upscaling procedures on a *given* small scale parametrization, I consider the conceptual model where each log sample is associated with a thin homogeneous layer as the given underlying small scale model.

3.3.2 Smoothing window effects

Any upscaling involves finding some kind of average vaues of the smaller scale parameters in the proximity of the location where the medium is to be upscaled. Since the large scale distribution of small scale parameter values often is non-uniform, estimating the upscaled properties for the entire large scale model by averaging the parameters in the entire small scale model is not a good approach. Such an upscaled model would, as a matter of fact, be entirely homogeneous. Instead, the upscaling is performed by running a smoothing window over the small scale model. Only the small scale samples within the window are included in the calculation of the associated upscaled sample, which is assigned the spatial location of the centre of the corresponding window, as displayed in figure 3.4.

In this figure 36 densely distributed input sample points are averaged by a smoothing window averaging four times four input samples for each output sample. The effect of the filtering function is determined by the size of the window and the internal weighting of the input samples in the involved averaging. In this figure, the sample interval of the output function and

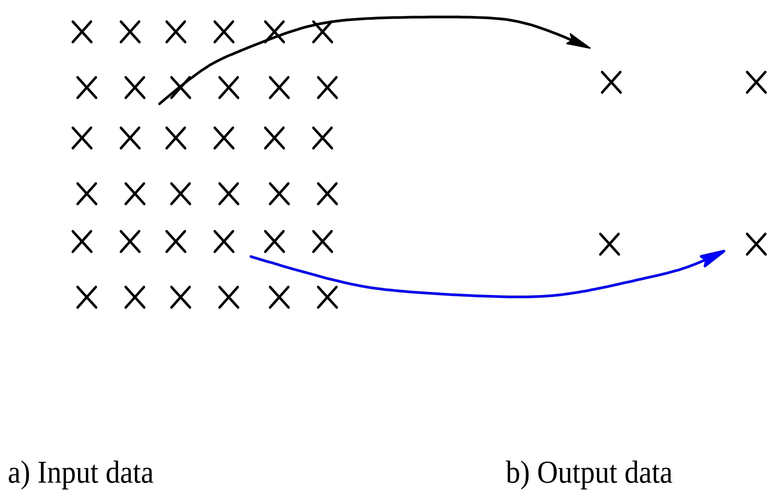

Figure 3.4: The moving average window determines which samples in the input data that contributes to each sample in the output data.

the smoothing window size are tuned to assure that the smoothing windows corresponding to adjacent output samples overlap. As I will come to later in this subsection, this is a matter of preventing possible aliasing of the filtered function, since the frequency content is specified by the window shape and size.

In this section, I will study the effect of applying different smoothing windows shapes and lengths on the well data presented in section 3.2.

Before starting to operate on the log data, a few remarks can be made from observing the smoothing effect of the four small scale data sets in figure 3.5. This figure is a scetch of four different input small scale functions along with hypothetical resulting moving average functions. In terms of upscaled parameters, it is seen that the functions in panel a) and c), respectively b) and d), are identical. For the set in a) and c), the high spatial frequencies in the input functions totally vanish in the smoothing, returning homogeneous output functions. For the two other input functions, these contain low frequency variations in addition to the high frequency fluctuations found in the two other data sets, and the output from the smoothing operations on these sets are functions with higher values in the intermediate range of the data.

Another feature is evident in this figure, however. Comparing the input data in panel a) with panel c), and similarly panel b) with panel d), though the output of these are identical, the input functions are different in terms

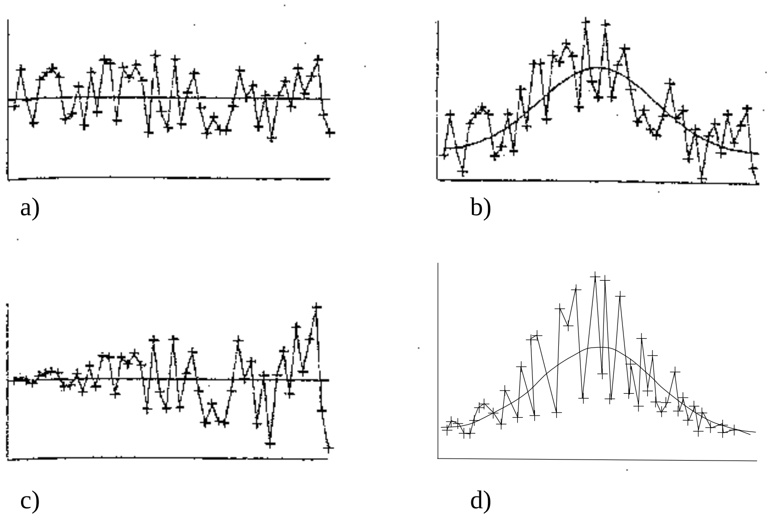

Figure 3.5: The effect of running a moving average window over four small scale functions. The resulting large scale function is unaffected by the small scale variability in the input functions. (Modified from Isaaks & Srivastava, 1989).

of local variability. The functions a) and b) has a constant variability, while this is not the case for the two other functions. In terms of elastic composite media, it is clear that such variations in local variability below the scale of the output effective medium may still affect the large scale properties. Indeed, a fundamental observation from the application of Backus smoothing was that the upscaled properties of a thin layered medium is anisotropic. Such layering may be produced by perturbing a constant function into increasing local variability, similar to that seen by traversing from left to the right in panel c). Thus, the overall elastic properties of the medium represented by panel c), is expected to change from isotropic toanisotropic characteristics from the left hand of the model and to the right. Accordingly proper upscaling nesseccarily involves more operation steps than just the smoothing operation. The smoothing process is nevertheless the focus of this section.

In signal analysis terms, the filtering of the function $f(z)$ to produce the output function $\langle f\rangle(z)$ is performed by the convolution of the input function with the filter response $w(z)$:

$$\langle f\rangle(z) = f(z) * w(z)\,. \tag{3.1}$$

In the continuous case, the convolution is defined as

$$\langle f\rangle(z)=\int_{-\infty}^{\infty} f(z')\cdot w(z-z')\,dz', \tag{3.2}$$

while in the discrete case it is represented as

$$\langle f\rangle_i=\sum_{j=-\infty}^{\infty} f_j\cdot w_{i-j}. \tag{3.3}$$

The functions to be discussed here, will involve one variable only. However, clearly the filtering often is performed on a surface or in a volume, requiring two or three variables. This extension is trivial, though, and since we will be focusing on 1-D well data, the one variable filtering is sufficient for our purpose.

The equivalent of this convolution in the space domain is the multiplication of the corresponding fourier-transforms. That is

$$\langle F\rangle(\kappa)=F(\kappa)\,W(\kappa), \tag{3.4}$$

where $F(\kappa)$ and $W(\kappa)$ are the Fourier transforms of the input function $f(z)$ and the filtering function $w(z)$, and $\langle F\rangle(\kappa)$ is the Fourier transform of the output of the filtering. Therefore, by studying the filter function $W(\kappa)$, information about the effect of the filtering on the different frequencies in the function given as input can easily be found.

In the continuous case the smoothing functions $w(z)$ with a window length A conform to the requirements that:

$$\begin{aligned}\int_{-\infty}^{+\infty} w(z)\,dz &= 1, &(3.5)\\ \int_{-\infty}^{+\infty} z\cdot w(z)\,dz &= 0,\ \text{and} &(3.6)\\ w(z)=0 &\qquad \text{for } |z|>A/2, &(3.7)\end{aligned}$$

which in the discrete case is equivalent to

$$\begin{aligned}\sum w_i &= 1, &(3.8)\\ i\cdot w_i &= 0, &(3.9)\\ \text{and } w_i &= 0 \text{ for } |i|>(N-1)/2. &(3.10)\end{aligned}$$

N is here the number of samples to be operated on by the smoothing function, and for simplicity I require N to be an uneven number.

The smoothing function $w(z)$ for calculating the pure arithmetic average is called the box-car window. This function is simply given by

$$w(z) = \begin{cases} 1/A, & z \in (-A/2, A/2), \\ 0, & |z| > A/2. \end{cases} \tag{3.11}$$

The discrete equivalent is:

$$w_i = \begin{cases} 1/N, & i = -(N-1)/2, \ldots, (N-1)/2, \\ 0, & |i| > (N-1)/2, \end{cases} \tag{3.12}$$

again assuming that N is an uneven number.

A more sophisticated smoothing function involves different weighting of the input samples dependent on the location of each input sample in the smoothing window. In this way, the input samples proximal to the location of the upscaled parameter contribute more to the averaged value than the peripheral ones. An example of this is the triangle-shaped Bartlett window, which is given by the function

$$w_{bart}(w) = \begin{cases} 0 & , |z| > A/2 \\ \dfrac{4}{A^2}z + \dfrac{2}{A} & , z \in (-A/2, 0] \\ -\dfrac{4}{A^2}z + \dfrac{2}{A} & , z \in (0, A/2] \end{cases} . \tag{3.13}$$

In the frequency domain, the filters corresponding to the two averaging operations are given by

$$W_{box}(\kappa) = \frac{\sin \pi A \kappa}{A \pi \kappa} = \operatorname{sinc}(\pi A \kappa), \tag{3.14}$$

$$W_{bart}(\kappa) = \left(2 \frac{\sin \dfrac{\pi A \kappa}{2}}{\pi A \kappa} \right)^2 = \operatorname{sinc}^2\left(\frac{\pi A \kappa}{2}\right). \tag{3.15}$$

From these functions it is clear that increasing the smoothing length A means compressing the filter function in the frequency domain. Also, $W_{bart}(\kappa) = W_{box}^2(\kappa)$ if the averaging length of the box-car window is half that of the Bartlett window. This means that the Bartlett window in the space domain may be expressed by the autoconvolution of the box-shaped window of half the smoothing size of the Bartlett window.

The two averaging windows and corresponding Fourier spectra are plotted in figure 3.6. As observed in panel c) of this figure, the first notch of the Bartlett filter is twice that of the box-car filter. Also, in the application of the Bartlett window, more of the frequency content is contained within this first filter notch. These differences in the frequency domain are explained in the space domain by the strong weighting of the central samples of the input function by the use of the Bartlett window. By increasing the smoothing length of the Bartlett window to $2A$, the notches of the two filters will coincide in the frequency domain. In figure 3.7 the resulting amplitude spectras are plotted, illustrating that applying smooth averaging windows in the space domain produces frequency windows with more of the energy concentrated to frequencies below the first filter notch. In this example, more energy is found in the sidelobes of the box-car filter than for the Bartlett filter. Such energies may produce undesirable aliasing when the filtered function is sampled.

According to the sampling theorem, to prevent aliasing the sampling interval Δx of the output function must be less than $\Delta x_{\max} = 1/\left(2f_{NY}\right)$, where f_{NY} is the maximum frequency of the output function. The input function, the one being smoothed, has a maximum frequency given by the input sample interval, and by maintaining this sampling density in the sampling of the output smoothed function, aliasing will be avoided. However, the point of upscaling is usually to coarsen the model representation, and thus the spectrum of the filter has to be considered to determine the maximum frequency of the output. Clearly some aliasing will occur when the sampling density is decreased compared to the input density, since the frequency spectra of both filters have non-zero amplitude values for frequencies ad infinitum. A filter cut-off frequency and the associated Nyquist frequency have thus to be *defined* to some value that is less than the theoretical maximum frequency of the output signal *before* it is samples. For the given filters, this cut-off frequency can conveniently be set to the first notch of the filter. Accordingly there may be some aliasing in the sampled output function due to energy in the filter outsite this cut-off frequency.

With the cut-off frequencies defined to be at the first notch, *i.e.* $\kappa_{NY,box} = 1/A$ and $\kappa_{NY,bart} = 2/A$, the associated minimum sampling intervals of the output data are

$$\Delta x_{\max,box} = A/2, \tag{3.16}$$

$$\Delta x_{\max,bart} = A/4, \tag{3.17}$$

according to the sampling theorem.

More sophisticated smoothing filters can be found in Mæland (1993). Obviously, the smoother averaging functions, the less aliasing. However, the application of smoother windows may require more calculations, thus reducing the time efficiency. The key here is thus to find the smoothing window fit for the specific purpose.

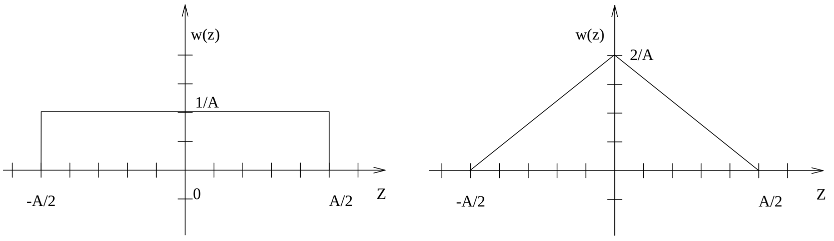

a) Boxcar window

b) Bartlett window

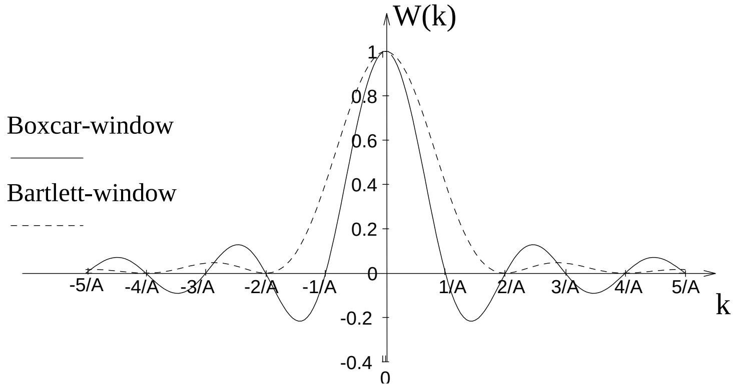

c) Fourier spectra of the averaging windows

Figure 3.6: The simple a) box-car and b) Bartlett averaging windows and c) their Fourier spectra.

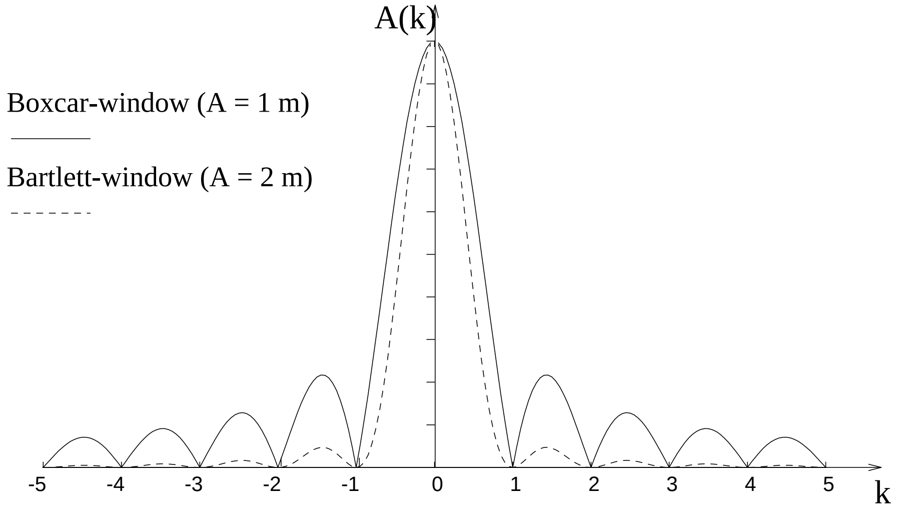

Figure 3.7: Comparison between boxcar window of length A and Bartlett window of length 2A.

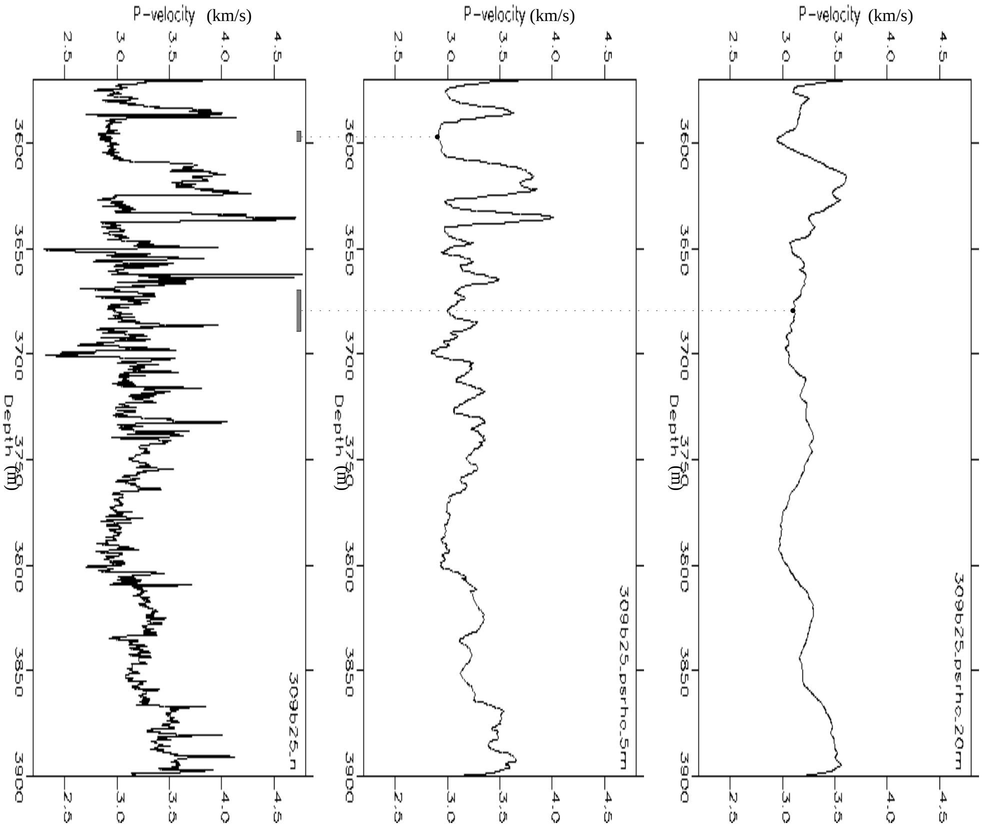

Original P-velocity log

Filtered P-velocity from using a 5 m boxcar averaging window

Filtered P-velocity from using a 20m boxcar averaging window

Figure 3.8: The result of smoothing the velocity log over 5 and 20 meters with a box-car window.

Figure 3.8 displays the effect of applying a 5 and a 20 m box-shape averaging window on the P-velocity log of the presented well data. The original data is plotted to the left, and those smoothed over five and twenty meters to the middle and right respectively. The effect of the window length on the decrease of frequency range in the output data is obvious. The five meter window has the highest cut-off frequency and thus preserves the most of the frequency content of the data. Here the energy corresponding to a few meters wavelength is filtered out, while the shape of stratigraphic features on the scale of ten meters and above is preserved. Applying a 20 meter averaging window, the largest scale fluctuations are also smoothed. The larger the smoothing window, the more homogeneous the output.This is well illustrated by observing the upper 60 meters of the logs, where *e.g.* the high velocity layer at approximately 3590 m is almost entirely smoothed out in the case of 20 m smoothing.

Since the dominant frequency of surface seismic surveys may be about 30 Hz and average P-velocity often exceed 3000 m/s, the wavelength of the wave propagating through the model is generally on the scale of 100 meters. According to the Rayleigh resolution limit, features of smaller scales than 25 m are then below the scale of resolution. Thus no harm is done to the data in terms of data resolution by smoothing out layers below this scale before performing wave propagation simulations.

However, the validity of the upscaling, given that the smoothing window is not too large, depends on that the smoothing is performed correctly, according to how the seismic wave "sees" the signal, by somehow preserving the effect on the propagating wave from the small scale variations that are filtered away in the large scale model. Referring back to panel c) in figure 3.5 on page 42, the large scale property was constant throughout the spatial model, while the variability was increasing. According to Backus (1962), the large scale medium will be isotropic on the left side and strongly anisotropic on the right side. Such features are preserved by smoothing the model in the appropriate parameter domains, from which effective parameters are calculated. This issue is the theme of the next section.

3.3.3 Parameter domain of smoothing

While size and form of the smoothing window are important parameters, probably the most important issue is the choice of data domains in which the small scale model is to be smoothed. In rock physics, different parameter domains are related. In chapter 2 I looked at the relations between parameters such as the elastic constants and the P- and S-velocities. Other data domains are those of porosity, density, fluid content and so on. Such relations may be given for small scale representations as well as for the upscaled models. However, since the relations between the domains are not linear, *e.g.* $V_P = \sqrt{c_{33}/\rho}$, the parameter domains cannot be smoothed independently. Instead, for each relation the dependent and free parameters must be selected, and the smoothing and subsequent calculations must be performed on the free variables.

The issue of this section is to observe effects of smoothing different parameter domains of which the elastic properties of the isotropic small scale medium and the upscaled medium can be considered to be a dependent function of. The isotropic model contains three free parameters, *e.g.* V_P, V_S and ρ, and thus three small scale parameter functions must be smoothed. The procedure may be described in general terms before defining the specific domains in which I will perform the smoothing operations later.

Letting the vector $\mathbf{m}_1 = (V_P, V_S, \rho)$ be the original valid representation of the elastic small scale medium, other valid representations may be given by a vector function $\mathbf{m}_2(z) = \mathbf{g}(\mathbf{m}_1(z))$, providing that the three components of $\mathbf{m}_2$ are independent. The $\mathbf{m}_2$ functions are then smoothed by the convolution with the averaging window, giving

$$\langle \mathbf{m}_2 \rangle (z) = \mathbf{m}_2(z) * w(z), \tag{3.18}$$

where the brackets represent a large scale parameter. After the smoothing process, the original domain large scale parameters may be found by applying a generalized inverse function $\mathbf{g}^{-1}$, *i.e.*

$$\langle \mathbf{m}_1 \rangle (z) = \mathbf{g}^{-1}(\langle \mathbf{m}_2 \rangle (z)). \tag{3.19}$$

In all the suggested upscaling domain sets, bulk density ρ constitutes one of the three free parameters, thus $\langle \rho \rangle$ is always found by applying the smoothing directly on the small scale density. Natural options for the selection of the remaining two free parameters are either the seismic velocities, the associated slownesses, the elastic constants or the inverses of these. Thus, I will consider the effect on the smoothed, directly or indirectly, P-velocity by smoothing the following parameters:

$$\begin{aligned} f_1(z) &= V_P, & \text{(3.20a)} \\ f_2(z) &= (1/V_P)(z) = S_P(z), \\ f_3(z) &= \left(V_P^2 \cdot \rho\right)(z) = c_{33}(z), \\ f_4(z) &= (1/c_{33})(z), \end{aligned}$$

The averaged functions are then given by:

$$\begin{array}{ll} \langle f_1 \rangle = \langle V_P \rangle & \text{(velocity average)}\,, \\ \langle f_2 \rangle = \langle 1/V_P \rangle & \text{(slowness average)}\,, \\ \langle f_3 \rangle = \langle V_P^2 \cdot \rho \rangle & \text{(Voigt average)}\,, \\ \langle f_4 \rangle = \left\langle 1/\left(V_p^2 \cdot \rho\right) \right\rangle & \text{(Reuss average)}\,, \end{array} \tag{3.21}$$

and the effective velocity may follow from the corresponding inversions:

$$\langle V_P \rangle_1 = \langle f_1 \rangle\,, \tag{3.22}$$

$$\langle V_P \rangle_2 = 1/\langle f_2 \rangle\,, \tag{3.23}$$

$$\langle V_P \rangle_3 = \sqrt{\frac{\langle f_3 \rangle}{\langle \rho \rangle}}\,, \tag{3.24}$$

and

$$\langle V_P \rangle_4 = \sqrt{\frac{1}{\langle f_4 \rangle \cdot \langle \rho \rangle}}\,. \tag{3.25}$$

The functions f_1, f_2, f_3 and f_4 are not linearly related, and the results of the different smoothing options are therefore different. This will now be illustrated by applying the four smoothing functions on a model of periodic layers with strongly contrasting velocities. The layers of this model are ten meters thick, the P-velocities alternates between 5 km/s and 3 km/s, and corresponding S-velocities are 3 km/s and 1.5 km/s. Though such an extremely contrasted medium is not likely to be found in reality, a periodic layering of shale and limestone would produce similar properties. The model is thus called the lime-shale model. The lime-shale model, which on large scale is entirely homogeneous, will also be used in the following sections to illustrate effects of anisotropy caused by the thin layering and the effect of the different upscaled models on propagating wave fields.

Figure 3.9 displays the P-velocity function of the input lime-shale model, along with the resulting upscaled velocities. The input model has been smoothed over the entire depth range, providing homogeneous output functions. Each layer type constitutes half of the entire medium. Therefore, the average-velocity model has a P-velocity given by

$$\begin{aligned} \langle V_P \rangle_1 &= 0.5 \cdot 5 \text{ km/s} + 0.5 \cdot 3 \text{ km/s} \\ &= 4.0 \text{ km/s} \end{aligned} \tag{3.26}$$

The average slowness is the basis for calculating travel-times in the ray-tracing cases where the wave length is much shorter than the layer thickness and the ray path is perpendicular to the layering. The basis for the application of average-slowness smoothing is that the total traveltime for waves is the sum of the traveltimes through each layer. In section 3.4, where waves are propagated through the models, we will show that for high frequencies the wave field in the average slowness model has a good correspondence with that in the small scale original. The average slowness of the given model gives the effective P-velocity by:

$$\begin{aligned} 1/\left\langle V_P \right\rangle_2 &= 0.5/\left(5 \text{ km/s}\right) + 0.5/\left(3 \text{ km/s}\right) \\ &\Updownarrow \\ \left\langle V_P \right\rangle_2 &= 3.76 \text{ km/s}. \end{aligned}$$

On the other hand, this average has also been used for calculating effective velocities in porous media by weighting the slowness of the matrix and the pore fluid according to the given porosity (Wyllies equation). This application has no theoretical support however, cf. Mavko et al. (1993).

To predict the actual effective properties of a composite medium, in addition to the volume fractions of the constituting materials and the elastic properties of these components, the geometric details of how the constituents are arranged relative to each other must be considered. The upper and lower bounds for the effective medium when exact arrangements are unknown, are given by the Voigt and Reuss bounds (Mavko et al., 1993).

The Reuss average involves averaging the inverse of the elastic modulii. This is termed the isostress average, assuming a uniform stress on the individual components. This smoothing is proved to be accurate for finding effective properties of fluid suspensions as given by Wood's formulae (Mavko et al., 1993) and also shows a good approximation for "soft pore shapes". For example, when long waves propagate perpendicular to the layering of a thin-layered medium, the stress upon each layer may be considered to be levelled out as the wave passes, corresponding to Reuss averaging (Marion et al., 1994). The calculated Reuss average for the given model gives a P-velocity of 3.64 km/s, approximately 0.125 km/s lower that of the slowness averaged P-velocity.

On the contrary, for "stiff pore shapes" the effective properties approach the upper Voigt average found by averaging stiffnesses or elastic constants. The Voigt limit for the P-velocity in the current example is found to be 4.14 km/s.

The Reuss and Voigt limits make a theoretical range for the effective P -velocity for models of the given components of as much as 0.5 km/s. Within this range the two other presented averages are found.

According to Mavko et al. (1993), a requirement for stating that Voigt and Reuss constitutes the bounds of possible effective properties, is that the rock is isotropic. Backus (1962) showed however that a thin-layered media has transverse isotropic properties on large scale. Thus it can be questioned whether the given limits actually applies to the thin-layered case. This question will be raised in the next section considering the result of Backus smoothing the well data presented in section 3.2.

I will now display the effect of smoothing the given well data in the four different parameter domains just presented. The smoothing operations are performed by applying a 5 and a 20 m box-car smoothing window, and the resulting effective P-velocities are plotted in figure 3.10 along with the original data for the depth-range 3575 – 3750 m.

From inspecting the curves, it is seen that the difference between resulting parameter values from smoothing in different domains generally increases with smoothing length. Compared to the spread of the four curves from the 20 m smoothing, the curves from the 5 m smoothing appear to coincide better, except for a few intervals, in specific the segments about 3650 and 3700 m, where the effective P-velocities differ with as much as 0.2 km/s from one curve to the other.

The reason for the increase in sensitivity of selected smoothing domain with increasing smoothing length, is believed to be the increased variability within the smoothing window. That is, with increased window length a larger proportion of the medium within the window has property values that differ from the average property value within the window.

This variability exists on several scales as discussed in section 3.2. When the data is smoothed over 20 m, it is expected that both small scale variability, only visible in the original data, as well as intermediate scale variability, which is visible in the 5 m smoothed data but smoothed out in the 20 m smoothed data, will contribute to the mentioned sensitivity. The question is however which of these scales of variations that contribute the most.

To answer this question, I performed four two-step smoothing operations on the provided data. The data were first Reuss- and Voigt smoothed over 5 m. The resulting two logs were then used as input to 20 m Reuss- and Voigt smoothing operations, producing four different large scale datasets.

Figure 3.11 displays the resulting P-velocity curves and is used to illustrate the ratio between the contribution to the smoothing domain effect from intermediate scale versus small scale variations. Here the curve couples (1) and (2) and couples (3) and (4) are the results from Reuss- and Voigt averaging over 20 m the priorly Reuss- and Voigt averaged data over 5 m, while curves (5) and (6) represent the one-step 20 m Reuss- and Voigt averaged data, also displayed in the previous figure.

Two main observations are made from this figure: First the Reuss and

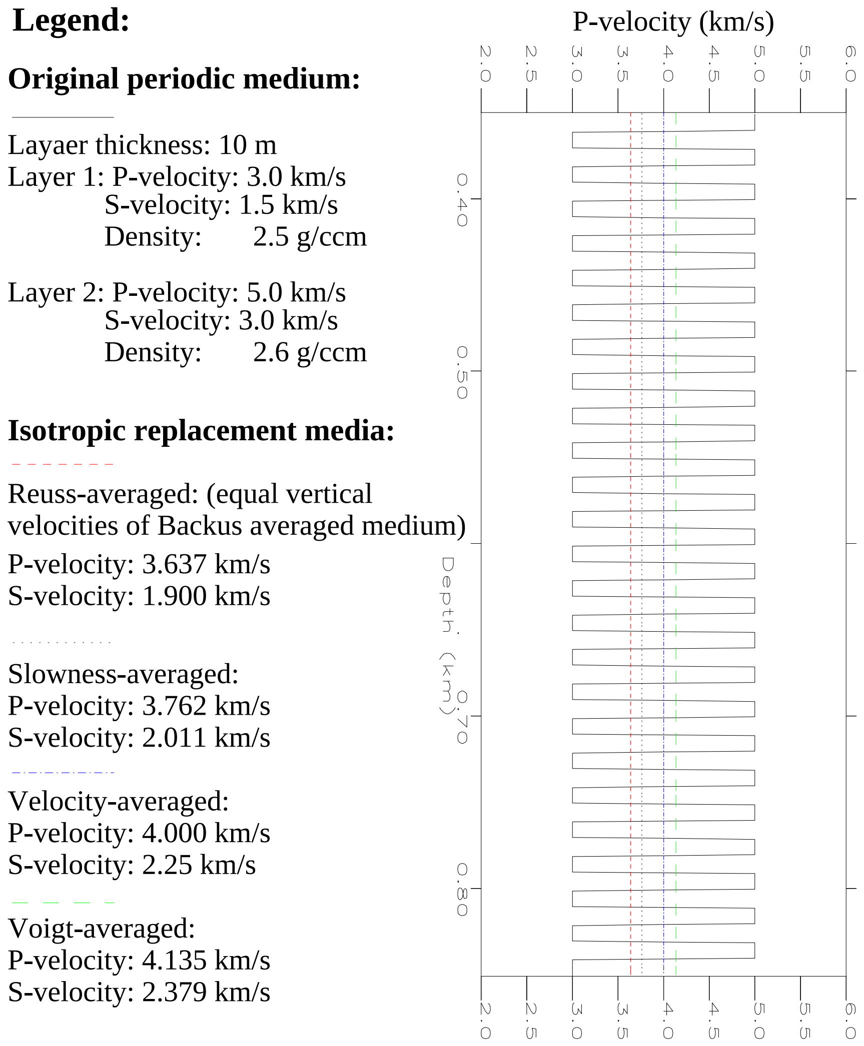

Figure 3.9: A 1-D graphical representation of the P-velocity of the "lime-shale" bipartite medium and the velocity of the four different replacement media.

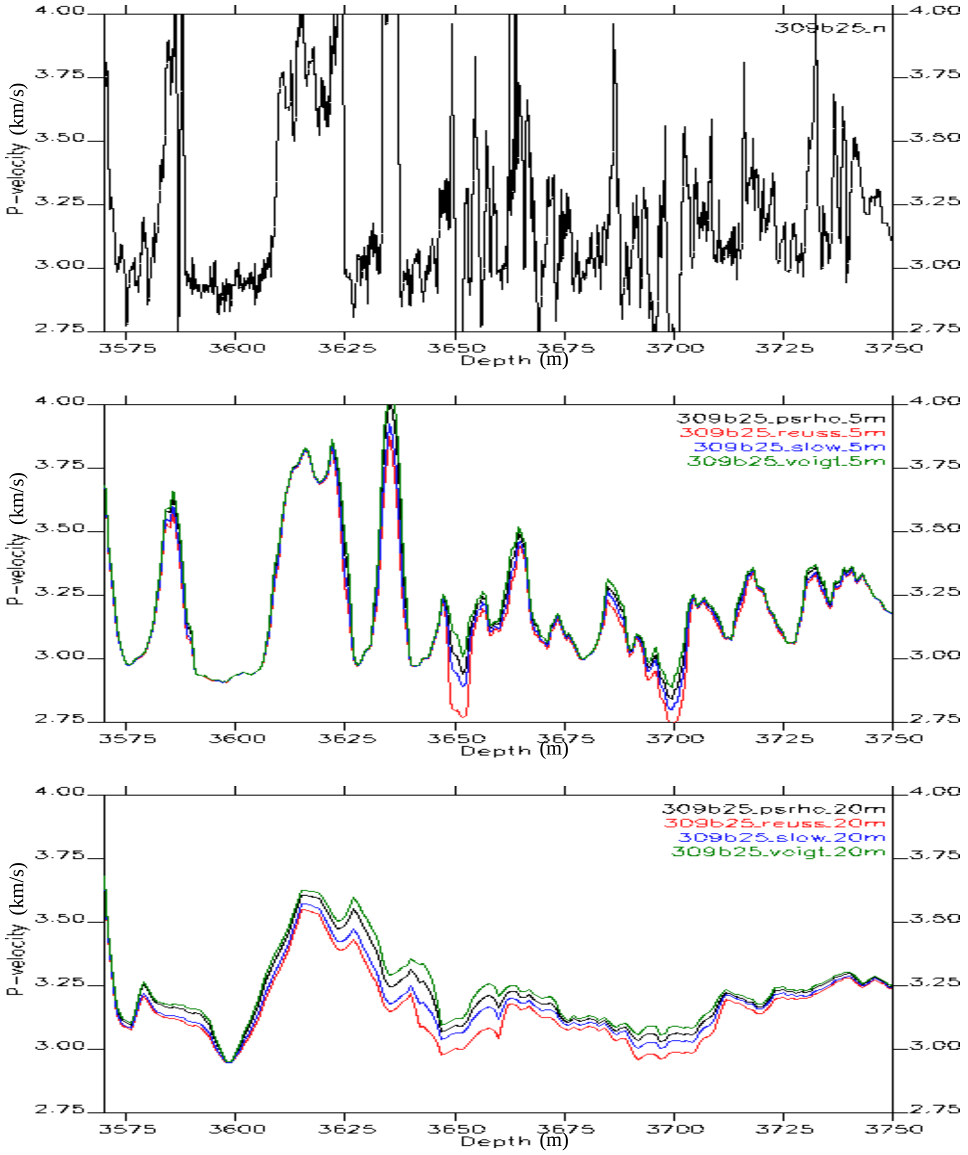

Figure 3.10: The effect of smoothing with respect to different parameters. (Reuss-, Voigt-, slowness- and velocity averaging).

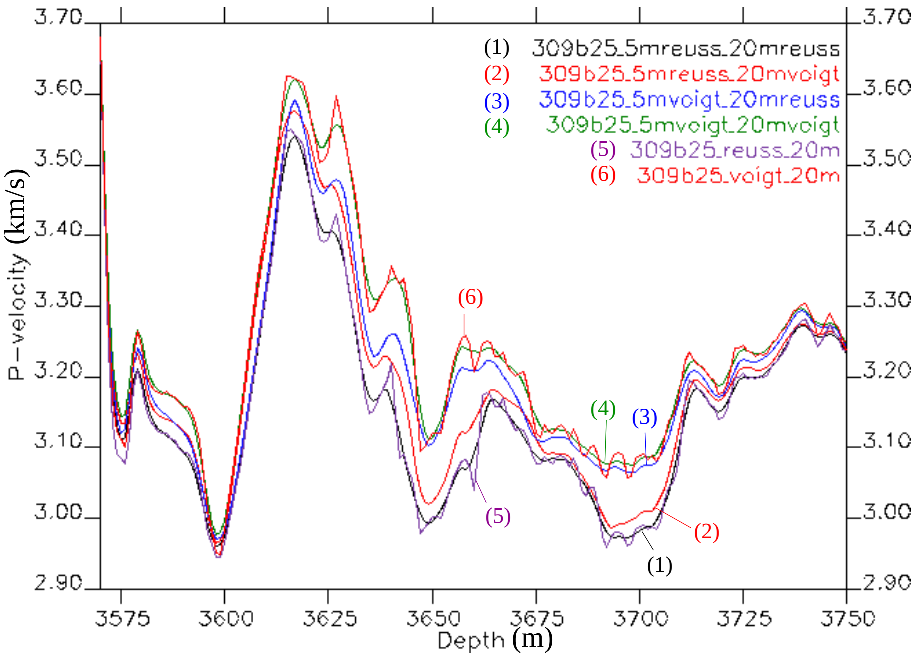

Figure 3.11: Two-steps smoothing combinations of Reuss and Voigt averaging shows that the small scale variability contributes the most to the effect of smoothing with respect to different parameters

Voigt large scale (20 m) upscaled properties of a previously intermediate scale (5 m) upscaled data set appear to differ less from each other, *i.e.* are less sensitive to the domain-effect, than the corresponding one-step upscaled (20 m) properties of the underlying small scale data, and secondly, the curves (1) and (4) appear to be low-pass filtered versions of the one-step filtered data given by (5) and (6).

Regarding the second observation, it is known that the sequence order of filters applied to a signal is arbitrary. Thus, the order of the two smoothing filters can be switched, applying the 20 m filter prior to the 5 m filter, without changing the filter response of the composite filter. The log represented by curve (5) and (6) would thus equal those of curves (1) and (4) by smoothing the former set with a 5 m smoothing window in the appropriate parameter domains.

The difference between curve (1) and (4) therefore represents the smoothing domain effects from both small and intermediate scale variations. Identifying the intermediate variations to account for the differences between the Reuss and Voigt 20 m smoothed data of the priorly 5 m smoothed data, *i.e.* the differences between curves (1) and (2) and curves (3) and (4), and comparing these differences with that between (1) and (4), it is seen that most of the smoothing domain effect is caused by the small scale variations.

One lesson from the observations of the curves in this figure, is thus that if a parameter set is to be upscaled by smoothing, but the modeller is unsure which parameter domain the data set is to be smoothed in, the modeller should apply the shortest possible smoothing window. Assuming that the propagating wave senses or "sees" the average properties of the medium corresponding to a Reuss average over 20 m, using the priorly 5 m Voigt smoothing data in a simulation model would thus cause the wave to sense the large scale properties in the simulation model given by curve (3). On the other hand, had the correct priorly 5 m Reuss-upscaled model been used, the large scale wave would "sense" the properties given by curve (1). But again, the starting point for the simulation could be worse could be worse: If the data have been upscaled by a 20 m Voigt averaging prior to the simulation, the Reuss smoothing wave would see the 20 m Reuss average of the data given by curve (6). Obviously the parameters "sensed" by the propagating wave after such an upscaling, which must be close to curve (4), differs more from the correct large scale properties represented by curve (1) than the parameters "seen" by the propagating wave subsequent to the corresponding upscaling using the smaller window.

The second lesson is a general caution regarding the quality of input data to a model, an issue I touched on in section 3.2. As we know, all model parameters are effective properties on some given scale, including the input data where the scale is determined by the measurement process. Though they are unmeasurable by the measurements applied, we may assume that the medium contains heterogeneities on smaller scales than those found in the input data.

In a hypothetic case we may consider the smallest measurable scale to be that of the 5 m smoothed data, while the properties in nature itself is *given* by the small scale representation of decimeters. The "measured" well data in this case is thus a 5 m smoothed version of the small scale "nature". The process to be studied is a long wavelength wave propagation where the wave "sees" the Reuss averaged elastic properties within a 20 m window. In "nature" this wave thus senses the 20 m Reuss average of the actual medium, *i.e.* it sees curve (5). On the other hand, in a simulation this wave will sense the corresponding 20 m average of the intermediate scale model input data. If the model is given by the 5 m Reuss average, the simulated wave will thus sense curve (1), a good estimate of curve (5), while if the input data is the 5 m Voigt averaged properties of the "true nature", the propagating wave in the following simulation will sense the effective properties of curve (3), producing simulated data differing more from an actual field survey of "nature".

As stated in section 3.2, the sampling of a physical medium at a given location involves averaging the smaller scale properties within the sampled volume. Now according to the theory of effective medium velocities, as outlined in chapter 2, this average will be different depending on the wavelength used in the sampling (Marion et al., 1994). From the previous paragraph it should be obvious that to construct a correct seismic model, the wave used in the small scale data sampling must smooth the smallest scale heterogeneities the same way as the large scale wave, which is to be simulated, smooths these microscopic heterogeneities in the real medium. Thus, if the large scale wave smooths the medium by Reuss-averaging, a sufficiently long wavelength also needs to be used in the sampling of the medium to smooth properties on scales that are averaged out in the sampling accordingly.

To sum up this argument: A large scale Reuss averaging of previously slowness averaged properties will, according to this two-step upscaling example, give a different result than the same large scale upscaling of previously Reuss averaged properties. Thus an appropriate question that should be raised is whether given input data from well logs does provide the correct average of the micro-scale properties and thus provides the basis for successfull further upscaling and simulations. This question is left open for others to investigate.

In the following section a similar question will be raised regarding the matter of isotropy versus anisotropy in the input data. Due to limited measurements, input data are most often presented and processed as if they are by default isotropic. In the next section I will look at the anisotropic large scale properties of such isotropic small scale media, but it is also proper to question what effect omitting intrinsic low scale anisotropy in such upscaling has on the behaviour of the model.

3.3.4 Applying Backus averaging

As outlined in chapter 2, a thin layered isotropic medium with nearly constant statistical properties when averaged over an interval l, can be replaced by a transverse isotropic medium with parameters calculated by Backus averaging over this interval. The resulting transverse isotropic medium is then equivalent to the original medium for wavelengths much larger than l. It is shown that the velocities along the symmetry axis of this replacement medium is equal to that of the Reuss averaged medium, while velocities in other directions are generally different.

Referring to the notation of the introduction of the previous subsection, Backus averaging involves smoothing the multi-component function $\mathbf{g}\left(\mathbf{m}_1\right)$, where $\mathbf{m}_1$ represents the low-scale parameters. The elastic properties of the upscaled medium are then a function of $\langle \mathbf{g}(\mathbf{m}_1) \rangle$. The smoothing window size and shape has in the previous sections been shown to influence the upscaled medium in terms of smoothness, *i.e.* in the spatial frequency content. The size of the smoothing window has also shown to affect the sensibility of the resulting upscaled medium from the choice of parameter domains, $D_\mathbf{g}$, where the smoothing is performed. In the current section, I will therefore study the effect on the anisotropic characteristics of the replacement media by increasing the smoothing length in the Backus smoothing.

The given well data have thus been Backus smoothed over 5 m and 20 m, and a selected set of the resulting parameters is displayed in figures 3.12 and 3.13.

In panel a) of the two figures the calculated vertical and horizontal P-velocities are plotted, *i.e.* the velocities normal and parallel to the small scale layering. In addition the P-velocity of the corresponding Voigt averaged medium, found in the previous subsection, is plotted for reference. From the plotted 180 m long interval, two 10 m segments have been enlarged to make possible a closer inspection. Note here that the scales of these windows are not identical everywhere. In the b) panels the corresponding Thomsen parameters have been plotted.

As expected from the previous sections, in addition to aquiring smoother effective velocities by applying a larger window, the difference between horizontal and vertical P-velocity is generally greater in the 20 m smoothed case than in that of the 5 m smoothing. This difference is reflected in the corresponding Thomsen parameters. While the Thomsen parameters from the 5 m smoothing have local peaks exceeding those of the 20 m smoothed medium, *e.g.* the case of the ε parameter at the depth of 3650 m, for most depths the Thomsen parameters of the 20 m smoothed medium are the largest.

The vertical P-velocity from applying Backus smoothing is equal to the velocity of the corresponding Reuss smoothing, since the effective C_{33} parameter in both cases are given by

$$C_{33} = \left\langle \left(\rho V_P^2\right)^{-1} \right\rangle^{-1}. \tag{3.27}$$

The horizontal P-velocity, $V_{P,90}$, of the Backus medium when the vertical velocity $V_{P,0}$ and the Thomsen parameter ε is given, is given by

$$V_{P,90} = V_{P,0} \cdot (1 + \varepsilon). \tag{3.28}$$

This relationship accounts for the large differences between vertical and horizontal P-velocities in the 5 m smoothed data at the depths of 3650 and 3700 m, where ε has unusually large values.

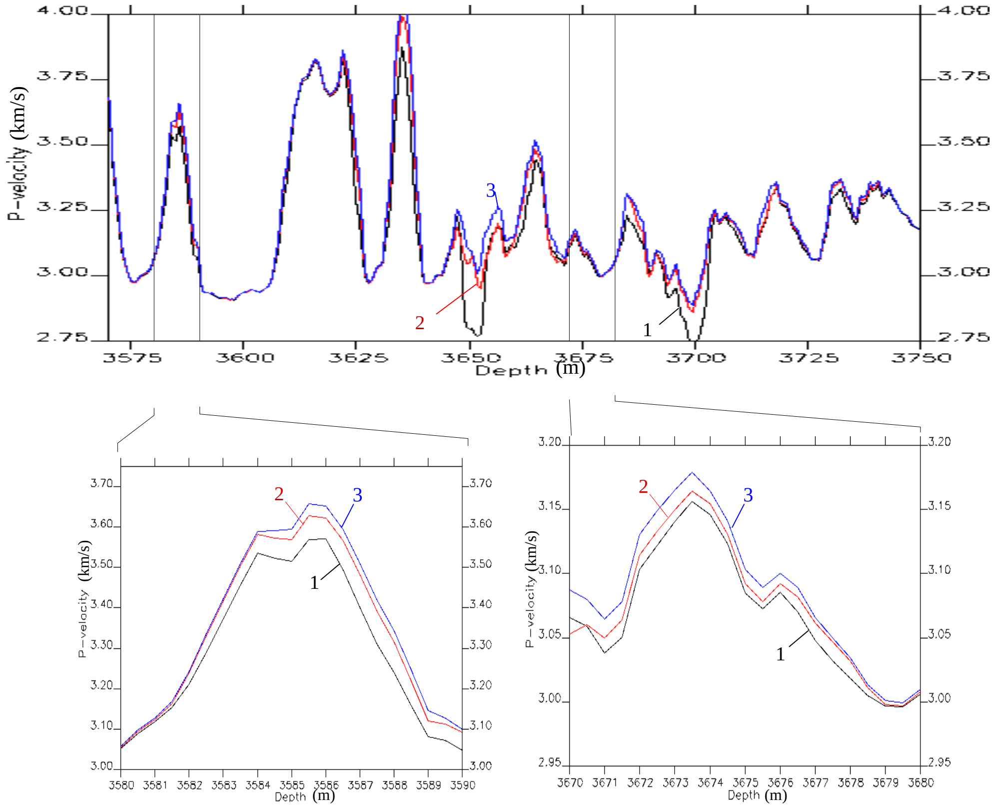

a)

1) Vertical P-velocity (Backus 5 m)
2) Horizontal P-velocity (Backus 5 m)
3) P-velocity from Voigt smoothing (5 m)

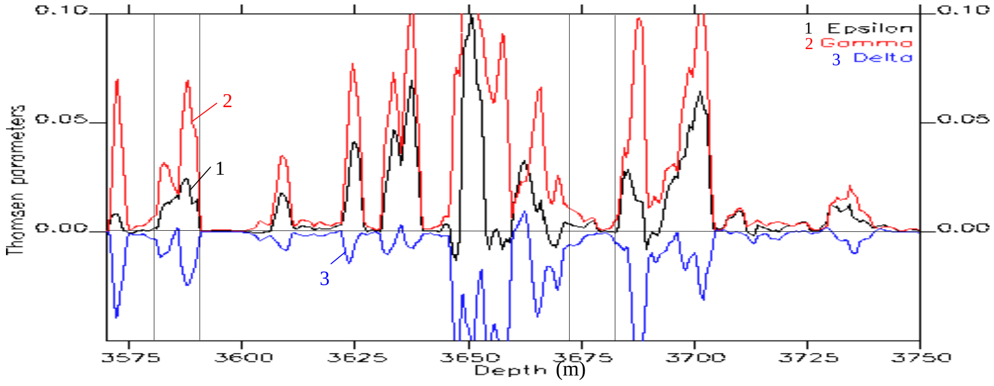

b) Thomsen parameters

Figure 3.12: Backus smoothing with 5 m averaging window.

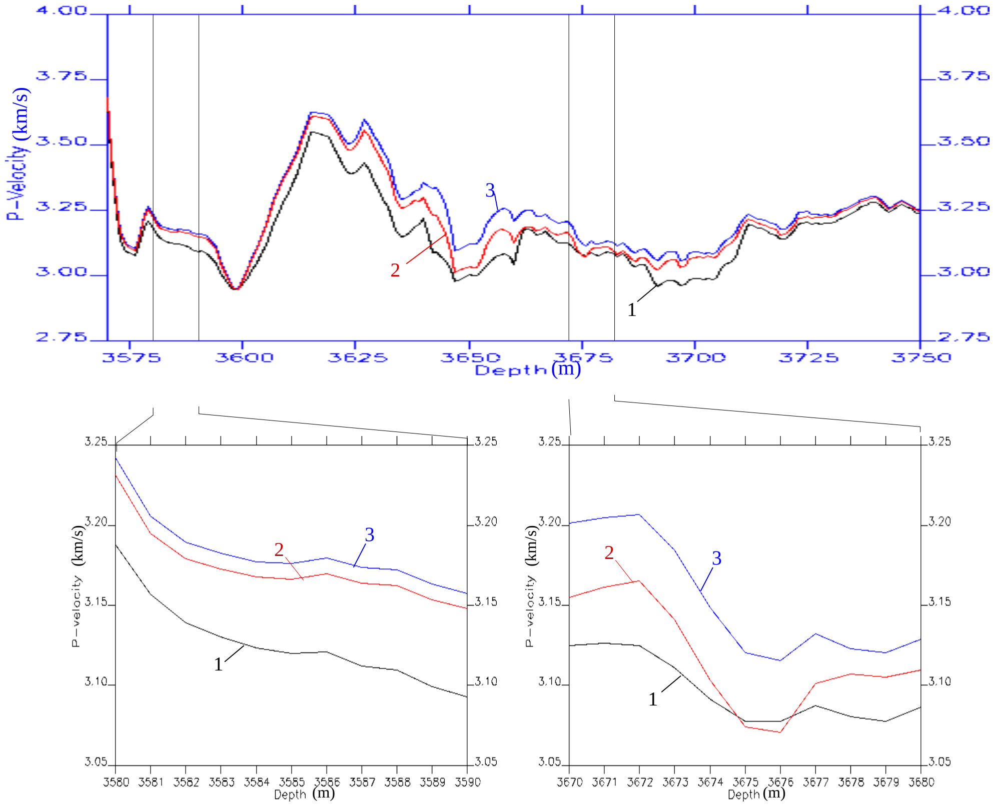

a)

1) Vertical P-velocity (Backus 20 m)
2) Horizontal P-velocity (Backus 20 m)
3) P-velocity from Voigt smoothing (20 m)

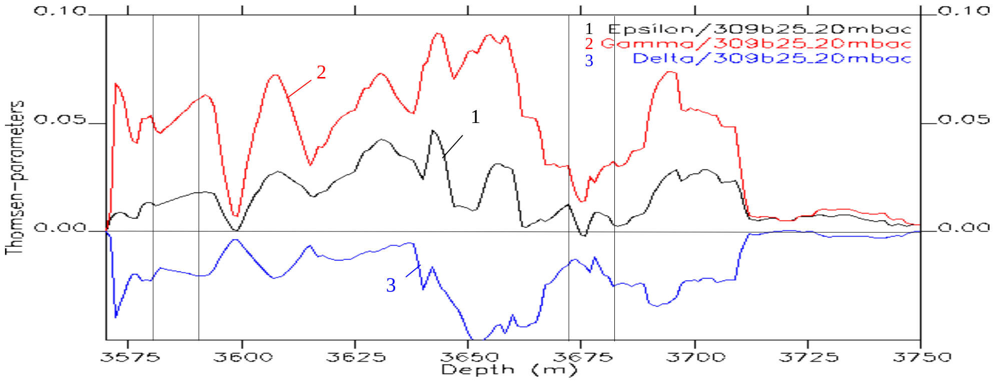

b) Thomsen parameters

Figure 3.13: Smoothing over 20 m averaging window

In the upscaled data, the horizontal velocities seem to have an upper bound by the Voigt average. In some intervals, *e.g.* the upper 50 meters of the 20 m smoothed data, the horizontal velocity is close, sometimes almost equal, to the velocity obtained from Voigt averaging. It never seems to exceed the Voigt average, though. Regarding a lower bound, at first glance the vertical velocity seems to be less than the horizontal velocity in the entire interval. However, from a closer inspection of the velocity plot of the 20 m smoothed data, I observe that the horizontal P-velocity is actually lower than the vertical velocity at the depth of 3675 m. For the corresponding Thomsen parameters it is seen that the epsilon value is negative for this specific depth value. Similar occurrences of negative values are found for epsilon values for the 5 m Backus averaged medium. The occurrence of negative ε values imply that the P-velocity normal to the symmetry axis of the Backus averaged medium is less than the P-velocity parallel to the axis. This again means that a wave propagates faster perpendicular to the layering of a thin-layered medium than along this layering. I find this fact quite remarkable, but I have not looked into possible explanations to this phenomenon in this thesis. From this observation I conclude, though, that velocities found by Reuss averaging of a small scale isotropic medium are not necessarily the absolute lower bounds for the seismic velocities in the upscaled medium for all directions of wave propagation.

While the epsilon and gamma parameters from the 5 and 20 m smoothing operations are generally positive, the delta parameter is generally negative. As stated in chapter 2, this delta parameter is decisive regarding the shape of the wavefront in the transverse isotropic medium and must be taken into consideration when performing *e.g.* moveout analysis of reflected waves (Thomsen, 1986).

To study the effect and validity of the Backus upscaling operations, I should have performed a long wave-length simulation in the original small scale isotropic model as well as in the 5 m and 20 m upscaled transverse isotropic models. These simulations have not yet been performed, though, and therefore represents a possibility for future work. But I have studied similar simulations on the synthetic model — the "lime-shale" model — to study the validity of Backus upscaling and the different isotropic upscaling functions when applied to a large scale homogeneous medium.

In the previous section I compared the resulting parameters from one-step and two-step smoothing operations, and I found that the two corresponded well when both steps of the two-step smoothing operation were performed in the same domain as the one-step operation. For example, the two-step Reuss smoothing over 5 and 20 m produced P-velocities very close to those from a 20 m one-step Reuss smoothing of the small scale data. Contrary I found that the Reuss upscaling of a priorly Voigt averaged dataset resulted in parameters that differed significantly from the one-step Reuss-upscaled data, and these observations pointed to the significance of having correctly measured — in specific correctly *averaged* — input data when simulating seismic processes.

In respect to this matter of input data correctness, the significance of accounting for transverse isotropy should be considered. Following the same line of thought as in the previous section, I define the intermediate scale (5 m) to be the finest scale for obtainable input data for making a model for a long wave-length seismic simulation. "Nature", the physical object to be modelled, is correspondingly defined to be identical to the small scale log data, which in this case is not directly accessible for measurements. Assuming now that Backus smoothing is the most correct upscaling, the wave propagating through the physical object will sense the 20 m one-step Backus averaged parameters of the small scale log data, *i.e.* "nature", while the simulated wavefield in the intermediate scale model will sense the Backus average of this model. Provided then that the intermediate scale data are given correctly, the modeller should be able to estimate the effective parameters of the physical object by Backus averaging the intermediate scale properties.

The best representation of the given object on the intermediate scale is believed to be the transverse isotropic properties identical to those calculated from the Backus upscaling over 5 m. While the resolution limit prohibits the measurements of the small scale properties, it is possible to measure the intermediate scale transverse isotropic properties by measuring waves propagating in different directions (see *e.g.* the Cand. Scient thesis of Kvalheim, 1997). In traditional logging, however, only the vertical velocities are measured, providing at best the Reuss averaged properties and at worst the slowness averaged properties, depending on the applied wavelengths.

What I would like to do, is to compare the (a) one-step Backus smoothed properties of the small scale data, assumably what the physical wave senses in "nature", with both (b) the 20 m Backus smoothed parameters of the priorly 5 m Backus smoothed data, assumably what a simulated wave propagating through the correct intermediate scale model senses, and with (c) the 20 m Backus smoothed parameters of the prior 5 m Reuss averaged model, the best model if anisotropy has not been included in the intermediate scale input data. Alas, I have not implemented the algorithms to perform Backus averaging on an already transverse isotropic medium, though implementation should be straight-foreward. I hope and expect that the two-step Backus smoothing (b) will estimate the one-step smoothing (a) quite well, but this constitutes a loose end to be checked out further. Regarding the isotropic intermediate scale model, this has been Backus smoothed (c) to produce the curves plotted in figure 3.14.

Comparing the results of this latter two-step upscaling, where the anisotropy in “nature” on the intermediate “input” scale is ignored, with the one-step averaging of which results are displayed in figure 3.13, I observe that the vertical P-velocities of the two models agree. The two-step vertical velocity is only a low-pass filtered version of the one-step smoothed version. This identity follows from the fact that this velocity calculated by Backus-averaging is always equal to the Reuss average.

Regarding the anisotropy of the upscaled model, this has clearly decreased by upscaling the Reuss model instead of the transverse isotropic model. This is seen by comparing the displays of the Thomsen parameters in the two resulting models. Here the Thomsen parameters are frequently two to three times larger in the one-step 20 m Backus upscaled model than in the priorly Reuss averaged model. The effect of this is seen in the plot of the P-velocities, where the difference between the vertical and horizontal velocities is much less for the two-step Reuss-Backus smoothing case. Obviously the reason for this is that only the heterogeneities on the intermediate scale contribute to the thin-layer anisotropy in the two-step case, while in the other case all the heterogeneities contribute. As I just stated, if the 20 m Backus smoothing had also been performed on the priorly 5 m Backus smoothed data, I would find out if the effect of the low-scale heterogeneities which were smoothed out in the 5 m average model, is preserved by the intrinsic anisotropy in the intermediate scale transverse isotropic model. Alas, this question remains unanswered. The comparison between the two procedures have nevertheless pointed out that care must be taken to avoid loss of anisotropy in model simulation when there exist heterogeneities on a smaller scale than the available resolution in the input data and where these heterogeneities contribute to the long wavelength transverse isotropic effect of the physical object to be modelled.

3.3.5 Applying a dynamic smoothing window

Thus far I have used constant shape and size on the smoothing windows when upscaling specific models. The smoothing window size has been altered from one upscaling case to another, but within each model the averaging window has been static. There are good reasons, however, for applying a smoothing window where the length of this is changed as it is slid along the input well data. In this subsection I will look into two such reasons. The first is related to variations of layering geometry and the orientation of the well trajectory along the borehole, while the second is related to a varying wavelength of the simulated wave due to changing effective velocities within the model.

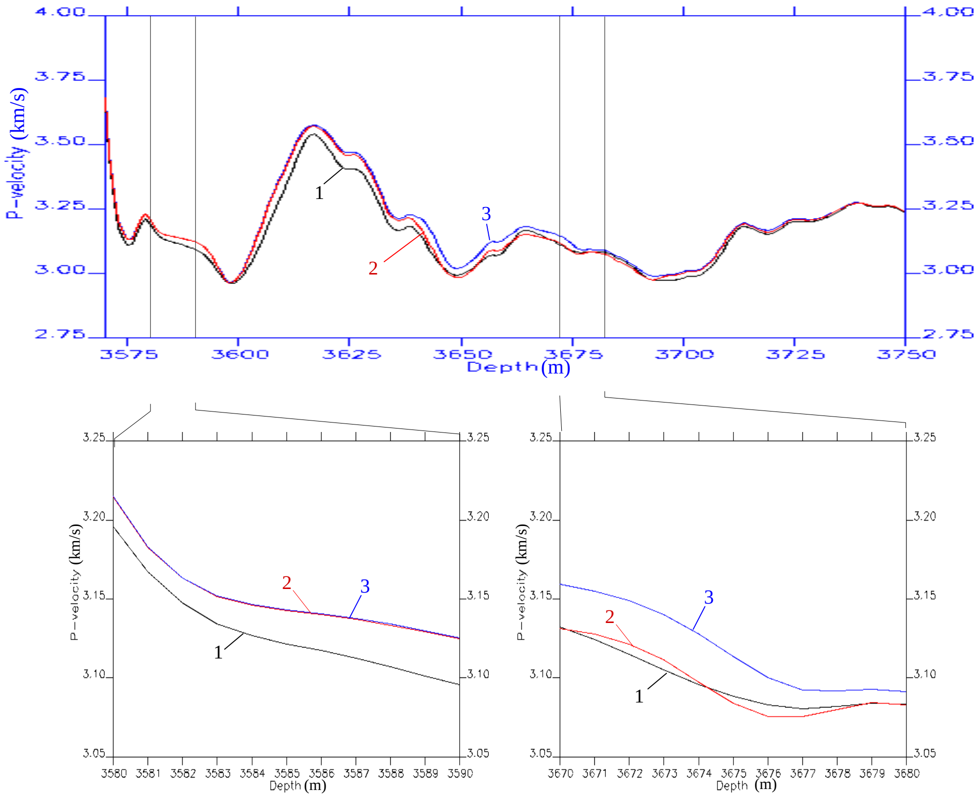

a)

1) Vertical P-velocity (Backus 20 m)
2) Horizontal P-velocity (Backus 20 m)
3) P-velocity from Voigt smoothing (20 m)

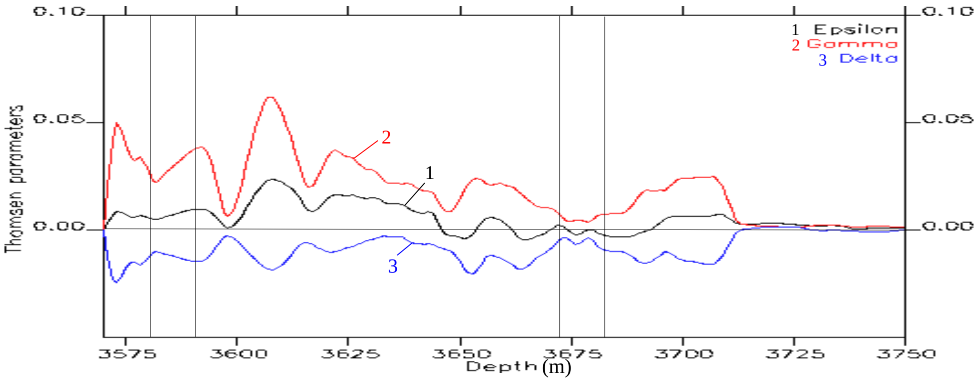

b) Thomsen parameters

Figure 3.14: The result of Backus averaging (20m) a priorly Reuss averaged (5m) well.

Orientation of layering and well trajectory

When upscaling a thin layered medium to the transverse isotropic equivalent, the orientation of the small scale layering has to be considered, since this orientation determines the orientation of the symmetry axis of the replacement medium. In most cases the studied object may be assumed to consist of horizontal layers, since the sediments often are deposited horizontally. However an oblique orientation of the small scale layers also occurs, for example in the form of crossbedding, and in the next section I will look at examples of simulated wavefields through thin-layered models with horizontal and dipping layers and their transverse isotropic equivalents.

When studying the effect of Backus averaging, the small scale models are only allowed to vary in the direction normal to the layering. In this upscaling study we are thus operating on a 1.5 dimensional model. In each layer, *i.e.* along the layering, the model is constant. When we thus are studying the effect of smoothing this model with different smoothing lengths, the lengths at issue are those perpendicular to the given layering, a layering which may be given *e.g.* from dipmeter logs.

Figure 3.15 displays the relationship between the smoothing length A' along the borehole and the smoothing length A normal to the layering when the layering is dipping with an angle θ and the borehole has a deviation η from the vertical line. To average the medium over a smoothing length A normal to the layering, the well data has to be smoothed over the length $A' = A/\cos\theta$ when the well trajectory is vertical, while the required smoothing length is increased to $A' = A/\cos(\theta + \eta)$ for the deviated case, where the two angles corresponds to rotations of the layering and trajectory in opposite directions (see the figure).

In cases where the orientation of the layering and trajectory vary along the borehole, the required averaging length for maintaining a constant averaging length normal to the layering becomes a function of depth. Assuming that the angles are nearly constant within the window range, the dynamic window applied for a given depth value is given by

$$A'(z) = A/\cos(\theta(z) + \eta(z)). \tag{3.29}$$

Wavelength variations

The validity of the performed Backus smoothing upscaling is dependent on the wave length of the applied wave in the simulation. According to Backus (1962), the upscaling model is only valid for seismic waves where:

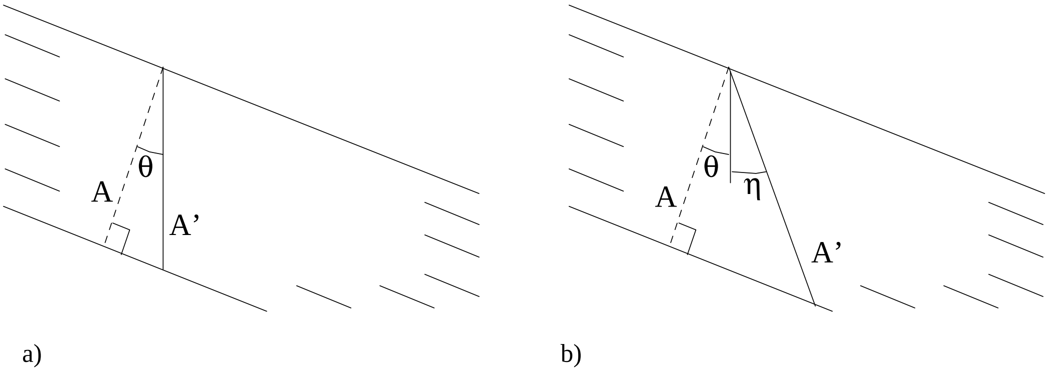

Figure 3.15: The relationship between averaging length A' along borehole and perpendicular to the layering, A, for dipping layers and a) vertical borehole and b) deviating borehole.

> "the distance κ^{-1}, over which the displacements change by an appreciable fraction of their values, is much larger than l' [*i.e.* the averaging length]".

This follows from the assumption that an equal stress is subjected to the top and bottom of the material involved in the averaging, which requires a long wavelength. In cases where an effective velocity of the material varies with depth, the wavelength λ of the propagating wave will vary accordingly, as λ and velocity are proportional. In a simulation the frequency of the propagating wave is assumed to be constant, and varying the smoothing length with depth as a function of the corresponding P-velocity will thus provide an upscaled model that is valid for all depths regardless of velocity variations for frequencies up to a certain maximum.

This upscaling by using a window proportional to the wavelength has been discussed by Sams and Williamson (1994), stating that the use of such windows gives a good overall fit between upscaled log data and long scale seismic data compared to the use of static windows. Finding the correct effective velocities, the corresponding λ and thus the correct smoothing length A — A is here equal to l' in the citation from Backus' article above — for aquiring a constant λ/A-ratio smoothing of the data over the entire depth range, involves repeating the smoothing operation several times. In one way this operation may be considered to be iterative, because the output P-velocity of one smoothing operation is used to estimate the smoothing length applied in the following smoothing operation. The data set to be smoothed is however identical for all operations, so in this respect the process is not iterative.

The procedure of the repeated process is explained below, referring to figure 3.16 where parameters from the operations on the given well data are plotted.

The goal of the repeated process is to smooth the data so that the input data at depth z_0 is averaged over a smoothing length A_0 and the smoothing window length A at other depths z is adjusted according to the relationship between the effective P-velocities at z_0 and z. According to these specifications, the smoothing length A at depth z is given by

$$A(z) = A_0 \cdot V_P(z) / V_P(z_0). \tag{3.30}$$

Initially the effective velocity is unknown. In the first calculation of the effective parameters, I therefore let the smoothing length be equal to A_0 for the entire range, *i.e.*

$$A_1(z) = A_0. \tag{3.31}$$

The use of this static smoothing window gives the first estimation $V_{P,1}(z)$ of the effective P-velocity as one of its output parameters.

The second smoothing uses the averaging window size calculated from $V_{P,1}$ by

$$A_2(z) = A_0 \cdot V_{P,1}(z) / V_{P,1}(z_0) \tag{3.32}$$

to calculate the second estimation of the effective P-velocity $V_{P,2}(z)$.

In each repetition of the smoothing, the calculated P-velocity is slightly modified, but the modification between consecutive steps is assumed to decrease with the number of repetitions. Thus, the effective velocities and the other effective parameters will converge, *i.e.* $V_{P,(N+1)}(z) \simeq V_{P,N}(z)$.

This is illustrated in the current figure. Here A_0 is 20 m and $z_0 = 3580$ m. The effective P-velocity from the two first estimations are displayed in panel a), the corresponding Thomsen parameters in panel b) and the applied smoothing lengths in panel c). For displaying the convergence of the parameters, curves d) and e) show additional numbers of output P-velocity and applied smoothing window lengths for a 20 m segment of the depth range.

From panels a) and c) it is seen that the curve of $V_{P,1}$ and A_2 have the same shape. This follows from that $A_N = k \cdot V_{P,(N-1)}$. A_2 also fullfills the length requirement at 3580 m. To explain the change in the effective velocity from the first to the second estimation *e.g.* at depth $z_1 = 3620$ m, it can be seen in panel a) that the effective velocity $V_{P,1}$ is higher at depth z_1 than at depth z_0, and, accordingly, A_2 is longer than A_1 at z_1. In fact A_2 is approximately 2 m longer than A_1 at z_1. When the effective velocity in the following run is reestimated at this location by using A_2, the parameter

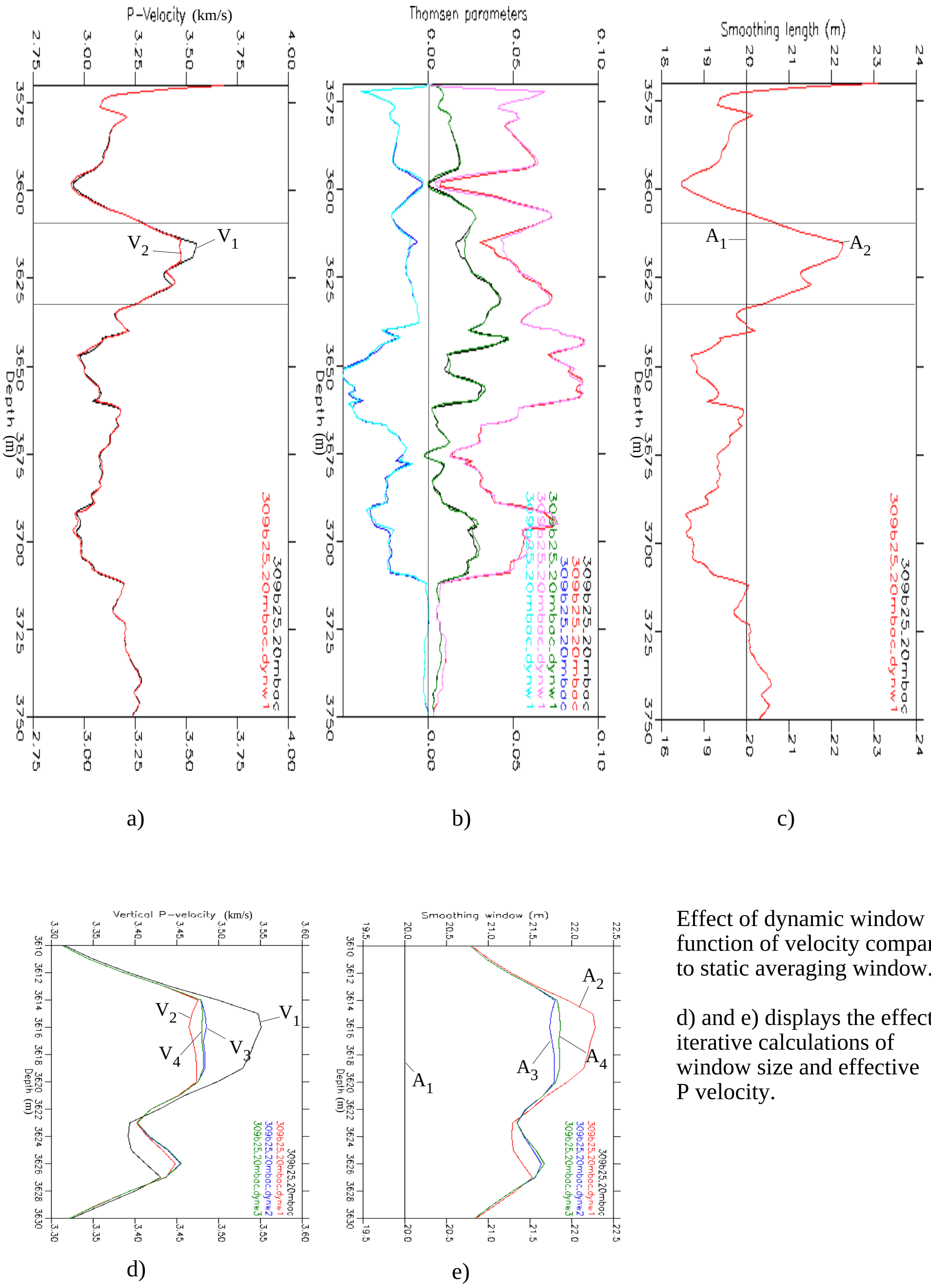

a)

b)

c)

d)

e)

Effect of dynamic window as function of velocity compared to static averaging window.

d) and e) displays the effect of iterative calculations of window size and effective P velocity.

Figure 3.16: The effect of applying a dynamic smoothing window as a function of effective velocities.

values in a 1 m segment on each side of the interval included in the first averaging, where A_1 was used, is added to the volume that is averaged. In this case, the average of these outermost samples is smaller than the average within the A_1 window, and therefore the average velocity of the small scale data within A_2 is less than that within A_1. Accordingly, $V_{P,2}$ is smaller than $V_{P,1}$ at z_1.

To understand the further convergence observed in panels d) and e); since $V_{P,2}$ is less than $V_{P,1}$ at z_1, A_3 becomes smaller than A_2. The average velocity at z_1 is however still greater than that found at z_0, so A_3 is larger than A_1. Since the trend of the P-velocity values is decreasing in the directions away from z_1 in the intervals within the window of length A_2 but outside that of length A_1, both windows positioned with their centre at z_1, decreasing the smoothing window from A_2 to A_3 leads to an increased average velocity. The value of $V_{P,3}$ is thus within the range limited by $V_{P,1}$ and $V_{P,2}$ at z_1. This observations is a general feature of the curves belonging to the four estimations displayed in panels d) and e). The averaging length and the resulting P-velocity associated to one estimation is enclosed by the parameter values of the two previous. Also, the difference between the values for consecutive estimations decreases. The data will therefore converge.

The difference between the estimated P-velocity at z_1 between the first estimation and the value of convergence is seen on the figure to be approximately 0.05 km/s, which may be quite significant in a wave simulation case. Therefore the use of a dynamic averaging window should be considered when operating on data having large velocity gradients on large scale.

A final remark regarding dynamic smoothing length: In the discussion above we have only considered the P-velocity values. Thus the smoothing window length was adjusted as a linear function of the large scale variations in this velocity. However, for the propagating S-wave, the appropriate smoothing length is less than that for the P-wave, since the S-wave has a lower velocity. It would therefore be nice to be able to make an upscaled model where properties determining the behaviour of the S-waves are smoothed over a shorter distance than those determining the P-wave. Unfortunately, in this respect, in a transverse isotropic medium the velocities of the P-wave and the SV-wave both depend on the Thomsen parameters epsilon and delta as well as the vertical P-velocity (Thomsen, 1984). Thus, to separate the parameter sets for the two waves is not possible. Instead, if the synthetic S-wave data is to be utilized, the applied smoothing length should be selected short enough so that the wavelength of the S-wave is also considerably longer than the applied smoothing length.

3.4 Effects of smoothing and upscaling on wave propagation

Thus far in this chapter the upscaling has been discussed by pointing to differenes in the upscaled parameters caused by different smoothing methods. However, as I have mentioned previously, the validity of the different models should be tested by simulating wave propagation in the different upscaled model versions and comparing seismograms and wave-field snapshots from these simulations with corresponding output from simulations in the original small scale model.

The remaining part of this chapter contains descriptions and discussions of the results from such simulations on a small scale bipartite model consisting of 10 m thin parallel layers of high and low impedance media, the "lime-shale" model presented in section 3.3.3, and the various upscaled versions of this model.

Two versions of the model are used, one with a horizontal layering and the other with a 10 degrees dip. The thin layered and the upscaled replacement media are all subjected to simulations with two different wavelet frequencies to check the validity of the different upscaled media for different ratios of wavelength to layer thickness. Simulating waves in the dipping layers model will here give an indication of the significance of accounting for the dipping layers by comparing the wavefields from the small scale models and the corresponding transverse isotropic upscaled models.

For performing the simulations, the simulation program Seismod is used, developed at the University of Bergen by a cooperation project between Institute of Solid Earth Physics and Department of Informatics. This program is a finite difference implementation of the elastic wave equation and provides means for simulating waves through gridded isotropic and transverse isotropic media with constant or varying symmetry axes (Haveraaen et al., 1999).

A 1-D representation of the thin layered medium and its corresponding versions of upscaled isotropic media used in the following simulations was displayed in figure 3.9 in section 3.3.3. To produce a 2-D horizontally layered small scale material, the properties from this synthetic data are extrapolated horizontally, and correspondingly the dipping layer material is produced by extrapolating the properties according to a dipping correlation line.

The 2-D property and survey geometries are given in figures 3.17 and 3.18. As seen here, the models are the composite of three large scale slabs. At the top there is a 150 m thick overburden, representing the elastic properties of water, followed by a 200 m thick horizontal slab of one of the two thin-layered

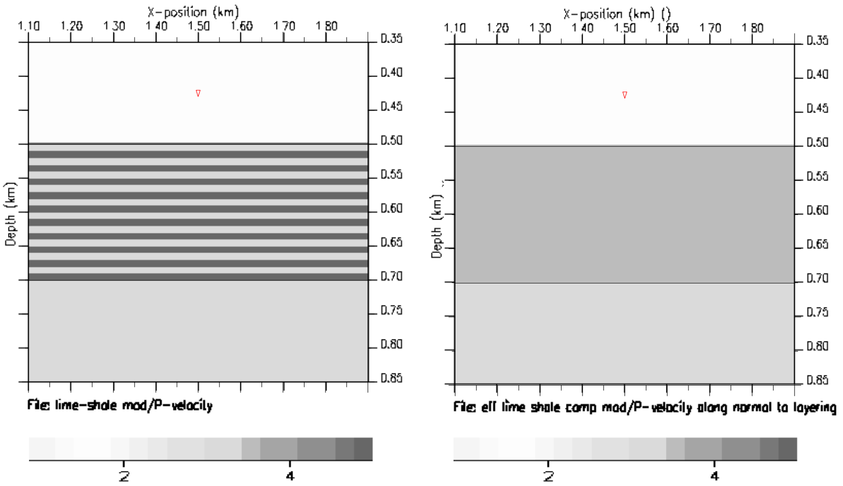

Shotposition: x = 0.5 km
z = 0.425 km

Geophones: x = 1.15 + (i-1) x 0.0125km (i = 1, 2,.., 57)

Properties		Original medium	TI replacement medium
Top layer:		P-velocity: 1.5 km/s S-velocity: 0.0 km/s Density: 1.0 g/ccm	
Middle layer:	Thin layer 1: (10 m thick)	P-velocity: 5.0 km/s S-velocity: 3.0 km/s Density: 2.6 g/ccm	Vert. P-velocity: 3.637 km/s Vert. S-velocity: 1.900 km/s Density: 2.55 g/ccm Epsilon: 0.142 Delta: -0.0624 Gamma: 0.284 Inclination: 0.0 deg
	Thin layer 2: (10 m thick)	P-velocity: 3.0 km/s S-velocity: 1.5 km/s Density: 2.5 g/ccm	
Bottom layer:		P-velocity: 3.2 km/s S-velocity: 1.85 km/s Density: 2.3 g/ccm	

Figure 3.17: Horizontally thin-layered "lime-shale" model and its Backus averaged replacement model.

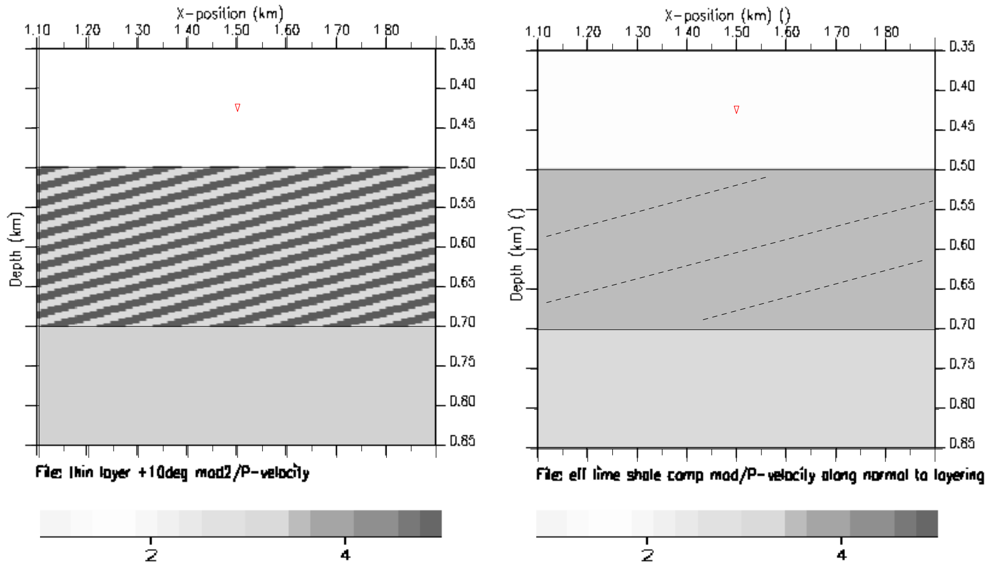

Shotposition: x = 0.5 km
z = 0.425 km

Geophones: x = 1.15 + (i-1) x 0.0125km (i = 1, 2,.., 57)

Properties		Original medium	TI replacement medium
Top layer:		P-velocity: 1.5 km/s S-velocity: 0.0 km/s Density: 1.0 g/ccm	
Middle layer:	Thin layer 1:	P-velocity: 5.0 km/s S-velocity: 3.0 km/s Density: 2.6 g/ccm	Vert. P-velocity: 3.637 km/s Vert. S-velocity: 1.900 km/s Density: 2.55 g/ccm Epsilon: 0.142 Delta: - 0.0624 Gamma: 0.284
	Thin layer 2:	P-velocity: 3.0 km/s S-velocity: 1.5 km/s Density: 2.5 g/ccm	
		Periodic layering, each of 10 m vertical thickness. Inclination: 10 deg	Inclination: 10 deg
Bottom layer:		P-velocity: 3.2 km/s S-velocity: 1.85 km/s Density: 2.3 g/ccm	

Generation of effective medium: Assumed same effective medium as in horizontal case, except for the inclination angle, which is set to 10 degrees, equal to the layer dip of the original medium.

Original medium has layers of slightly different values at gridpoints due to interpolation and discretation.

Figure 3.18: Spatial thin-layered model with layers dipping 10 degrees to the left and its transverse isotropic replacement medium.

media or one of their large scale replacements, and at the bottom there is a 150 m thick homogeneous medium. The model is 800 m wide and 500 m deep, with x-values ranging from 1.1 km to 1.9 km and depth values from 0.35 km to 0.85 km. The upper edge of the model behaves like a free surface in the simulations, reflecting all the energy, and the z-coordinate of 0.35 km may thus be considered to represent the sea surface. The other edges of the model are energy absorbing. The grid size is 2.5 m × 2.5 m. Each property grid of the property model thus consists of 64 501 grid nodes.

The simulated survey setup is given by the position of the seismic source and receivers. The source is placed in the middle of the upper layer representing the water layer, while 57 receivers are placed along a horizontal line at depth 0.75 km in the lower medium, symmetric about the vertical line through the source, and with a 12.5 m distance between adjacent receivers.

The waves to be studied are the directly transmitted P-waves, and to limited degree the directly transmitted S-wave. The reason for focusing on P-wave is that S-waves are not generated in the water layer, and P-waves are only converted to S-waves at the interface at 0.5 km depth for obliquely incidenting waves. Thus, the wavefront for the S-wave in the vertical direction vanishes. The P-wave, on the other hand, gives a good picture of the effective velocities in the medium for all directions of propagation. The waves are studied both by the use of snapshots of the wavefields taken during the simulation, describing the absolute particle displacement in the entire spatial model at specific time intervals, and by the use of seismograms recorded at the positioned receivers. The snapshots will be useful for comparing the wavefields from different media variations. The snapshots can be contoured and plotted together in the same figure. In this way the effective velocities in the different media subjected to the simulation can be compared by simply comparing the contoured wavefronts.

In real life the means for surveying the wavefield is by recording seismograms at a limited number of geophone or hydrophone locations. The plotting of the aquired seismograms does not give such an intuitive picture of the wavefield as the snapshots, however. For example, it is difficult to identify the different events in the traces, in terms of being reflected or refracted, P- or S-wave, and to get the picture of the "travel-history" of the waves. However, from the seismograms the arrival times of the different waves can easily — in theory — be picked, providing a simple test of the correspondence between the small scale medium and its different upscaled versions. In specific the seismograms will be used to study the difference in the effective medium properties from applying different seismic frequencies, although, as will become evident as going along, to compare the output data from applying different frequencies is not straightforward.

The applied wavelets are Ricker zero phase wavelets of 30 Hz and 100 Hz. Marion et al. (1994) identified the transition from ray to effective medium behaviour of a stratified medium, corresponding to the Backus- and slowness averaged media, to occur at the λ/d-ratio of approximately 10, where λ is the length of the propagating wave and d is layer thickness. Since the effective P-velocity for this model is in the range of 3.6 km/s and 3.8 km/s for the thin-layered intermediate slab, λ becomes longer than 100 m when applying the 30 Hz wave, while the application of a 100 Hz wavelet produces a wavelength of about $30-40$ m. The λ/d-ratio in the former case is thus greater than 10 and in the range of $3-4$ in the latter case. The next section, considering data from the horizontally layered model, verifies that such a transition actually exists for the given 10 m layered model for some frequency between the 30 Hz and 100 Hz.

3.4.1 Horizontal layers

30 Hz wavelet

The snapshot-analysis This section contains a description and discussion of the snapshots from the simulations applying the 30 Hz Ricker zero phase wavelet in the small scale horizontally layered and the upscaled model versions, cf. figure 3.17.

The displayed snapshots are taken 125 ms after the shot, each consisting of a grey-scale displacement amplitude map and a selected number of contours. The contours are provided to lineate the wavefronts for comparison purposes. Being simulated measurements using wavelets with normalized amplitudes and considering only the differences in the wavefront positions in the snapshot, the unit of the mapped displacement has not been considered. The maximum amplitude is identical in all the snapshots, found in the direct P-wave propagating laterally in the water layer. The amplitude value here is 3.83 units. Contours are plotted for amplitude values of 0.02 , 0.25 and 0.5 units. The two latter contours are helpful when comparing the position of the main energy in the different snapshots, while the 0.02 unit contour is used to locate the head of the wavefront, plotting the locations where the displacement has reached approximately 0.5 % of the maximum amplitude.

The snapshot from the original thin-layered model is plotted in figure 3.19 a), along with two reference curves which will be commented later. The major features seen in this snapshot are also found in the snapshots from the replacement media and are therefore briefly described here. At the capture moment, much energy has been reflected from the free surface at the top of the model and from the bottom of the water layer at 0.5 km. The water layer also contains a refracted P-wave due to the higher P-velocities in the underlying composite layer. Thus most of the released energy remains as P-waves in the upper layer, cf. the location of maximum amplitude in the snapshots.

At the interface at 0.5 km much energy from the incident P-wave is converted to S-waves for oblique incidenting waves. The S-waves thus contains the largest amplitudes in the intermediate layer, although due to the larger geometrical spreading of the corresponding P-wave, the energy relationship between the two modes is not straightforwardly given. It is also noted that in the vertical direction the S-wave vanishes and the amplitude of the P-wave increases accordingly.

The most specific feature of the snapshot from the thin-layered model is the occurence of ripples in the head of the P-wave front in the intermediate layer. Obviously these ripples are caused by the internal layers of high and low velocities. These ripples are small, however, only causing minor differences from an entirely smooth wavefront. There are neither observed any reflections from the internal layering. Thus, on the scale of the propagating wave the composite material may be considered to be homogeneous. My goal is then to find which of the homogeneous upscaled version that accounts the best for the behaviour of the small scale heterogeneous medium for this frequency. Therefore, the snapshot from the small scale model is now compared with the snapshots from the Reuss-, Voigt-, slowness- and velocity averaged models, and finally with the transverse isotropic Backus averaged model.

The end-members of the presented isotropic versions are the Reuss and Voigt averages. The corresponding snapshots are plotted in figure 3.19 b) and 3.20 a). The black contours here are those corresponding to the amplitude maps of the upscaled models, while the red contours are overlayed from the small scale model snapshot for comparison purpose. For this purpose the head of the P-wave wavefronts, the outermost contour, in the Reuss and Voigt snapshots has also been plotted in the small scale medium snapshot, given as dashed lines marked with circles and triangles respectively. Comparing the snapshots of these three models, I observe that the vertical going P-wave in the Reuss replacement medium fits almost exactly with the P-wave in the thin-layered model. For the horizontally propagating P-wave, the Voigt averaged model clearly gives the best fit, though the correspondence here is not as good as the fit between the thin-layered model and the Reuss averaged medium for the vertical wave. Clearly the thin-layered medium behaves as an anisotropic medium for the applied wavelength scale. Regarding the S-waves in the large scale intermediate layer, the effective S-velocity in the small scale model appear to be somewhere between the Reuss and Voigt average.

The P- and S-velocities in the slowness- and velocity averaged models

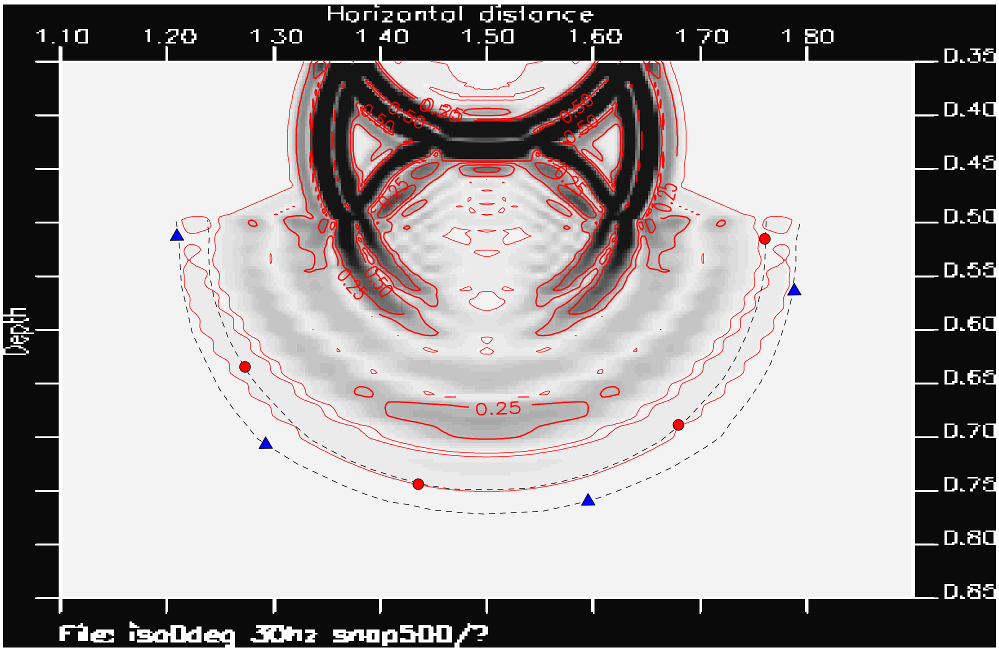

a) Thinlayered model

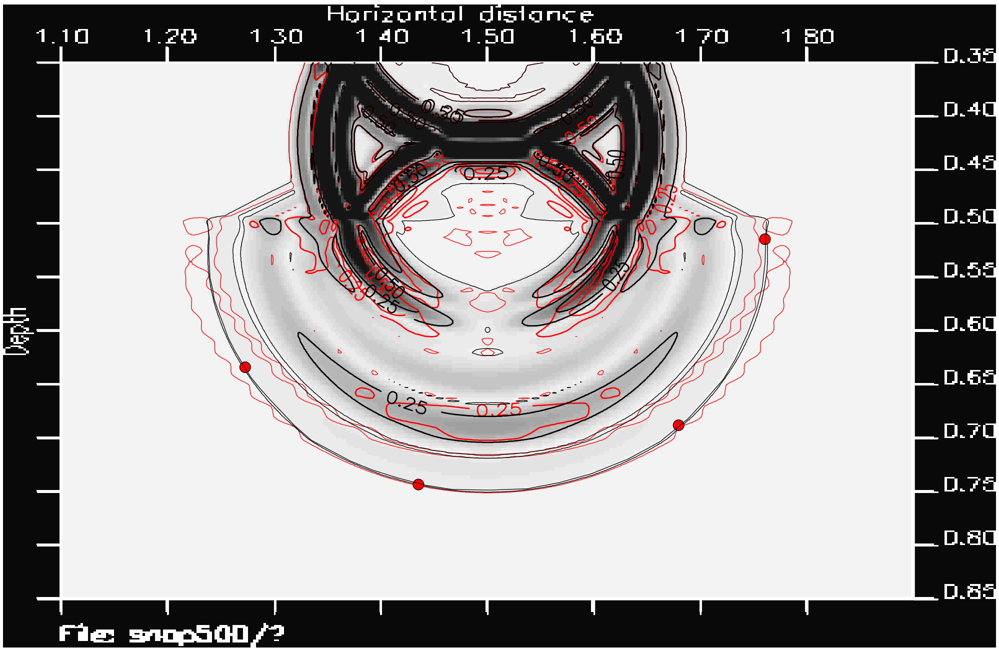

b) Reuss replacement medium

– – –●– – Reuss isotropic wavefront

– – –▲– – Voigt isotropic wavefront

Figure 3.19: Snapshots from thin-layered model and Reuss averaged replacement model, using a 30 Hz wavelet.

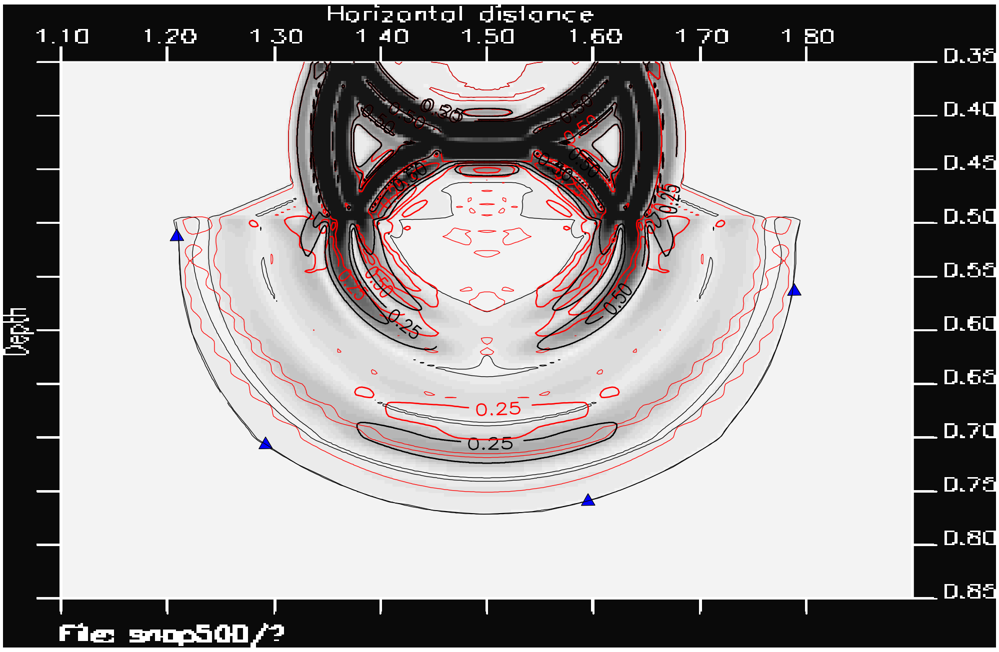

a) Voigt replacement medium

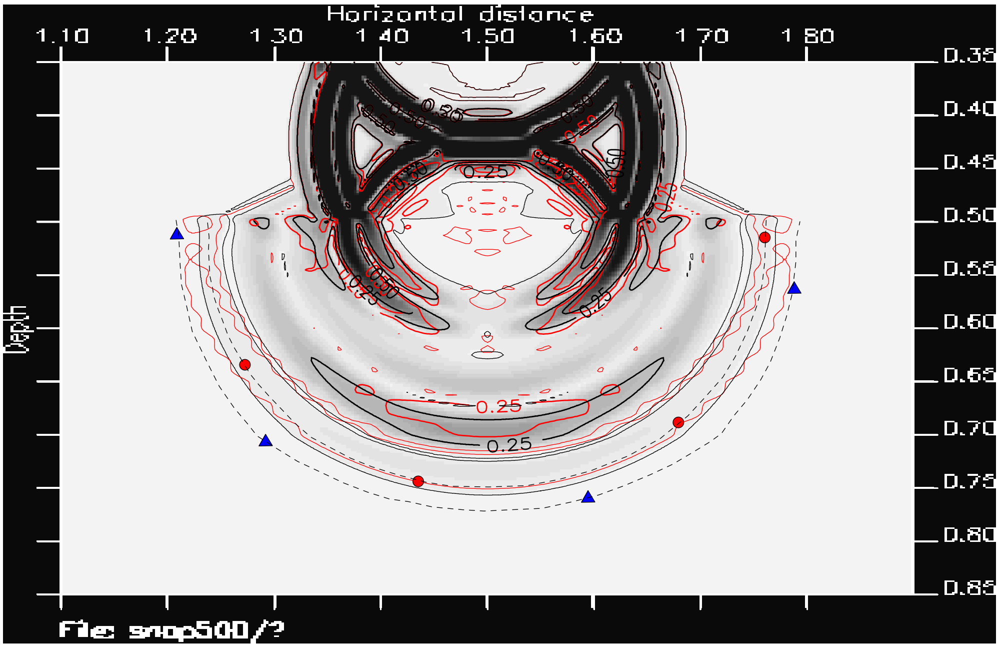

b) Average slowness

Figure 3.20: Snapshot from a) Voigt-averaged and b) slowness-averaged models, using a 30 Hz wavelet.

are enclosed in the range given by the Reuss and Voigt models, and the corresponding snapshots from these are plotted in figures 3.20 b) and 3.21 a). Also here the small scale model contours are plotted in red and the enclosing Reuss- and Voigt wave-front heads are plotted. For the average slowness wavefield the vertically propagating P-wave is ahead of the wave in the small scale model, while for horizontally propagating P-waves, the velocity is too small. Regarding the S-waves, the waves in the slowness averaged model fit better with those of the small scale model than either the Reuss or Voigt model. For the velocity averaged model, the head of the P-wave has almost propagated as far as that of the Voigt averaged model. This model thus gives a poor estimate of the vertical waves. For the horizontal waves at the top of the intermediate model, the average velocity model gives an almost exact reproduction of the P-waves in the small scale model, *i.e.* a better reproduction than any of the other upscaled media. As an effect of this, the critically refracted P-wave in the water layer is also better reproduced by this model than by any of the others. Regarding the S-waves in the velocity averaged model, these are slighly ahead of those in the small scale model. Thus the slowness averaged model turns out to be the one reproducing the S-waves in the small scale model the best.

The properties of the transverse isotropic replacement medium calculated by Backus smoothing are given in the table in figure 3.17. The vertical P- and S-velocities in the intermediate layer are here equal to those of the Reuss model, and the horizontal P-velocity, given by $V_{P,90} = V_{P,0}\,(1+\varepsilon)$, is approximately 4.15 km/s, slightly higher than the velocity of the Voigt averaged isotropic medium. Observing the snapshot from the simulation in the Backus averaged model, in figure 3.21 b), comparing the contours of the transmitted P-wave with the red contours overlayed from the thin-layered model, it is seen that there is a very good correspondence for the vertically propagating wave as well as for obliquely travelling waves. Compared to the isotropic models, the Backus averaged model is thus by far the best model. The only exception to this superiority regards the P-wave propagating in the horizontal direction in the very upper part of the intermediate layer, corresponding to the critically refracted wave. Here the velocity averaged model accounts the best for the wave field in the small scale model. From the observation of the snapshots at the time of 125 ms, the P-wave critically refracted back to the upper layer is thus modelled the best by using the average velocity model for the thin-layered section. Regarding the S-wave generated at the interface below the upper water layer, the snapshots display a better correspondence between the S-waves in the small scale medium and in the slowness averaged isotropic replacement medium than the correspondence between the thin-layered medium and the transverse isotropic Backus

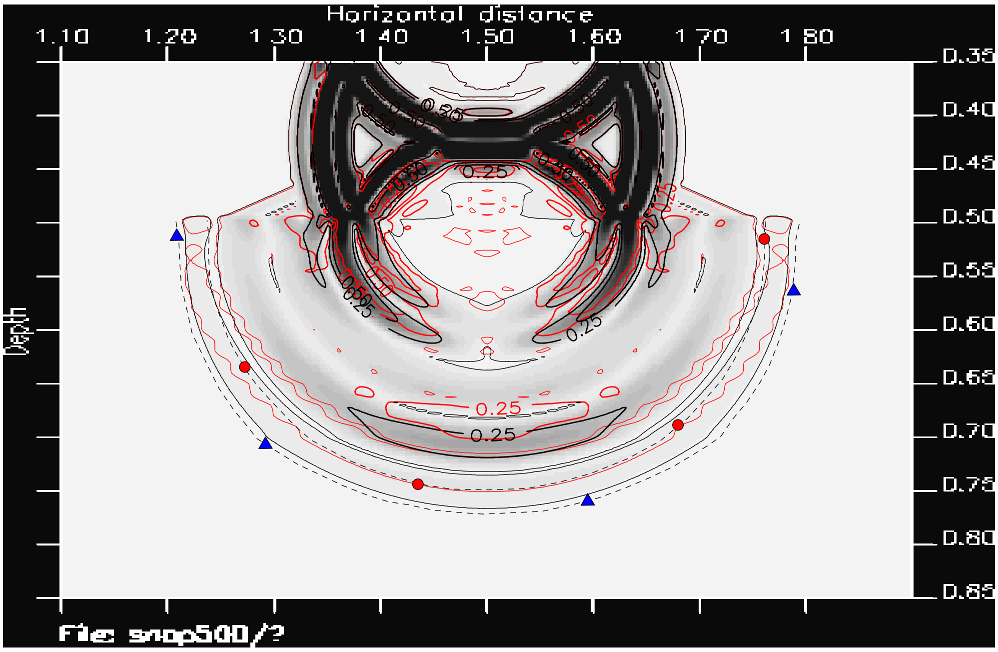

a) Average velocity

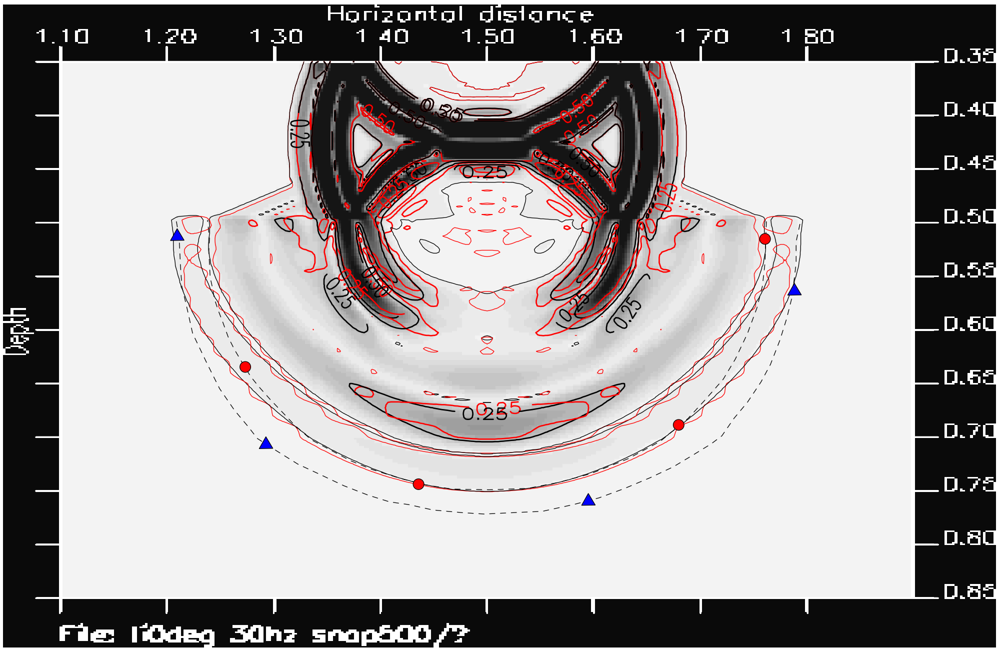

b) Transverse isotropic model

– – ● – – Reuss isotropic wavefront

– – ▲ – – Voigt isotropic wavefront

Figure 3.21: Snapshots from a) velocity averaged and b) Backus averaged "lime-shale"-model, using a 30 Hz wavelet.

averaged medium.

These observations can be explained by referring to the λ/d-ratio for the thin-layered model. For the P-waves, this ratio is greater than 10 for the given frequency, and thus the medium behaves as a transverse isotropic effective medium. Regarding the difference between the effective P-velocity in the small scale medium and the Backus averaged medium for horizontally propagating waves, this can probably be attributed to influence by the overlying lower velocity water layer at these locations. For a more thorough study of the validity of the Backus averaging for the waves travelling in the direction of the layering, I would suggest to "rotate" the internal layering of the intermediate layer by 90 degrees. The upscaled replacement media would be identical, except for the orientation of the symmetry axis of the transverse isotropic medium, which would be correspondingly rotated. Comparing the vertically propagating waves in the small and large scale models for such a case, I would still expect the best correspondence for the Backus averaged medium. This has however not been tested, yet.

Regarding the S-wave, the wavelength of this wave in the thin-layered medium is approximately 60 m for the 30 Hz wave. Thus the λ/d-ratio is approximately 6, which is in the transition zone between the short and long wavelength to layer thickness limit. According to Marion et al. (1994), this short wavelength limit is given by the average slowness medium, and this is a tenable explaination of why the S-wave of the slowness averaged version corresponds the better with the small scale model. As will be displayed shortly, by replacing the applied 30 hz wavelet with a 100 Hz wavelet, also the correct effective P-wave velocity of the thin-layered medium is given by the slowness averaged velocity due to the decreased λ/d-ratio.

The seismogram analysis While snapshots are superior for visualizing the wavefield, the domain in which real experiments are monitored is that of seismograms. Here the seismograms are used to find and compare the first break arrival times of the 30 Hz P-waves in the small scale and the various upscaled model versions. In the next subsection a similar picking of arrival times is done for the 100 Hz wave, and the effective behaviour of the thin-layered model is thus compared for the two frequencies.

Figure 3.22 displays the relative shape and length of the recordings of zero phase Ricker wavelet 30 Hz and 100 Hz wave at a receiver where the first break of the wave arrives at t_{fb}. The seismograms plotted here are constructed by convolving the wavelets with the impulse function $\delta\left(t - t_{fb}\right)$. By increasing the amplitude of the two inner seismograms 250 times and cropping off everything but the base of the resulting wiggle trace, the outermost

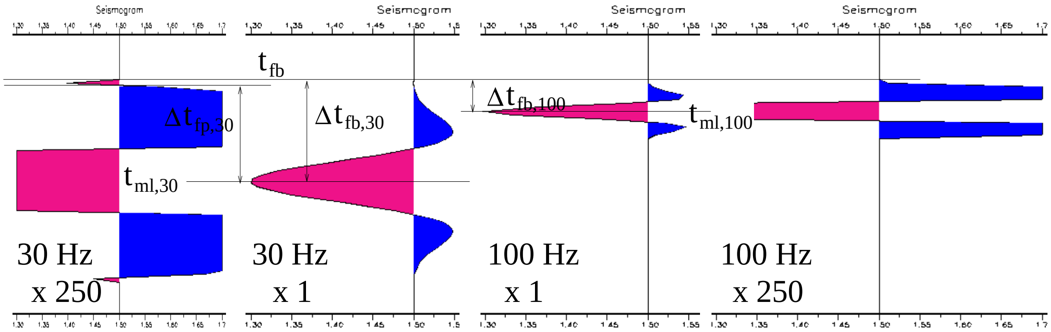

Figure 3.22: Relative shape and wavelength of a Ricker zero phase 30 Hz and 100 Hz wavelet

traces result. From the amplified traces the arrival time t_{fb} of the waves can be picked directly. If there had been noise in the seismograms, this would be more difficult, however. The easiest time-event to pick from the less amplified traces is the time of maximum amplitude in the main lobe of the wavelet, t_{ml}. If the time delay Δt_{fb} from t_{fb} to t_{ml}, *i.e.* the delay from the first non-zero value to the maximum amplitude value of the wavelet, is known, t_{fb} can be calculated from picking t_{ml}.

As seen in this figure, the 30 Hz wavelet contains a very small extra lobe compared to the 100 Hz wavelet. To study possible phase changes of the applied 30 Hz wavelet in the simulations, the time t_{fp} where the trace changes sign after this minor lobe is also considered, and the time-delay from t_{fp} to t_{ml} is denoted Δt_{fp}.

In the FD simulations the wavelets of the propagating wave is not necessarily identical with the input wavelets given in figure 3.22, due to signal distortions *e.g.* occuring in the source implementation. Thus the time delays which can be used to estimate the arrival time of the first break of the wave cannot be found directly from the input wavelets. Neither, which will become evident especially from the 100 Hz seismograms displayed in the next section, can the time-delay be easily determined from the seismograms, since energy leaks ahead of the wave due to numerical effects. The exact arrival time t_{fb} in the seismograms can thus only be estimated. In the following plots of the 30 Hz simulations, the time of the maximum amplitude t_{ml} has been picked for each trace, and the time-lines t_{fb} and t_{fp} are calculated by subtracting the time-delays $\Delta t_{fp} = 26.4$ ms and $\Delta t_{fp} = 22.7$ ms from this value. The values of the time-delays are chosen to fit the assumed waveshape, *i.e.* ignoring supposed dispersion noise, in the traces corresponding to vertically propagating waves recorded in the upscaled medium models.

The vertical displacement seismograms from the thin-layered model and the transverse isotropic model are plotted in figures 3.23 and 3.24.

The three hyperbolic time curves in these figures are those of t_{fb}, t_{fp} and t_{ml}. As can be seen in figure 3.24, the correspondence between the traces and the time-lines is very good for the transverse isotropic upscaled medium. This follows directly from the setting of Δt_{fb} and Δt_{fp}. A minor detail when observing the amplified seismograms recorded on the left side in this figure is that the first lobe in the arriving wave is slightly shorter here than for the vertically propagating waves. This difference is however insignificant. Observing the seismograms in the thin-layered model displayed in figure 3.23, however, it is seen that the wavelet here is different from the case for any of the replacement media. For the vertically propagating wave, the first minor lobe in the wavelet has a smaller amplitude than that recorded in the upscaled media. This lobe also arrives slightly ahead of the calculated t_{fb}. The second lobe in the trace also arrives ahead of the time given by the calculated t_{fp}. For the traces of the obliquely travelling wave displayed in the left window, the minor first lobe has totally vanished, and the second lobe of opposite sign constitutes the first break of the signal. This lobe arrives at time close to t_{fb}. This difference in wave-shape recorded in the thin-layered medium compared to that recorded in any of the isotropic replacement media, can be explained from figure 2.5 in chapter 2, related to the change of wave-shape as the λ/d-ratio varies from the ray-trace to the effective medium limit. For example, in this figure the composite material consisting of 128 thin layers (Model 4), has an effective velocity very close to that of the medium with 1024 layers (Model 1). The waveshapes of the two transmitted waves are however quite different. By decreasing the layer thicknesses of the small scale model, the wavelet difference between the wave measured the homogeneous replacement medium and the thin-layered medium is expected to vanish, just as the wavelet measured in figure 2.5 is similar for the end members.

Because of this different wave-shape, it may be argued that choosing the t_{fb}-curve, which has been generated on the assumption of the waveshape measured in the homogeneous medium models, does not constitute the correct arrival time for the wave propagated through the thin-layered model. I have nevertheless chosen to use this line for comparing arrival times for the seismograms from all the different models. I think this can be justified by the very small amount of energy found ahead of this time-line for the central receivers in figure 3.23. The energy here is so small that it qualifies to be estimated as numerical noise, cf. the energy found ahead of the arriving 100 Hz wave propagated through the transverse isotropic medium in figure 3.28. Indeed, for the obliquely travelling wave there is no such first lobe ahead of the t_{fb}-line.

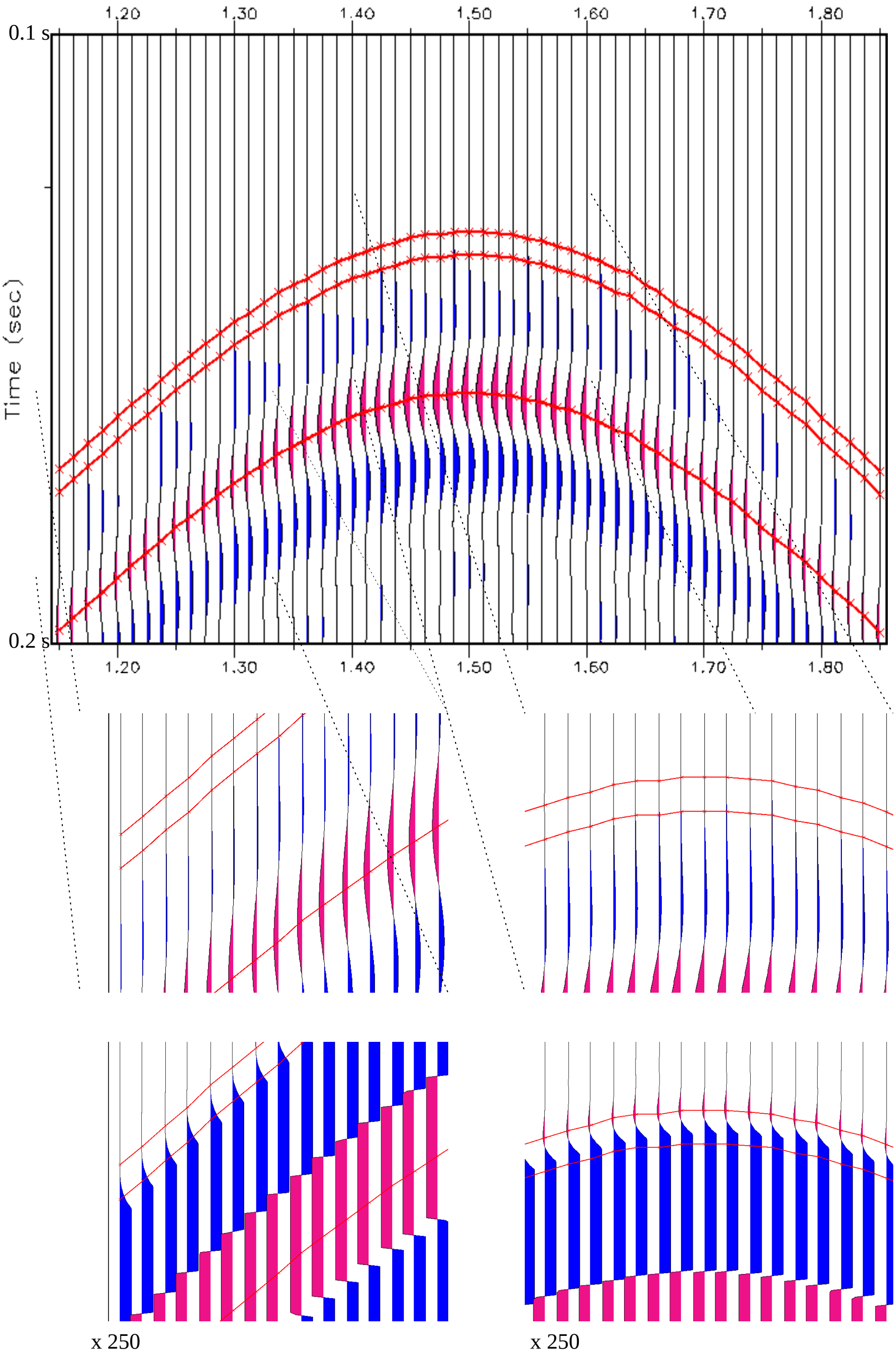

Wavelet: Ricker zero phase 30 hz
Medium: Isotropic thin-layered medium

Figure 3.23: Synthetic seismogram from a 30 Hz Ricker wavelet passing through the thin-layered “lime-shale”-model.

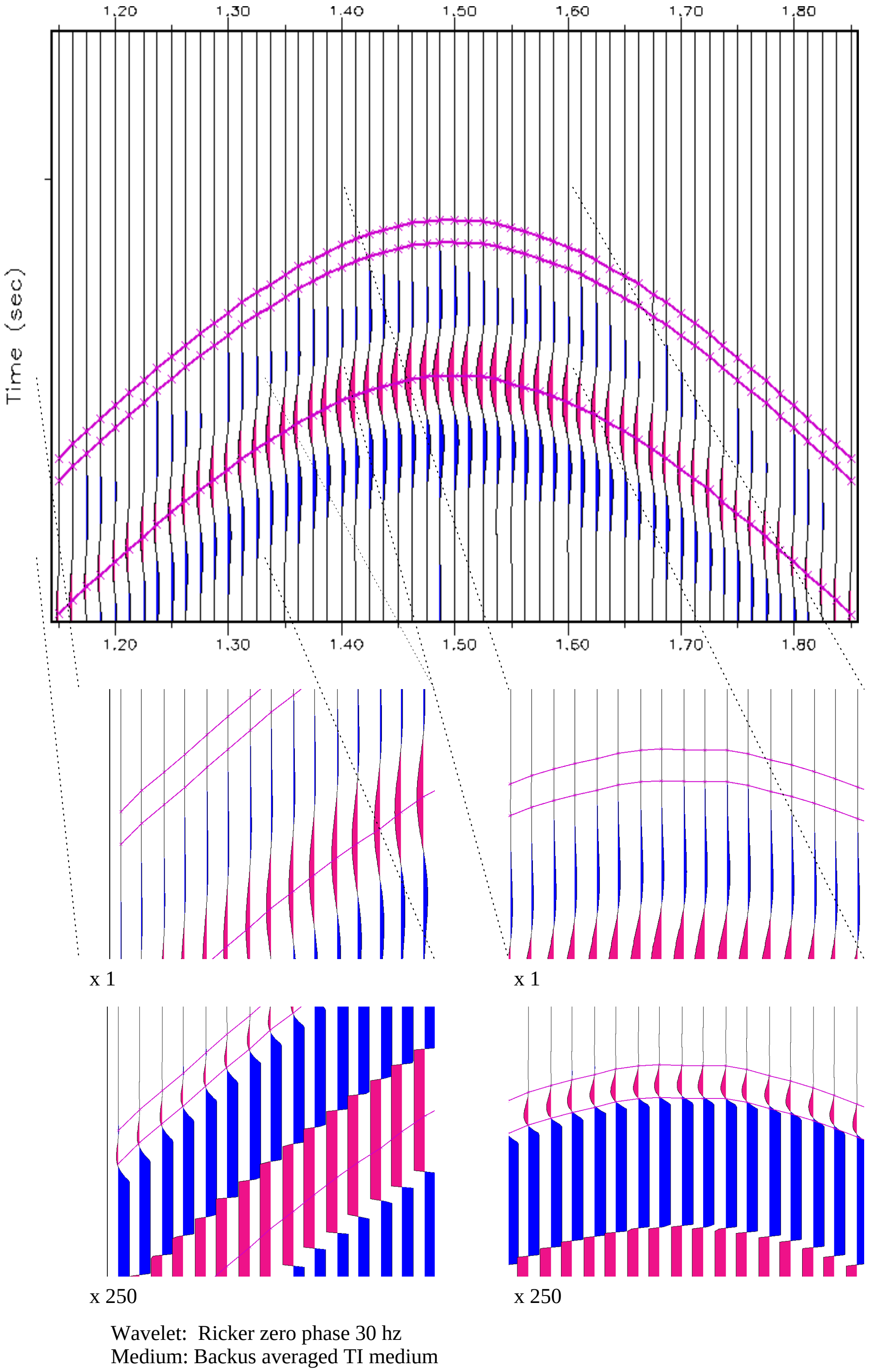

Figure 3.24: Seimogram from a 30 Hz zero-phase Ricker wavelet propagating through the TI replacement medium of the lime-shale model.

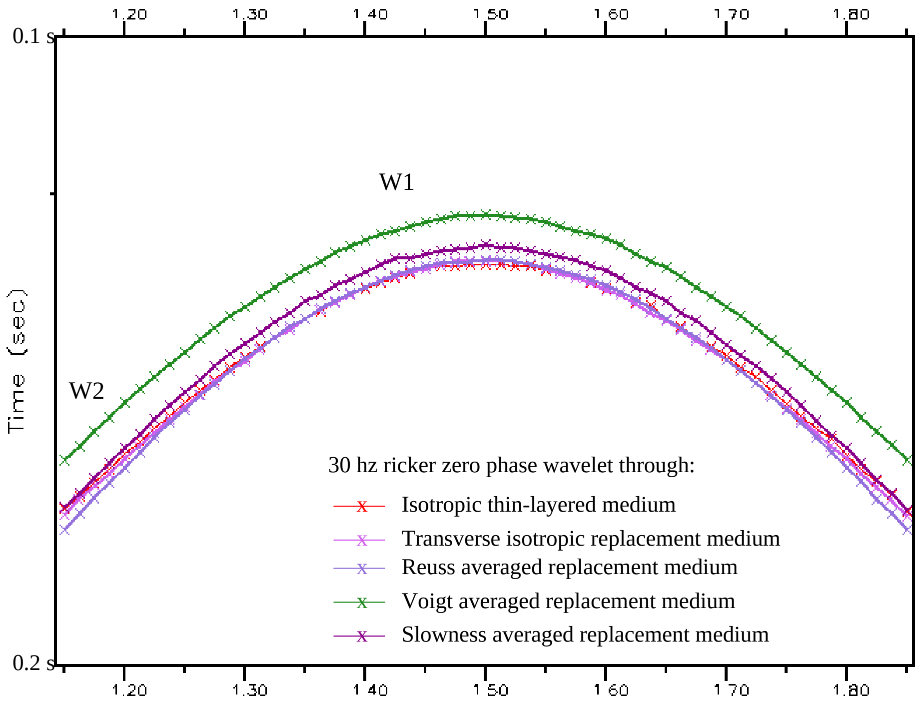

Figure 3.25: Comparison of travel times for the 30 Hz frequency through the thin-layered and the various replacement models.

The t_{fb}-lines from the thin-layered model and the four versions of upscaled media are plotted together in figure 3.25. In order to discern the individual curves, a more detailed plot of three of the curves, together with corresponding lines from the 100 Hz modelling, is given in figure 3.30. In these figures it is seen that for the 30 Hz simulations, the time-curve from the thin-layered model coincides the best with the curve from the Backus averaged transverse isotropic model. Furthermore, these two curves have a good fit with the curve from the Reuss averaged isotropic medium for the vertically propagating waves and they approach the results from simulation in the slowness averaged replacement medium for the outermost receivers. All these observations agree with the observations from the snapshots earlier in this chapter.

A comparison with 100 Hz

Comparing snapshots To test the effect from the λ/d-ratio in the small scale model for the correctness of different effective media, I also performed simulations using a Ricker zero phase wavelet of 100 Hz. This modelling provides a λ/d-ratio for the P-wave of approximately 3.6 for the thin-layered model. Snapshots are taken of the wavefields after 125 ms in the thin-layered, the Backus averaged and the slowness averaged models. I do not provide such a thorough presentation of the 100 Hz snapshots as I did for the 30 Hz snapshots. The question of interest is how the 100 Hz wavefront propagating through the thin-layered model fits with those propagating through the Backus averaged and the average slowness upscaled models.

For this comparison, the generated snapshots are contoured, and the outermost contours, marking the first break wavefront, from the three models are plotted together in one figure. The corresponding display is provided for the 30 Hz seismograms, and the two resulting panels are displayed in figure 3.26. This figure verifies that for the 30 Hz wave, involving the largest λ/d-ratio, the Backus averaged model has the better fit with the thin-layered medium for the direcly transmitted P-wave, while for the 100 Hz model, with a smaller λ/d-ratio, the slowness averaged medium has the better fit.

Comparing seismograms The seismograms from the 100 Hz simulations through the thin-layered medium and the Backus averaged medium are plotted in figures 3.27 and 3.28, and a similar seismogram has been generated from a simulation in the slowness averaged model. Again, the time t_{ml} of maximum amplitude in the arriving waves is picked. Assuming that the 100 Hz wavelet consists of one sidelobe ahead of and behind the central maximum amplitude lobe, cf. figure 3.22, inspecting the traces in the two given figures corresponding to the vertically propagating waves gives an estimate of the time delay Δt_{fb} of 6.0 ms for the 100 Hz wave. Plotting the t_{fb}-curve with this delay seems to fit well for the vertically propagating waves in both the thin-layered and the upscaled model. Amplifying the traces 250 times displays however that there is energy ahead of the t_{fb}-curve in terms of additional sidelobes. This energy is visible both from the thin-layered and the homogeneous upscaled model. It is therefore not the result of the small-scale layering but must be attributed to numerical effects, probably caused by too large grid-cells in the spatial model or too large time steps in the simulation. This phenomena has not been studied further, however, nor what conclusions that can be drawn from the observation that the wavelet for obliquely travelling waves in the thin-layered medium is different than that of the vertically travelling waves in the same model, also observed when applying the 30 Hz wavelet.

For comparing the arrival times of the 100 Hz wave from the simulations in the thin-layered, the Backus averaged and the slowness averaged model, the t_{fb}-curves from the three simulations are plotted in figure 3.29. Again, as

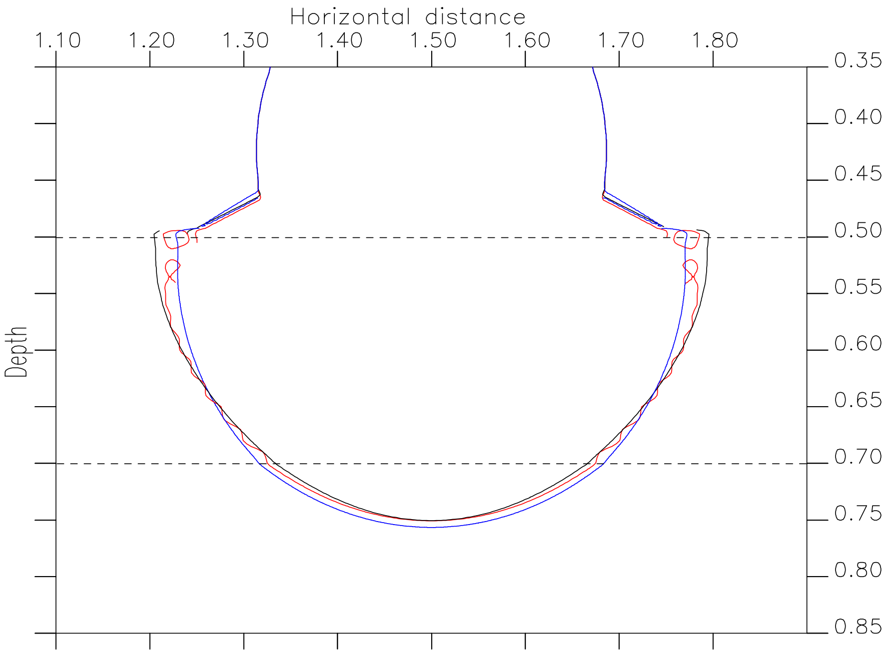

a) Wavefronts from 30 hz Ricker zero phase wavelet

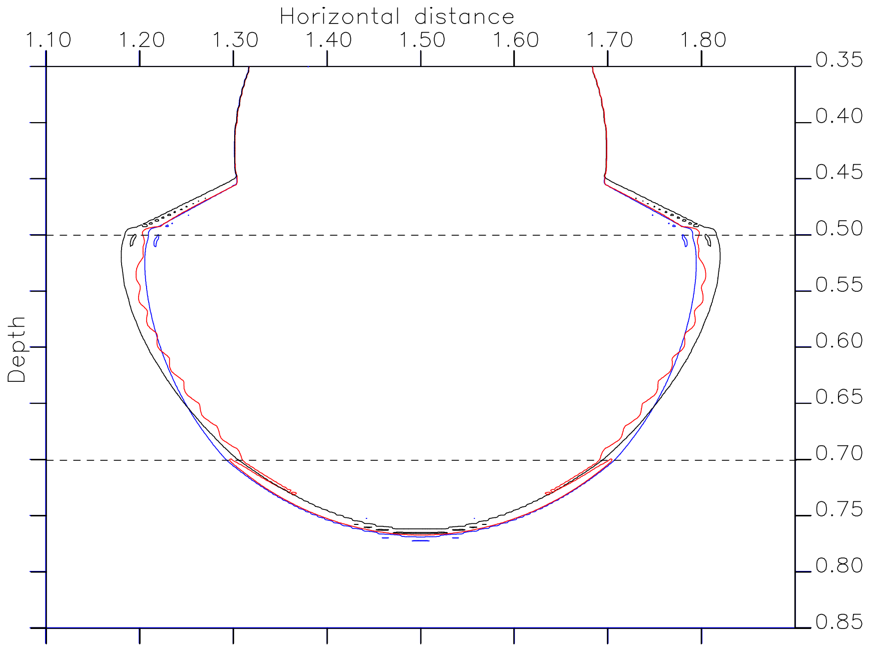

b) Wavefronts from 100 hz Ricker zero phase wavelet

Color of wavefront refers to the specified intermediate medium of the model:

🟥	⬛	🟦
Layered medium	Backus TI replacement medium	Slowness averaged medium

Figure 3.26: Superpositioned wavefronts from the thin-layered, Backus- and slowness averaged media, using a) 30 Hz wavelet and b) 100 Hz wavelet. The figure displays which of the replacement media that is the correct effective medium for the two frequencies.

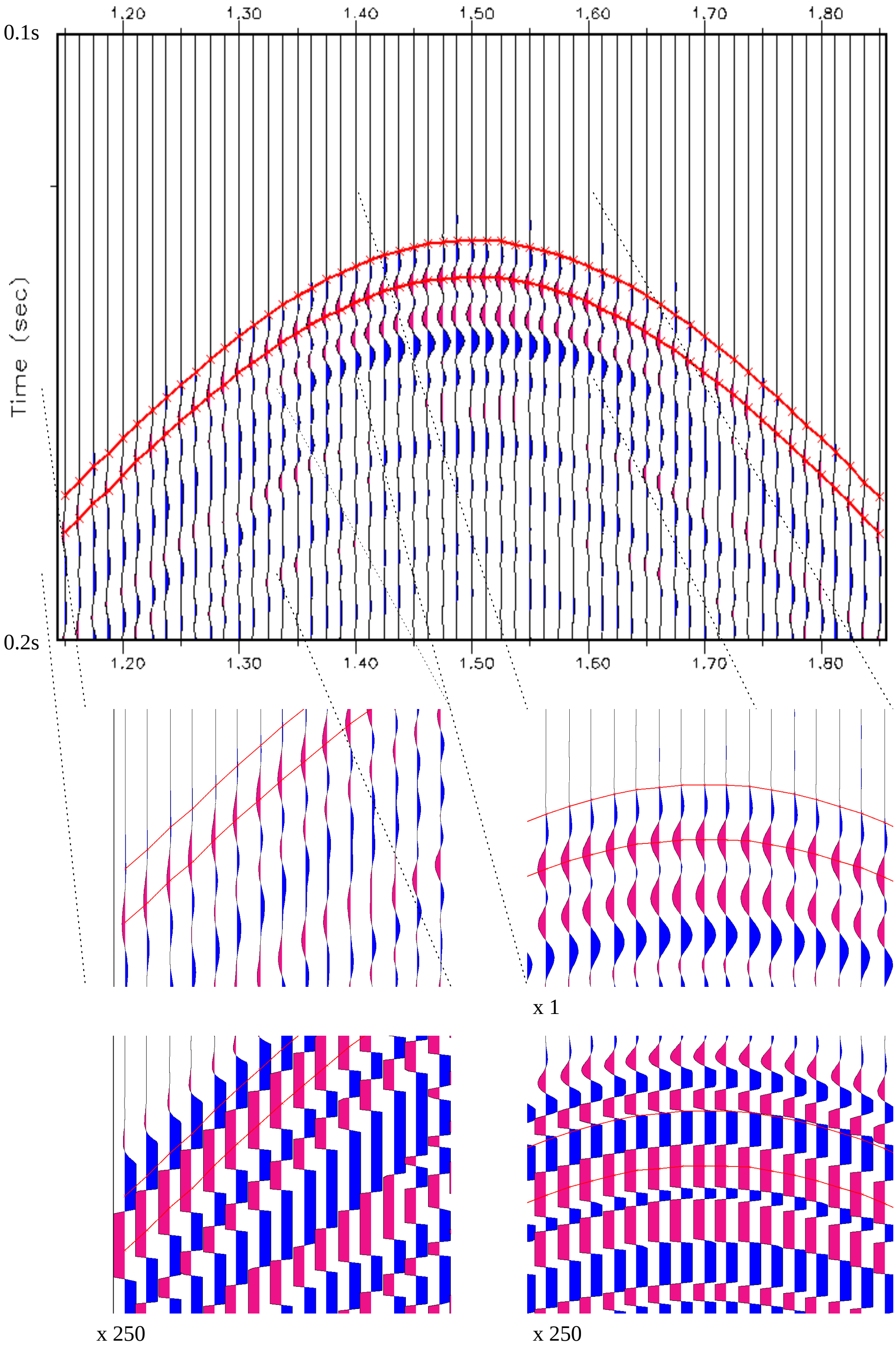

Wavelet: Ricker zero phase 100 hz
Medium: Original thin-layered medium

Figure 3.27: Synthetic seismogram of 100 Hz Ricker wavelet through thin-layered medium

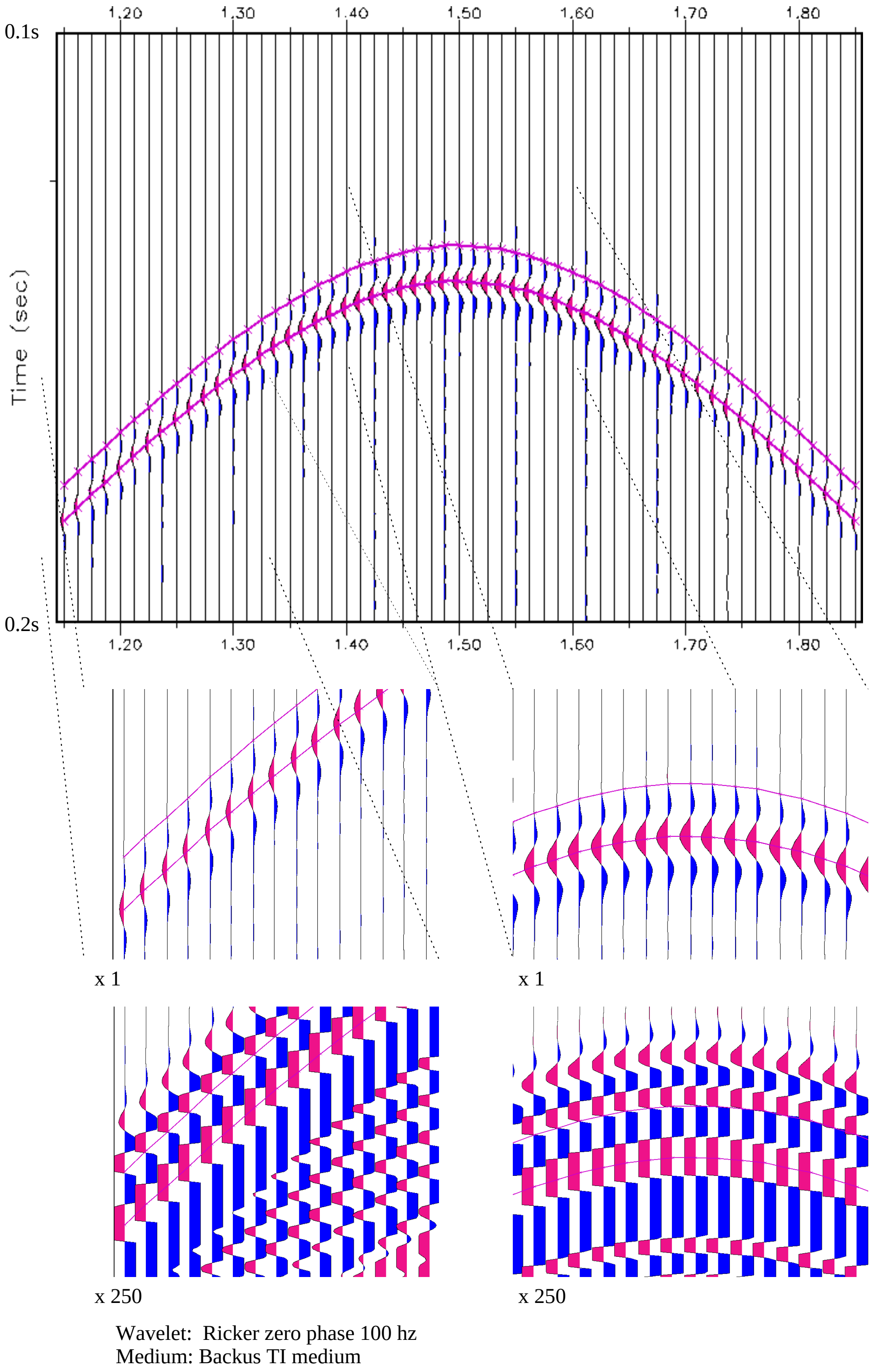

Figure 3.28: Synthetic seimogram of 100 Hz Ricker wavelet through TI replacement medium.

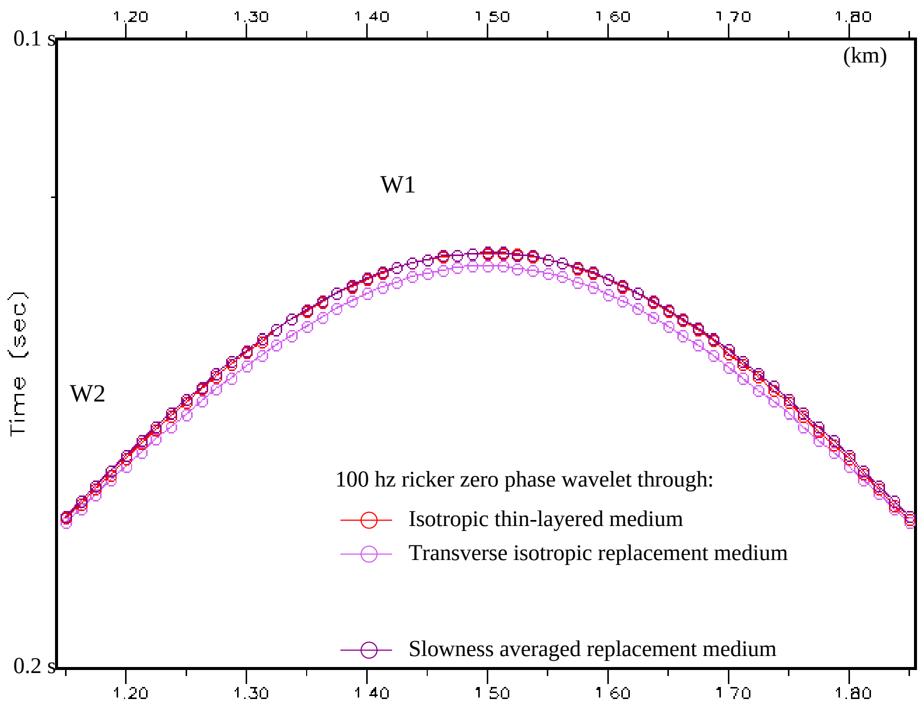

Figure 3.29: Comparison of travel times for the 100 Hz frequency through the thin-layered and the Backus- and slowness averaged replacement models.

I expected from the λ/d-ratio for the 100 Hz wave and the given layering, the arrival-line from the thin-layered model almost coincides with the arrival-line from the slowness averaged model, while the difference between the former and the Backus averaged model is substantial, especially for vertically propagating waves.

To conclude, figure 3.30 displays the t_{fb}-curves for both frequencies from the thin-layered, Backus averaged and slowness averaged models together. As seen in this figure, the thin-layered model behaves like the Backus averaged model for the 30 Hz wave and like the slowness averaged model for the 100 Hz wave. This conclusion, supported by the observations from the snapshots, is in good correspondence with the statements of Marion et al. (1994) regarding the scale effects on velocity dispersion. This effect of the different λ/d-ratios also explains the good correspondence between the S-waves in the thin-layered and slowness averaged models for the 30 Hz wave case, since the S-waves are shorter than the P-waves. For this frequency the Swave thus has a λ/d-ratio below the effective medium limit.

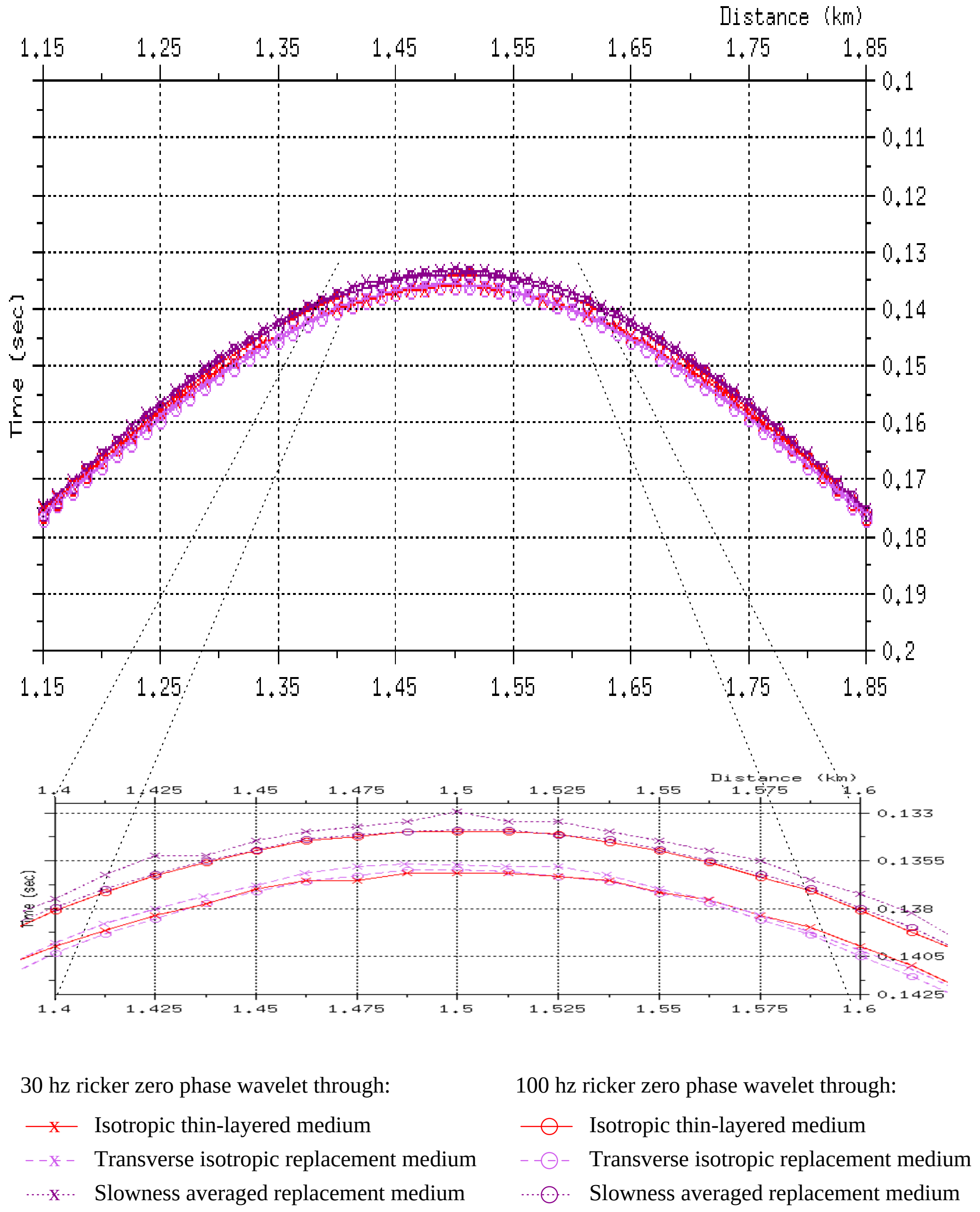

Figure 3.30: Traveltime curve for wave propagation through original thin-layered medium converges to traveltime curve through slowness averaged medium for high frequency wavelets, and converges to traveltime curve through Backus averaged medium for lower frequency wavelets.

3.4.2 Dipping layers

Finally I will consider the effect of dipping layers in the thin-layered model in terms of large scale behaviour by comparing snapshots of wavefields generated in the two thin-layered models, with horizontal and ten degrees dipping layers correspondingly, and compare these with the wavefields generated by some of the upscaled models, in specific with the corresponding transverse isotropic models with vertical and dipping symmetry axes respectively.

Figure 3.18 displayed the 2-D model of containing the intermediate slab of 10 degrees dipping thin layers. Compared to the horizontally-layered model, the properties are identical except from the orientation of the layering. Thus, the isotropic upscaled models are identical for the two models. Regarding the transverse isotropic upscaled media, in terms of material properties these will also be identical for the two small-scale models, except from the direction of symmetry axis which will be dipping 10 degrees to the left, corresponding to the dip of the layers.

Figure 3.31 a) shows the wavefield in the original dipping layer medium. This wavefield is compared to that of horizontal layering in figure 3.31 b), where the contours of the latter is superpositioned in red on the snapshot of the former contoured in blue. The most obvious difference is the anti-clockwise skew of wave energy. For example the 0.25 contour of the direct P-wave propagating downwards shows this effect clearly. Likewise, the characteristics of the near horizontal P-wave in the middle layer, in terms of energy, correspond to a anti-clockwise rotation, seen the best on the left side.

Careful inspection of the P-wavefronts also shows that in the direction down to the left, the dipping layers wavefront is ahead of that of the horizontal layers, while in the direction down to the right the horizontal layers wavefront takes the lead. This is actually what we would expect, since maximum and minimum velocity in thin-layered media is normal and parallel to the symmetry axis of the medium. Since the wave propagating down to the left moves more parallell to the layering of the dipping layer medium than to the horizontally layered medium, the wavefronts of the former will propagate faster. The opposite is the case for the wave that moves to the right in the figure.

The wavefield of the transverse isotropic replacement medium with dipping symmetry axis is plotted in figure 3.32 a). The simulation shows a good reconstruction of the wavefield, especially regarding the P-wave, showing the same skew of the direction of the maximum energy in the head P-wave in the anti-clockwise direction. Concerning the locations of the wavefronts, the TI-medium clearly fits better than any of the isotropic replacement media,

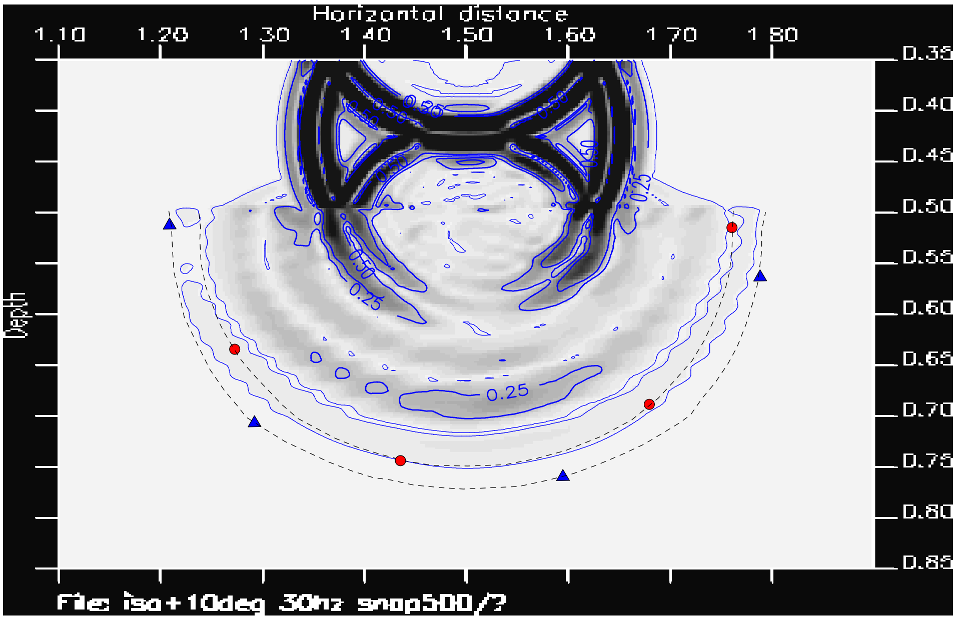

a) Isotropic medium dipping 10 degrees

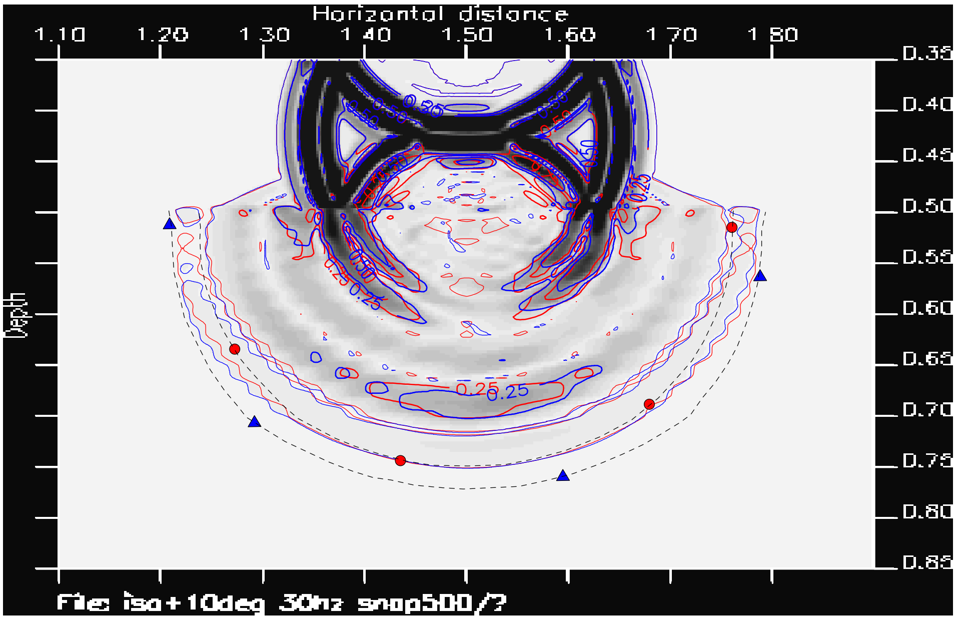

b) Snapshot from (a) with overlay (red contours) from equivalent horizontally layered model

Figure 3.31: Snapshot of 30 Hz wavefield propagating through dipping thin-layered model (a) versus horizontal thin-layered model (b).

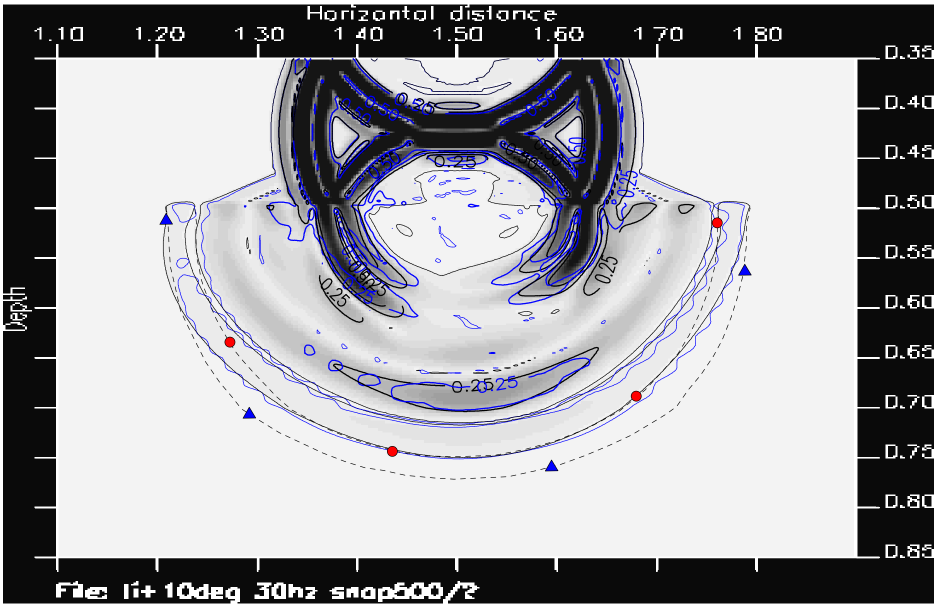

a) 10 degrees dipping TI medium overlaid with blue contours from original dipping medium

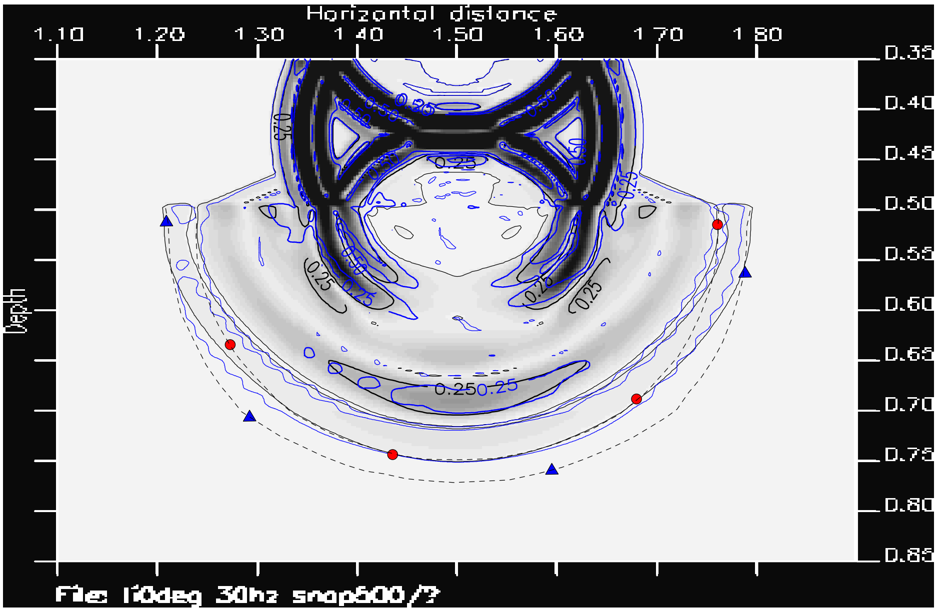

b) Horizontally oriented TI medium overlaid with blue contours from original dipping medium

Figure 3.32: Snapshots from 30 Hz wavefield propagating through dipping transverse isotropic replacement media (a) versus non-dipping transverse isotropic media (b).

and better than the TI-medium with vertical symmetry axis, which is plotted together with the original field in figure 3.32 b).

The wavefield simulation in the TI-medium with dipping properties is time and memory-consuming, however, since the orientation of the symmetry axis has to be stored, and the elastic parameters have to be transformed from a local rotated system to the global coordinates by applying the Bond transformation described in chapter 2. However, even though wave simulation in transverse isotropic medium is time-consuming, there are good reasons for operating on an upscaled medium instead of the fine-scaled medium. This dipping medium upscaling gives a recipe for how to represent a horizontal package of cross-layered sediments. The small scale layering may then be dipping, while the large scale properties can be extrapolated horizontally. This leads to the subject of the next chapter, focusing on the interpolation of well data. The subject of upscaling and that of interpolation or extrapolation are related, and one of the primary reasons for upscaling is to get to a scale on which we have good indications on how the parameters correlate between wells.

3.5 Conclusions

Heterogeneities in the object of seismic investigation are found on every scale from the microscopic scale to the scale of basins. Small scale heterogeneities below resolution limit is represented by an effective medium. Well measurements sampled at desimeter scale can be upscaled to surface seismic scale by considering log samples to be thin layers that can be upscaled by moving average smoothing.

The simulations of the bi-periodic medium for large wave-length to layer thickness ratios show that Reuss averaging the thin layer parameters gives the best result of the isotropic effective media. For small λ/d-ratios averaging slowness gives the best results.

It was shown that Backus averaging gives an improved upscaled model compared to isotropic upscaled media for large ratios of wavelength to layer thickness. The improvements are specificly in the non-vertical directions. Along the symmetry axis the velocities of the TI and Reuss averaged replacement medium are equal, and for studying waves propagating close to vertically in a horizontally layered medium, an isotropic effective medium may be sufficient.

The λ/d-ratio is smaller for the S-waves than for P-waves. We observed in the 30 Hz simulation through the 10 m layering model that for the S-wave slowness averaging gives the best simulation while Backus-averaging gives the best simulation of the P-wave. This raises a question of whether it is possible to construct a replacement medium compatible to both the P- and S-wave in such a case. This question is open for more research.

For layers that are non-horizontally oriented, the dip effect is maintained in the upscaled medium by using a transverse isotropic representation with a corresponding orientation of the medium symmetry axis.

Since any measurement can be considered as an upscaling of the underlying medium given on an even smaller scale, a conclusion from the two-step upscaling experiments on the real well data is that the large scale upscaled medium is significantly affected by ignoring anisotropy present in the small scale medium because of microscopic heterogeneities. Upscaling of a layered transverse isotropic small scale medium causes a different anisotropy than the result of upscaling an isotropic layered medium. The common assumption that the sampled well is isotropic on log scale may be false, and this may cause serious errors in further upscaling.

The filtering effect of the smoothing function is given by the length and shape of the averaging window. The transfer function bandwidth gives the needed sampling density of the upscaled log to avoid aliasing.

We have also considered filtering effects of variations in inclination of layers and variations in wave velocity requiring a dynamic window size for maintaining a constant windowlength to wavelength ratio in the averaging.

We also observed that the vertical velocity of the Backus averaged well data was not always confined by the Voigt and Reuss limits. At a few segments the Thomsen parameter epsilon was negative, which means that the velocity along the symmetry axis is greater than that of waves propagation perpendicular to this. This seems to contradict the (unsupported) assumption that the Reuss and Voigt averages defines the lower and upper limits on medium stiffness for any medium.

Chapter 4

Effects of interpolation of well data

4.1 Introduction

In the previous chapter the focus was on upscaling the reservoir model, i.e. reducing the spatial resolution of the model while attempting to preserve its overall behaviour related to e.g. low frequency wave propagation. Apparently, the focus of the present chapter is the opposite, that is to increase the amount of information in the model. It will be evident though, that there is no contradiction in claiming that both operations are necessary for constructing a reliable model.

We have seen that log measurements provide information on the scale of decimeters at the locations of wells, giving a detailed description of the geology along the borehole. However, provided with no additional information, the complementary volume of the reservoir is unknown. The task of the modeller is then to estimate reasonable property values to this non-sampled volume. The methodology involved in this operation is to utilize available data from well and surface measurements and assure that the assigned values relate to this information.

Seismic inversion, applying modern methods such as AVO-analysis, will give an estimate of the properties in the inter-well volume. As have been stated in previous chapters, the data resolution of such methods often is on a coarser scale than what is requested. In addition the derived parameters from seimic inversion are the *elastic* parameters, from which the transformation to parameters such as porosity, permeability and hydrocarbon content not necessarily is one-to-one. Both these factors, the requested model resolution and the different parameter domains, suggest the application of a different approach: to determine the unknown values based on nearby well measurements. This interpolation involves making different choices, such as deciding on the geometry of spatial correlation and choosing interpolating functions. Both these clearly affect the resulting model, and the goal of this chapter is to study the effect of different parameters involved in the interpolation process.

Historically interpolation has been a most important issue. Names of fameous scientists such as Gauss, Newton and Bessel are all associated with it. In the sixteenth and seventeenth century the matter of interest was that of determining the locations of the planets and other heavenly bodies at times between those of observation. In this application some a priori assumptions regarding their motion were held, like that the bodies were moving in circular or elliptical orbits according to the law of gravity. Likewise, in the earth sciences, a general assumption widely held in the interpolation of rock properties between locations of observation, is the principle of stratification, *i.e.* that sediments are deposited in layers. William Smith, when surveying the geology of western England in the beginning of the nineteenth century, for the purpose of constructing new channels, observed that the studied sediments were found to be ordered "like slices of bread and butter." The layers were stacked in a sequence that was unvarying from location to location. Equipped with this basic stratigraphic principle, a simple geologic model could be constructed by interpolating the identified layers between the sample locations.

However, this principle of stratification alone is not a good enough basis for constructing a realistic model. First we need the correlation geometry of the assumed stratification in the object. Secondly, since measurements show that rock properties may vary from location to location within an identified layer, we need a function for interpolating the measured parameter values along the stratification geometry between the provided samples. Influencing both the choice of geometry and interpolator is the matter of scale or resolution of the model. In this chapter we will show that scale indeed is not just an issue of economical model representation and correct and efficient computer simulation, as we looked on in the previous chapter, but also related to the procedure of model construction by interpolation.

For the sceptical reader who may consider conventional interpolation as obsolete in reservoir characterization, I would like to give a few remarks in defence of its application before addressing its main issues. My first remark is to acknowledge that the modeller has no a priori correct choice in the selection of parameters. In principle the relationship between the sampled material in a well and its surroundings is indeed unknown. The principles of stratification makes no claims that there are not internal variations within

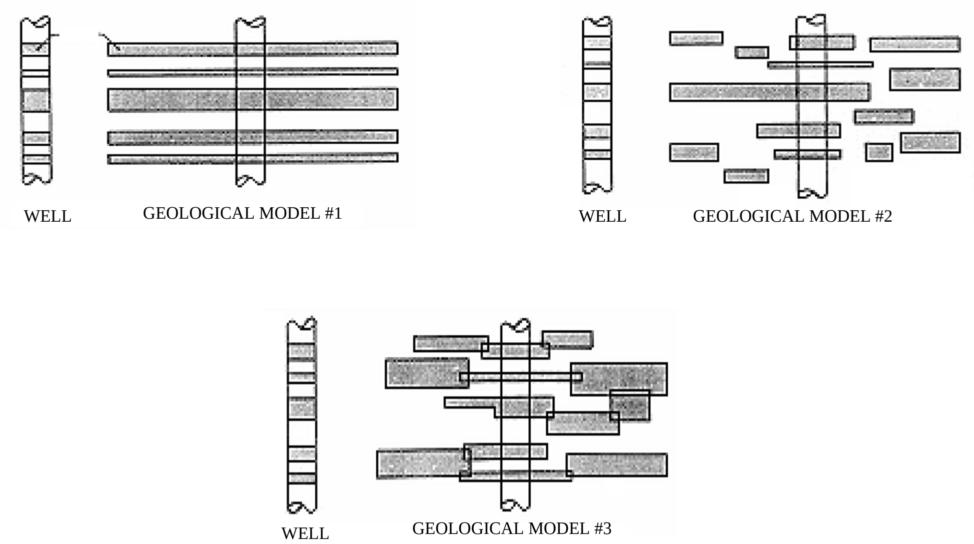

Figure 4.1: Three different interpretations of the relations between a well and its surrondings. (From Haldorsen and van Golf-Racht, 1992)

sedimentary units. For example in an alluvial environment, fluvial channel sands and flood plain shales will both be present, merging into each other and the one pinching out into the other. On a finer scale, *e.g.* within the sand bodies, internal variations will also be present. Thus, as illustrated in figure 4.1, many geologic models are possible to deduce from a given set of well measurements. In such cases, proper scaling is an important issue. For example, in the alluvial deposition case, that may not support interpolation of sand and shale units separately, a solution could be to interpolate the overall average properties of the two components, *i.e.* the upscaled parameters. A problem with this upscaling, however, is that the resulting spatial model might not comply to the purpose of constructing the model, due to the resulting coarseness in its resolution.

An alternative approach to classical interpolation, acknowledging the uncertainties involved in the procedure, is that of geostatistics. In this case the internal spatial variations in the units are estimated and quantified in terms of spatial correlation functions to be used for obtaining geostatistical realizations of the reservoir. For a brief introduction to the concepts of geostatistcs, see Journel (1989) or Isaaks & Srivastava (1989). Here fundamental concepts such as variograms and covariance and basic procedures for obtaining realizations of the stochastic model are explained. A general class of such procedures is that of sequential simulation, which includes different

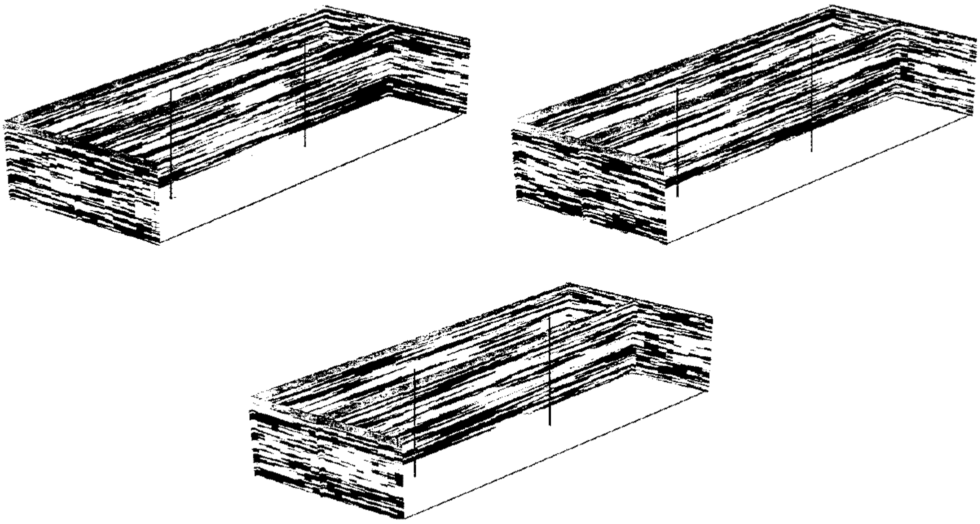

Figure 4.2: Three geostatistical realizations of the Statfjord formation. (From Dubrule et al., 1998)

methods of kriging.

The Association of American Petroleum Geologist publication "Stochastic Modeling and Geostatistics", edited by Yarus and Chambers (1994), contains an additional list of useful books and articles on the topic. In addition to this it includes several case studies illustrating the usefulness of the stochastic method.

Regarding the predictive ability of stochastic modelling compared to traditional interpolation, Laslett (1994) has performed a comparison concluding that "in the cases examined, kriging sometimes outperforms splines by a considerable margin, and it never performs worse than splines". When geostatistics was introduced, it was, according to Laslett (1994) "countered by widespread negative reactions ranging from mild to total scepticism". However, recognizing that different modellers, despite presented identical data, will produce different models, and also recognizing that there is a need for quantification of the uncertainties involved, geostatistics has now been widely accepted as part of the modelling toolbox.

Figure 4.2 from Dubrule et al. (1998) shows three realizations of a geostatistical model, based on spatial continuity parameters from the Statfjord formation model of Johnson and Krol (1984) and constrained by two wells indicated on the figure as vertical lines. These well constrainments imply that all realizations have equal property values at these locations, while at different locations the properties generally may differ from one realization to the other. The overall properties of the three models are the same, *e.g.* with respect to the sand-shale ratio and the spatial correlation functions. Thus, based on the given presumptions, the realizations are equally valid. In their recent article, Dubrule et al. (1998) present a general algorithm for geostatistical modelling that includes seismic modelling to guide the applied sequential simulation towards the most reliable realization. Geostatistical parameters are supplied from 3-D seismic interpretation, a priori assumptions and well data analysis, and initial constraints are provided by the well measurements. In short, their simulation is performed as follows: A random location in the horizontal plane is selected, for which a great number of realizations of "synthetic wells" are produced according to the stochastic parameters. A synthetic seismogram is produced from each realization and compared to the actual seismic trace from this location. The synthetic well whose seismogram agrees the best with the seismic data is selected and added to the set of constraining wells. From this point the process is repeated for a next location, now having increased the number of constraining wells with one, repeating this untill the whole model is filled. Dubrule et al. (1998) has thus presented a procedure that incorporates seismic inversion with geostatistical modelling.

This promising advance of stochastic modelling, supported with the mentioned conclusion of Laslett (1994), may cause one to wonder whether traditional interpolation is obsolete and thus not worth studying. This proposition I will like to challenge. The first such reason is that in many cases the model has such a strong spatial correlation of properties that the introduction of geostatistics seems to be unnecessary. A traditional interpolation will surely do. The second reason is simply that interpolation may be useful even if the primary method for model construction is geostatistical. This is so because the general assumption that the geostatistical parameters are constant throughout the layer to be modelled may only be a first approximation. For example, when studying an object, the overall spatial continuity, either its range or its orientation, may change from one part of the object to the other. The geostatistical parameters may then be calculated over a sufficiently large volume in different parts of the object and then interpolated. I believe the similarities to moving window statistics and interpolation of upscaled parameters are evident.

Thus, though new metods of model construction may have arisen, the concepts of interpolation are still very important. And these concepts are the issues of the following sections.

4.2 The basic interpolation algorithm

A prerequisite for discussing the effect of choosing different parameters involved in the interpolation procedure, is to give an account of the principles of interpolation or extrapolation algorithm. For the following discussion, the consepts will be illustrated in figure 4.3.

I will only consider the two dimensional model construction, but the concepts may easily be extended to 3-D. Panel a) of the referred to figure illustrates the input data to the algorithm. It consists of well data and correlational horizons. This figure panel displays three wells and three horizons. The wells are given as discrete samples, with spatial position parameters and sampled property values. The samples together constitute the well trajectory. In this example, one of these is vertical while the others are deviating.

The correlation horizons are given by a set of sample points containing their spatial position. In cases where the samples of a horizon do not form a simple straight line and the horizon is sparsely sampled, an input parameter is needed stating the type of interpolating function to be used to draw the line between the samples. The available options here are the linear and the spline interpolator.

I will later show that the wells generally are resampled as part of the initial step of the procedure to form equal number of samples in each well involved in the spatial interpolation. Therefore, each well given as input needs to be accompanied with parameters specifying the type of interpolation performed in this preparing resampling of spatial location and parameter values. As the trajectory of the wells usually are nearly linear at the scale of the resample interval, the effect on the trajectory, in terms of spatial parameters, of choosing different interpolators is only moderate. However, regarding the property values at the resampled locations, these may indeed be influenced by the selection of different interpolators, as property values, in the case of a thin layered medium, may vary significantly on the scale of sampling, only assumed to be constrained by the Nyquist frequency.

Additional parameters to be given for performing the model building are the parameters defining the final grids to be generated. This involves stating the spatial range of the grid and the sample density in the x- and z-direction.

Before performing any kind of interpolation or resampling, the correlation field has to be defined based on the provided horizons. At any point in the model, the path of correlation must be possible to calculate. This establishment is fundamental for drawing correlation lines between the given wells; lines along which the sample values are to be interpolated or extrapolated.

The definition of the correlation field depends on the number of horizons given as input parameters. If one single horizon is given, the field is defined

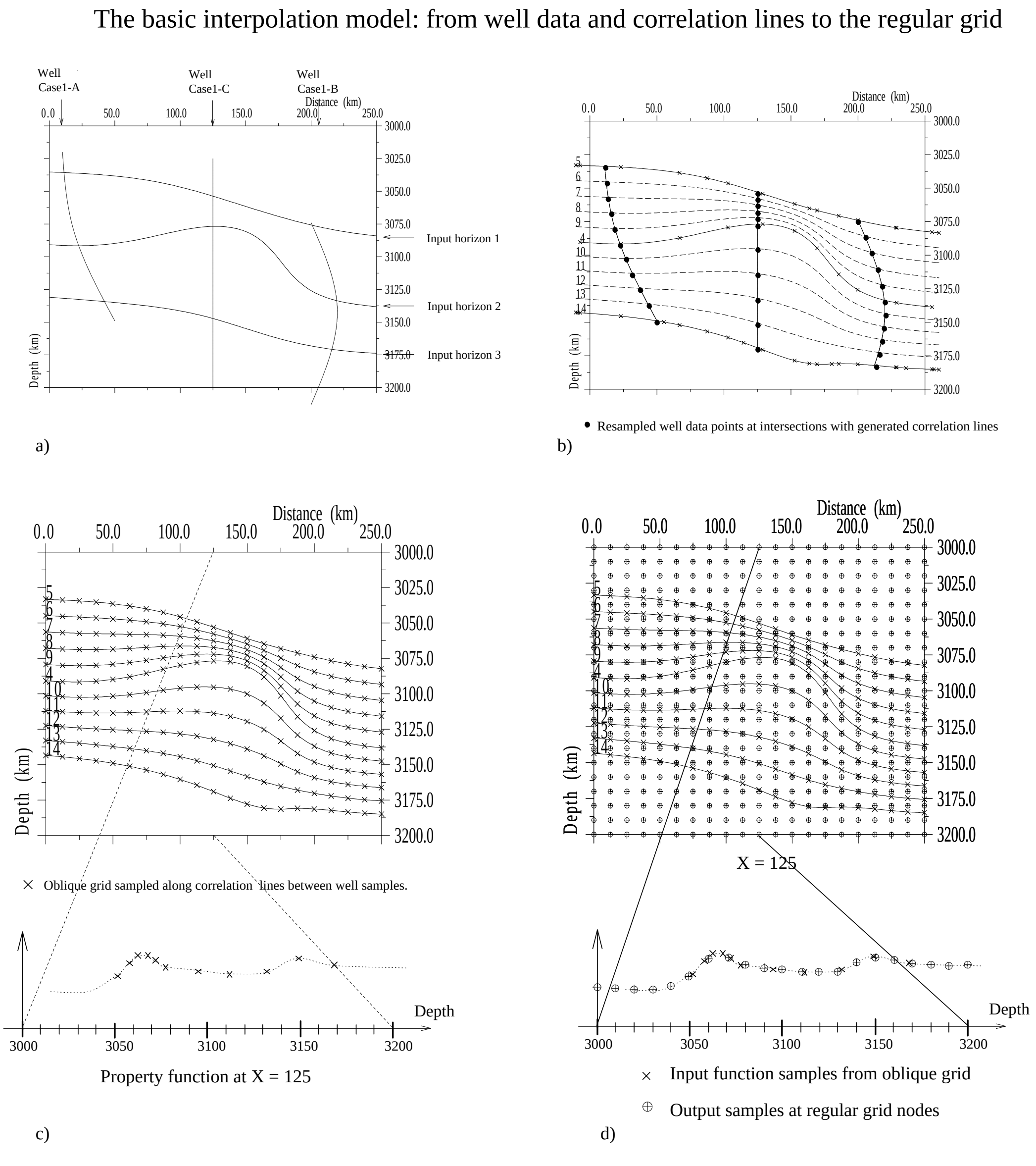
The basic interpolation model: from well data and correlation lines to the regular grid

Figure 4.3: The conceptual model for interpolation of welldata to construct a 2D model. See text for explanation.

such that the vertical distance from any correlation line to the given horizon remains constant along this line. In this case all correlation lines in the correlation field are parallel. If the input is two horizons, the field is defined such that along the path of any correlation line, the ratio of the vertical distances to the two provided horizons is constant. For example, the correlation line l passing through a point A at (x_1, z_1), at which point the vertical distance between the horizons h_1 and h_2 is d_1 and the vertical distance from A to h_1 is s_1, the vertical distance s between l and h_1 at any position x is given by $d \cdot s_1/d_1$, where d is the corresponding distance between h_1 and h_2. A special case occurs when this distance d as a function of x is constant, where the given horizons are parallel, causing all the correlation lines will be parallell. If more than two horizons are provided, the principle of using two of the given horizons is still used. Two of the horizons are then selected, which ones depending on the location of calculation. When the location is between two given horizons, these are selected, while the nearest two horizons are selected in the case where the location is above or below respectively the upper or lowest given horizon.

The vertical extent of the provided wells constrains the area where the correlation field can be utilized. If only one well is given, the correlation line passing through the uppermost sample defines the upper limit of this area, while the line passing through the lowermost sample defines the lower limit. If more than one well is provided, these limits are defined to be the upper and lower lines passing through all provided wells. Surely, an interpolation or extrapolation outside this area would be meaningless if only one well is given, but also in the multiple well case interpolation outside this region should be avoided. This is so because generally a discontinuity is generated in the resulting property field at these borders if interpolation is performed also outside it. This discontinuity is generated because there are fewer samples governing the interpolation along each correlation lines outside this border than inside of it, related to the fewer wells that are intersected.

Having defined the correlation field with its spatial borders, the interpolation or extrapolation procedure can be performed in three steps:

The first step is to generate a finite number of correlation lines and to resample the given wells at the locations of intersection with these lines. The result of this step is illustrated in panel b).

Then second step is to interpolate or extrapolate the independent property functions along each of the correlation lines. The interpolated functions are then sampled at the x-positions where grid samples are requested for the final regular grid. If k is the number of correlation lines and n is the number of grid-nodes along the x-axis for the requested $m \times n$ grid, the output of this correlation step of the process is a generated $k \times n$ grid. The geometric structure of this grid is illustrated in the upper half of panel c). At each x-location of this grid, property values are thus provided at k depths corresponding to the correlation lines.

The final step is performed by interpolating property values vertically at each of these x-locations, based on the k calculated property samples. The inferred property functions are then, as illustrated by the lower part of panel c) and d), resampled at the z-values of the requested regular grid, providing property samples at the grid nodes specified by the requested regular property grid. The circle shaped samples in the upper part of figure 4.3 d) thus illustrate the final result of the interpolation procedure.

In the described steps, three main parameters determine the output of the total operation.

The first is the geometry of the correlation field, the issue to be discussed in the next section. The second issue is that of selecting the functions of interpolation, the parameter domain of interpolation and the interpolator itself to be used along the generated correlation lines. The third issue is that related to model sampling and the effect on the model information by different sampling densities in the three sampling steps in the operation.

In the first resampling, the given wells are resampled. Then the interpolated function along each correlation line is sampled at regular x-values, and finally the resulting skew grid is resampled at regular z-values. According to the sampling theorem, a spatial function has to be sampled at a minimum of twice per wavelength to prevent distortion by aliasing. The issue of aliasing relates to the first and third sampling step of the full operation; the vertical or near to vertical resampling.

To prevent aliasing in the first step, the wells have to be resampled with a sufficient density. The resample points are determined by the intersection points between the instantiated correlation lines and the wells. To prevent aliasing, a sufficient number of correlation lines has to be generated in the correlation field.

In the final step, where the skew grid is resampled vertically to produce the requested regular grid, the aliasing issue is related to the requested sampling density of the output grid compared to the vertical signal frequency of the input grid. This frequency must not exceed the spatial Nyquist frequency determined by the output sampling density. Thus, here somewhat the converse constraints to that of the first step is put on the density of the generated correlation lines. If not the signal represented by the columns of the skew grid is oversampled, the final step requires a minimum allowed separation on the corresponding correlation lines.

In some cases the maximum allowed separation of the correlation lines due to the signal frequency in the input wells may still cause undersampling in the final step. In such cases one solution is to perform upscaling of the input wells before performing the interpolation procedure, the subject of the previous chapter. An alternative option is of course to increase the sample density of the output grid.

The sample issue can be illustrated by the already referred to figure illustrating the interpolation concepts, figure 4.3. Let us assume that the three input wells are given with sample density equal to the resampled outer wells in panel b), and that the maximum frequency of each of the three wells corresponds to this input sampling density, *i.e.* none of the wells are oversampled. According to the correlation field, a selection of correlation lines then has been generated, and the wells have been resampled. From the above discussion and the mentioned frequency assumptions, it should be clear that the two outer wells are well represented by this resampling. The middle well, however, is clearly undersampled in its lower part for the given selection of correlation lines, due to the expansion of the correlation field in this part of the object. To avoid a distortion of the information given in this well, more correlation lines should be generated in this lower section of the field, producing a sampling density equal to that of the outer wells. Surely this increase of correlation lines will increase the sampling density of the lower parts of the outer wells too, but an oversampling does not distort the signal of the wells. Similarly, a proper sampling of the outer wells in their upper parts causes an oversampling of the corresponding part of the middle well due to the compression of the correlation field in this part of the object.

In panel d) the resulting skew grid is resampled. In this example, the vertical sample interval of the regular grid is approximately equal to the vertical sample interval of the skew grid on the left and right hand side of the grid. In the middle of the object, where the skew grid is compressed and stretched, the vertical sample density of the regular grid is respectively smaller and greater. In cases where the sampling density is larger for the skew grid, there is a possibility of undersampling in the generation of the regular one. In this example, however, the upper middle portion will not suffer from aliasing, since we already know that the spatial frequencies in this region is mainly dependant on the corresponding frequencies of the input middle well, which we assumed were upper band limited causing a non-aliased signal when sampled at the density of the resampled left and right well in panel b). The vertical sampling density of the final grid exceeds this density, and thus the skew grid will not be aliased by the final resampling. In other words: the initial oversampling exceeded the final undersampling.

The information contained in the lower middle part of the skew grid is not distorted by the final resampling. However, the information here already suffer from aliasing due to the unsufficient resampling of the middle well in a previous step of the interpolation. Surely no operation can restore this distortion, so the final regular grid will still contain an aliased parameter field in this part.

Before leaving this issue, imagine that only the outer wells were given as input to the previous example. In this case the interpolation lines generated in the previous example and displayed in panel b) are sufficient to preserve the information given in the two wells, and there is no aliasing in the resampled wells and the resulting skew grid. However, when this grid, represented in panel c), is resampled to construct the final grid, the property field is likely to be distorted by aliasing in the compressed region, where the vertical sampling interval of the input grid is less than that of the output. To prevent this, either the input wells must be upscaled, or the vertical sample interval of the output grid has to be decreased.

4.3 Geometric correlation effects

From the discussion of the interpolation algorithm above, it is evident that the correlation horizons given as input to the procedure are of vital importance for the result. The horizons define the general orientation of the stratification of the object. From the discussion of the sampling issues of the spatial model, it is also obvious that geometric features of the correlation field affect this.

To study the mere effects of geometry, the case of extrapolation, where only one well is given, is the most illustrative one. The effects of interpolation, involving more than one well, is the theme of the next section.

A model constructed by pure extrapolation contains no variations along the provided correlation lines. Clearly this is a strong simplification of reality, but it serves well as a first approximation of the object.

If seismic interpretations of the reservoir are available, these will give guidance for the correlation geometry. In figure 4.4 data from one provided well is extrapolated according to three different geometries. Assuming property variations along the well borehole, differing models result from the extrapolations. The sediment package to be determined is confined by an upper and lower surface, forming a wedge shaped package to be filled by correlating values from the well. The upper correlation geometry is defined by entering these two surfaces as input to the correlation procedure, forming a divergent wedge structure of the internal stratigraphy. The stratification displayed below is created by entering only the top horizon as input to the correlation procedure. Thus, the stratification of the package is created parallel to the top of the layer, causing a downlapping structure with the sediment lay-

a) Divergent wedge

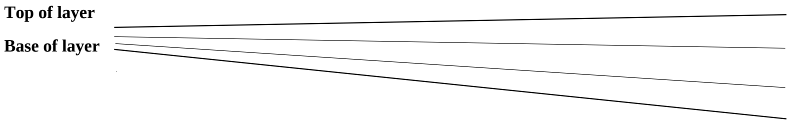

b) Onlap or downlap (baselap)

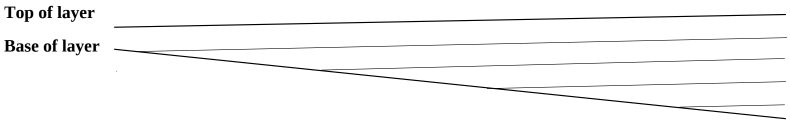

c) Erosional truncation

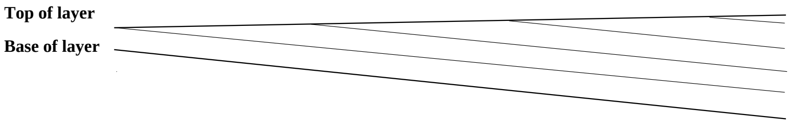

Figure 4.4: Different geometries of correlation

ers terminating against the lower surface. In the final example, the lower horizon in entered as input, causing the sediments to terminate against the upper surface, a structure that can be interpreted as an erosional truncation. Clearly the effect of the different choices are strong on the resulting model. For example, in the case of downlap the properties at the very left hand side of the wedge are identical to those measured in the upper part of the given well, while in the truncation case, the properties in the left part of the model are equal to those found in the lower part of the well.

4.3.1 Multiple scales of interpolation

Generally the correlation information related to the layering geometry aquired from seismic interpretations provides information about the large scale structures in the object, such as formations and groups. Smaller features, found internally in these structures, such as foresetting structures and cross-layering,

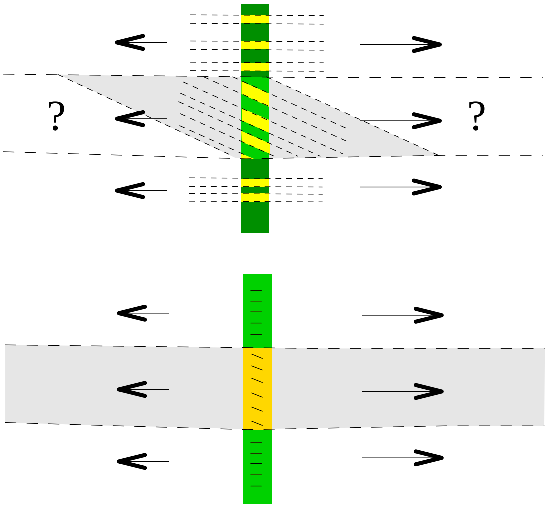

Figure 4.5: Interpolation with correlation defined on several scales.

may be observable in high resolution seismic surveys, but these structures may also be indicated by borehole measurements. Measurements providing such information are *e.g.* dipmeter logs and core samples showing small scale stratification. These small scale structures may have a different orientation of stratification than the encapsulating structure, and in this case the issue to be considered is what set of correlation lines should be used for the interpolation or extrapolation routine. The modeller has to decide what scale he is to interpolate on.

A conceptual model illustrating the issue is given in figue 4.5. Three vertically stacked large scale strata are identified from seismic data, each containing internal structures. Information from a given well indicates that the internal structures of the upper and lower layer are horizontal, while the structures within the middle layer are dipping. The upper and lower layers are easily extrapolated, as the orientation of the correlation lines for the large and small scale features are equal. This geometric equivalence is however not the case for the middle layer. While on large scale the layer is horizontal, *i.e.* the overall properties may be extended horizontally out from the well, the small scale stratification has a different geometry. Clearly the effect of the dipping layers on elastic wave propagation will vanish if the large scale correlation lines are used directly to extrapolate the intermediate layer. On the other hand, if the well data belonging to the middle layer is extrapolated according to the correlation characteristics of the small scale features, parameters can only be assigned to the area of the spatial model indicated by the grey parallelogram displayed in the figure. Outside this area, properties cannot be correlated to well measurements belonging to the proper well interval, and thus the lateral correlation applying this correlation information is limited.

However, referring to the previous chapter addressing the issue of upscaling, it should be obvious that the middle layer can be extrapolated by first upscaling the medium, obtaining a transverse isotropic replacement medium with symmetry axis normal to the small scale correlation structure. This medium may then be extrapolated horizontally, or in any other direction, and still preserve the large scale effect of the orientation of the internal layering.

From this example it is clear that upscaling is a useful tool in case of multiple scales of correlation. Also, interpolation or extrapolation of upscaled values produces a more statistical reliable description of the material than what interpolation on small scale does. I will return to this benefit in the next section, addressing aspects of interpolation between two and more wells.

In the previous section, from the last example it can be concluded that there is a relationship between the correlation geometry, the spatial frequency content in the wells and the required sampling density of the output grid, and the present section concludes by elaborating a bit more on that issue. If the skew grid is generated by extrapolation from one well only, it will contain identical sets of property values in each of its columns. The only parameter that will differ along the non-vertical rows is the vertical position of each sample, as the correlation horizons given as input may cause the grid to be compressed and extended vertically. A result of these compressions or dilatations is that the spatial frequency of the signal may differ from column to column as the sample points are moved closer or more distant from each other. Where the columns are compressed, the necessary sample density to prevent aliasing of the regular output grid, increases. The required sampling density is reduced, however, if the number of correlation lines in the skew grid is reduced. One problem here is however that the frequency content in the given wells may require a minimum sampling density in the prior resampling of the wells to prevent aliasing at that step. In consequence a minimum number of correlation lines is required.

If a limit of maximum sampling density of the output regular grid is given, the dilemma of having too dense correlation lines for avoiding aliasing in the final grid or having too sparse correlation lines to avoid aliasing in the prior resampling of the wells, can be solved by upscaling the input wells before the correlation is initiated.

4.4 Interpolation effects

The previous section considered the case of pure extrapolation. However, a correlation with no variations along the correlation lines is clearly only a first approximation of a more realistic model. If more than one well is given as input, lateral variations in the strata of the object can be modelled by interpolating along the correlation lines between the intersected sample values of different wells. As a result, the grid nodes of the resulting skew grid will contain different property values along the rows corresponding to the correlation lines.

The issue of the current section is to study the effect of choosing different functions in the interpolation step of the correlation procedure. The issue will be discussed under two separate headings. The first regards different functions of interpolation, while the second regards the parameter domains that may be interpolated.

4.4.1 The choice of parameter interpolators

In theory an infinite number of different functions can account for the sample values of a finite set of sample points along a correlation line. Accordingly, there is no *a priori* given answer to which function that most accurately predicts measurements at yet unsampled locations.

One assumption that could be made is that the interpolator is quite simple. For example, if only two sample points are given along the correlation line, the natural assumption is that the predicting function is linear. If the two sample points have equal values, thus the only reasonable function will be constant along the correlation line. Clearly this does not mean that the property variations in nature has to conform to this assumed function. Indeed an additional sample taken in the middle of the two samples of identical values could reveal a very different value, but such an observation cannot be expected and thus predicted on the basis of the provided data.

In some cases, the modeller may do better that assuming a linear interpolation between two given sample points. Given information regarding the geologic environment where the data is sampled may suggest that the interpolated property varies in a different way, *e.g.* that rather than the function itself varies linearly along the correlation line, the logarithm of the function is linear. This examples touches however the topic of the next subsection, which covers the topic of parameter domain in which to operate on in the interpolation step. Clearly to operate the interpolation on the logarithm of the function generates a different parameter field than interpolating the function directly. The point we make here is that where the measurements are identified to belong to a specific sedimentary facies, *e.g.* a river delta deposit, this may advocate the application of some other interpolation model than the linear for estimating property variations between the proximal and distal part of the unit.

Disregarding the possibility of choosing a non-linear function to interpolate between two sample points, still the question regarding the spatial *argument* of the interpolation has to be decided on. The modeller may choose between the horizontal x-parameter and the curvelength s traversed along the correlation line.

As long as the correlation line constantly traverses in one direction laterally, allowing the correlation line to be represented by a functions of the form $z = l\left(x\right)$, property values p along the correlation lines may be given as functions of the horizontal x-coordinate. The properties along the correlation line may thus be given as $p = f_1\left(x\right)$.

The other possible spatial argument for the property functions along the correlation line is the parameter of curve-length. The curvelength along the correlation line from a position (x_0, z_0) to a position (x, z) along the curve defined by $z = l\left(x\right)$ is given by

$$s\left(x\right) = \int_{x_0}^{x} \sqrt{1 + l'\left(X\right)^2} dX \tag{4.1}$$

Since the integrand here is always positive, the s-value of each point along the correlation line is unique. The s-variable may therefore be used as the spatial argument for any property p along the line, defining the function $p = f_2\left(s\right)$. For the actual object, the mapped property is the same regardless of which spatial argument that is used for its representation. Thus

$$p = f_1\left(x\right) = f_2 \circ s\left(x\right). \tag{4.2}$$

However, when interpolating properties between a finite set of samples, the result will generally differ depending on the argument of interpolation. We will now consider the case of interpolating along a correlation line $z = l\left(x\right)$ between two sample points (x_1, z_1) and (x_2, z_2) with property values p_1 and p_2:

A linear interpolation of p with respect to x is given by

$$p_x\left(x\right) = p_1 \frac{\left(x - x_2\right)}{x_1 - x_2} + p_2 \frac{x - x_1}{x_2 - x_1}, \tag{4.3}$$

while a linear interpolation of p with respect to s is given by

$$p_s\left(s\right) = p_1 \frac{s - s_2}{s_1 - s_2} + p_2 \frac{s - s_1}{s_2 - s_1}, \tag{4.4}$$

where s_1 and s_2 are the curvelength parameters corresponding to the horizontal parameters x_1 and x_2 according to equation 4.1. Since s is a function of x, equation 4.4 can be written as

$$p_s(x) = p_1 \frac{s(x) - s_2}{s_1 - s_2} + p_2 \frac{s(x) - s_1}{s_1 - s_2}. \tag{4.5}$$

Now it should be observed that in case the correlation line is straight, *i.e* $z = k \cdot x + a$, the curvelength function $s(x)$ will be linear. As a result, the function $p_s(x)$ will also linear as well. Since $p_x(x)$ and $p_s(x)$ now both are linear functions passing through the identical two sample points, these two functions must be identical. On the other hand, in the case where $z = l(x)$ is non-linear, the curvelength function $s(x)$ and thus $p_s(x)$ will be non-linear as well. The two functions p_s and p_x will thus be different.

Figure 4.6 displays the effect of interpolating linearly with respect to the two spatial variables along a strongly curved horizon. The geometry of the correlation line is displayed in panel a), and the relationship between the x and s parameter calculated on the basis of equation 4.1 is displayed in panel b). Panel c) displays the difference between the predicted parameter values for different x-values. This difference becomes quite large for some parts of the functions. For example, for $x = 100$, the property values differ with approximately 0.03 units, which is 6% of the 0.5 units difference between the two given sample points. In cases of strongly curved correlation lines, the effect of interpolation argument is clearly significant.

Regarding the question of what spatial argument that will produce the most reliable result, there are at least two reasons for preferring the curvelength function. The first reason is based on a geological assumption that many parameters of rocks are determined by the location of the rock at the time of deposition. If a reliable predictive function of *e.g.* lithology properties along the original usually flat layering is available, selecting this parameter as a function of curve length allows the modeller to use the same function to correlate the property values in space if the layers are deformed by folding.

The second reason is that by defining the property function with respect to the traversed length along the correlation line, the geometry of the correlation lines need not to be expressed as a function of the horizontal x-parameter. A more general parameter representation of the lines l in the form $l(t) = (x(t), z(t))$, will also allow lines of more general shape, resembling the shape of *e.g.* overturned folds.

The reason for choosing the opposite option, interpolating with respect to the x-axis, is clearly of economical character. When the curvelength is to be used, for each correlation line the curvelength value given by equation 4.1 must be calculated for the x-locations of the input sample points as well as for

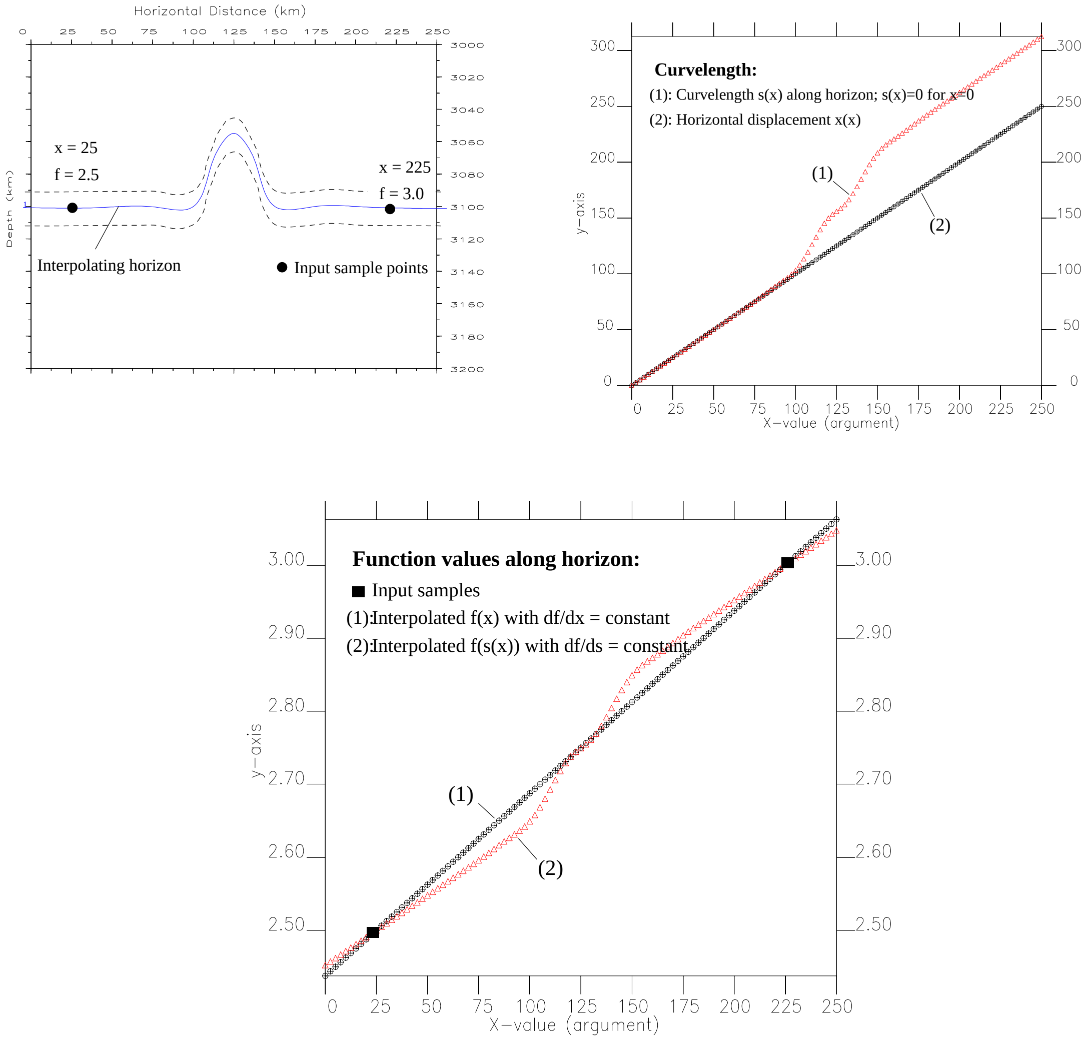

Figure 4.6: The effect of choosing different spatial variables for linear interpolation of parameters

the x-values of the resample points before the interpolation. This calculation clearly delays the execution of the interpolation algorithm, so in cases where the line curving is small, time is saved by using the x-parameter directly.

If more than two samples are given along each correlation line, regardless of what parameter that is the argument of the property functions, it is generally not possible to draw a straight line through the sample values.

A simple interpolating function accounting for a given set of $n+1$ samples is a nth degree polynomials. As we known from calculus, there exist a unique such function for a such a set of sample points. The problem with this is the great oscillations that often occur between the sample points in such polynoms. Generally these functions are also badly conditioned for extrapolating parameter values outside the outermost given samples, especially if a high order function has to be used, quickly approaching plus or minus infinity.

By using composite functions, the oscillations of the nth order polynomals are avoided. On the other hand some discontinuity in the function must be expected, either in the function itself or its derivatives, at the sample points being the connection points between the different functions.

Figure 4.7 displays four given sample values taken in a vertically homogeneous sediment layer. Two lateral composite functions are constructed as interpolating functions. The linear interpolator designed by pulling a straight line between adjacent sample values, is continous, but its first derivative is discontinous where the property gradient changes. A different frequently used interpolation function is the spline, which is the other function displayed in the figure. Like the piecewise linear function, the spline is a composite of different functions whose argument is defined between adjacent samples. The difference is that higher order functions are used, with higher order derivatives also continous at the given samplepoints. A frequently used spline is the cubic splines, composed of third degree polynomials having a continious second derivative at all the jointing points. Requiring the second derivative at the outer points of the composite function to be zero produces the what is termed a *natural* cubic spline, a uniquely determined function defined by the sample points. If the spline requested is not the natural spline, different cubic splines may be generated by setting the tangent slope of the function to specific values at the outermost points.

The referred to figure illustrates that the choosing of a linear composite versus a spline function affects the parameter values to be predicted. Comparing the two, the linear interpolation is surely the most time efficient, but the sharp changes in parameter gradient at the sample points is surely a disadvantage for this procedure.

A significant question occuring in the interpolation step is regarding the assignment of values at locations outside of the outermost borehole measure-

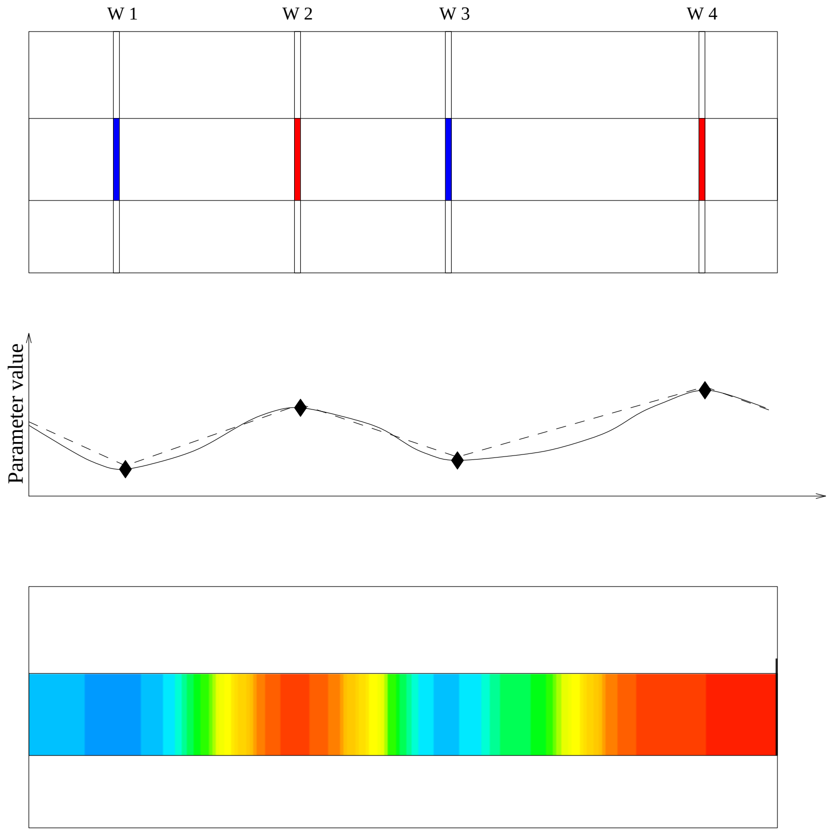

Figure 4.7: Interpolation between well measurements by linear interpolation and a spline function

ments, *i.e.* the issue of extrapolation.

Naturally one possibility is to apply the function that was used for the interpolation between the outermost sample point also for the extrapolation. The problem with this solution is however that the function values of the applied function usually quickly drifts far away from the sampled values. This is especially the case when a high order polynomial is used, as mentioned in the paragraphs above discussing the use of a nth order polynomial for interpolating between $n+1$ samples. The use of such a function for extrapolation, may easily give non-rational values, *i.e.* negative bulk density or velocities.

In the programmed correlation routines, two options of extrapolation are offered to prevent such drift-off.

The first option is to extrapolate to the edges by simply copying the property values of the outer wells to the exterior resampling points. This is similar to the procedure performed on the entire correlation lines in the one-well extrapolation case. If a spline is used to interpolate in the interior of the model, by setting the first derivative of the spline to zero at the outer input samples, the composite constant-and-spline function has a continous first derivative for the entire correlation line.

The other option is to assign some specific parameter value at the lateral edges of the model and include these values to the set of input samples to interpolate in between. By assigning such values, the issue of extrapolation is transformed to interpolation. The equivalent of this assignment is of course to input equivalent well data positioned on the very edge of the model. In such a case the matter of extrapolation vanishes.

The issue of extrapolation is also of interest in the final step of the grid generation, where the skew grid is resampled vertically at the z-values of the requested regular grid. This resampling was displayed in the lower part of panel c) and d) of figure 4.3. In cases such as that illustrated in that figure, where the correlation field does not extend to the top and bottom of the output grid, extrapolation has to be performed. Observing the short distance between the input samples in this step — due to the correlation geometry this distance may be shorter than the sample density of the input wells — and expecting some value difference between these input samples, within a few resample intervals of extrapolation the estimated function values may be be quite different from the range of the input values.

Possible solutions to the drift off in the vertical extrapolation are equivalent to those for the lateral extrapolation, as discussed in the previous paragraphs. These solutions have not yet been implemented in the well correlation program. Initially the vertical extrapolation issue was ignored due to the assumption that the correlation lines with associated well samples would be provided for the area to be gridded. The interpolation example in section 4.5 will show, however, that this assumption do not always hold.

4.4.2 Parameter domain effects

An obvious remark was made in the previous subsection that a linear interpolation of a function and the equivalent interpolation of its logarithm produces quite different results. This observation serves well as an introduction to the issue of which domain to interpolate property parameters in.

A rock at a specific location has different properties related to the different processes, operations or investigations imposed on the object. The rock has a specific mineral composition and texture, from which properties such as density, porosity and permeability, elastic and magnetic properties in theory should be possible to be deduced. The various parameter domains are thus related, since they are deterministic functions of the same actual medium.

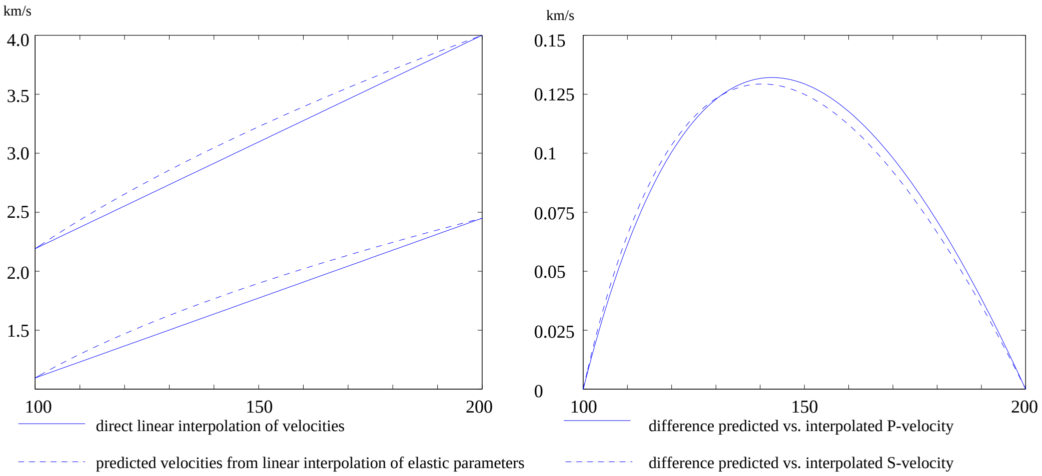

Figure 4.8: a) P- and S-velocity interpolated linearly and predicted from elastic constants linearly interpolated. b) Difference in velocity caused by interpolation method.

Some of the parameter domains may be mapped directly from each other. A known such relationship is that between shear modulus, bulk density and S-velocity in an isotropic homogeneous medium, such as inferred in the second chapter. Other parameters are consided to be independant. For example the porefluid is generally independant of the lithology.

For a set of independent parameters, these are interpolated separately. On the other hand, for any set of dependant parameters, the modeller has to choose which domains to operate on in the interpolation. For example, for the set of related density, shear modulus and S-wave velocity, two of the parameters may be interpolated, while the third is calculated based on the resulting interpolated functions, requiring the relation

$$V_S = \sqrt{\frac{\mu}{\rho}} \tag{4.6}$$

to hold at all sample points.

Since the relationship between the elastic constants and velocities are non-linear for both P- and S-velocity, the result of interpolating velocities linearly compared to that of predicting the velocity from interpolated elastic constants, will differ.

The differences between interpolating in the two parameter domains, are displayed in figure 4.8. Two sample points are given as input at $x_1 = 100$ and $x_2 = 200$. At x_1 the P- and S-velocities are respectingly 2.19 km/s and 1.10

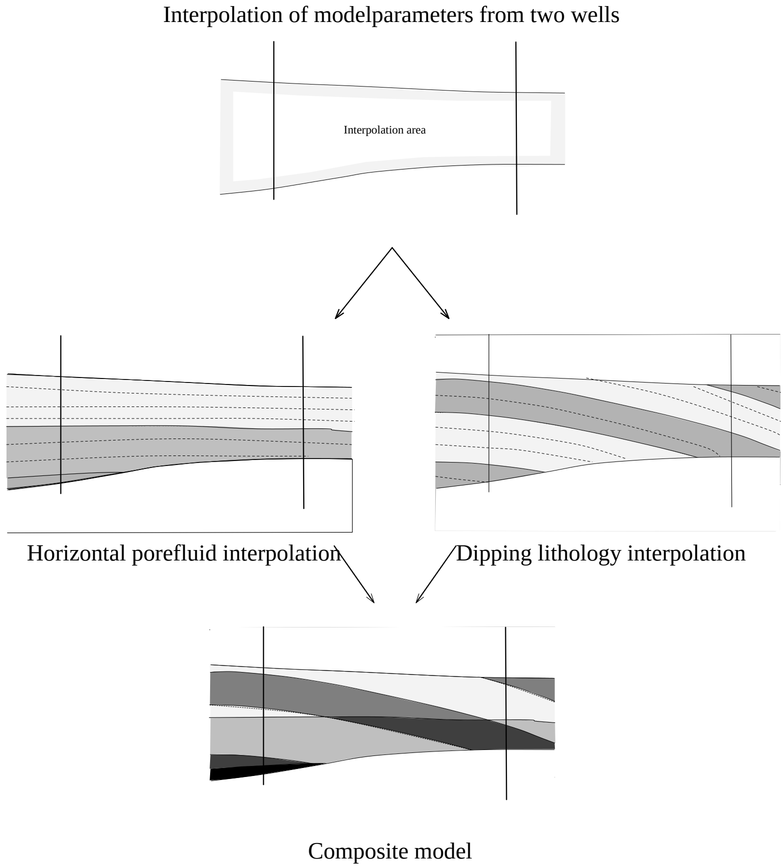

Figure 4.9: Independent parameters may be interpolated along different correlation lines.

km/s, while at x_2 the corresponding values are 4.00 km/s and 2.45 km/s. The density is 2.5 g/cm^3 throughout the model. Panel b) illustrates that the difference between the interpolated velocities and the predicted velocities from interpolated elastic constants, is about 0.13 km/s at the most for the intermediate points, equivalent to 12 % of the total difference in S-velocity between the two given sample points. Thus, clearly the choice of parameters for the interpolation is significant for interpolating along layers with a large difference in property values from one sample location to the other.

When correlating independent properties, such as pore fluid and lithology, even the correlation geometry for the various parameters may be selected independently. The application of such an approach is illustrated in figure 4.9. Here the lithology stratification is dipping while the porefluid has a close to horizontal stratification. Property grids representing these parameters are thus generated separately. As the elastic properties of the object depend on both these properties, the elastic properties cannot be interpolated by correspondingly simple correlation geometry and interpolation functions as those applied for the lithology and pore fluid. Instead, the elastic properties must be calculated as a function of the two mentioned rock domains, generating a composite model, such as the lowermost model displayed in this figure.

A given parameter domain, *e.g.* the P-velocity, is related to a specific scale of measurement. This was covered in the previous chapter, discussing the transformation of parameters from small to large scale. In the current discussion about operating an interpolation in different domains, it is appropriate to look at an example of interpolating on different scales. As stated in the previous chapter, upscaling of a small scale layered isotropic medium produces an anisotropic medium, where the spatial variability is reduced while additional parameters has been added for accounting for anisotropic effects.

The effect of interpolating on the various scales is illustrated in a similar way as that used for illustrating the effect of selecting velocity versus elastic constants as the interpolation domain in figure 4.8. The starting point for the interpolation comparison is a set of wells and correlation lines. The first option is to upscale the wells and then interpolate the upscaled parameters according to some interpolator along the correlation lines. The second option is to interpolated the well at the original given scale. For comparing the effect of the two, the small scale interpolated model must be upscaled, mapping the gridded parameters to the domain of the other model.

Figure 4.10 is a constructed example to illustrate this issue. The model input is two given wells and a horizontal correlation geometry, as displayed in panel a). The two wells are identical, except from a vertical shift equal to the thin layer thickness, causing the high values in one well to correlate with the low values of the other and vice versa. In panel b), an example of the upscaled properties of the two wells are plotted. The medium of the upscaled wells is transversely isotropic, and the properties in the two wells are absolutely identical, since the ratio between the two materials within each input well is identical. Panel c) displays the resulting small scale velocity field by interpolating the input given in panel a). To compare this field with the result of the interpolation of upscaled well data, the property grids are upscaled. The P-velocity of this upscaling is displayed in panel d). As seen here, the velocity increases in the middle of the wells, corresponding to the area where the vertical contrasts in the small scale interpolated medium vanish. The difference in large scale P-velocity between that displayed in d) and the velocity field generated by interpolation of the upscaled properties displayed in b), is displayed in panel e). The anisotropic properties will also differ between the two approaches. The difference in the Thomsen epsilon parameter between the two approaches is displayed in panel f). The decreased vertical contrasts in the middle between the wells in the fine scale interpolation corresponds to the lack of anisotropy in this part.

From this example, it can be concluded that clearly the procedure of upscaling and then interpolating does not produce the same result as that of interpolating and then upscaling.

The exception to this observation is the bulk density. The difference of upscaling the well density log according to Backus smoothing and then interpolate, versus first interpolating and then upscale, is zero, as illustrated in figure g). The reason why the two approaches produce identical results, is that in this case both the interpolation and the upscaling operations of the density parameter are linear. For the other parameters this is not the case, cf. the upscaling formulas of Backus, and thus the results of the two approaches differ.

On which scale, then, should the interpolation be performed? To answer this question, it should be recalled from section 4.3 that the model may have a different correlation geometry on different scales. Thus, if the correlation geometry is drawn from large scale observations, the well data should be given on a corresponding scale.

The given example is really an example of what may happen if the modeller fails to do so. Imagine that the mapped reservoar unit consists of very thin layers of highly contrasted material. The layers are nearly horizontally oriented, except from a tiny structural distortion somewhere between the wells. At the well locations, the dip of layering is measured to be horizontal. This assumption of horizontal layering is also supported by large scale seismic data interpretation over the area. However, the small vertical displacement of the corresponding layers in the two wells leads to a miscorrelation when the large scale horizontal correlation lines are applied on the small scale log data. Contrary, by first upscaling the data before the interpolation, the overall properties, identical in both wells, are correlated correctly, except from not being able to account for for the mentioned small deformation that must be somewhere within the medium.

Large scale properties, resulting from an averaging of small scale properties, are naturally easier to correlate than properties given on small scale. In some cases a rock unit may be considered to be homogeneous on a certain scale, but studied more in detail internal heterogeneities are revealed. The exact function of the variances on small scale may be very chaotic compared to the simple functions describing the large scale properties. Indeed, to interpolate any sedimentary rock on a microscopic scale would be meaningless. The modeller is thus encouraged to interpolate the rock properties on a sufficiently large scale, where the properties are ordered.

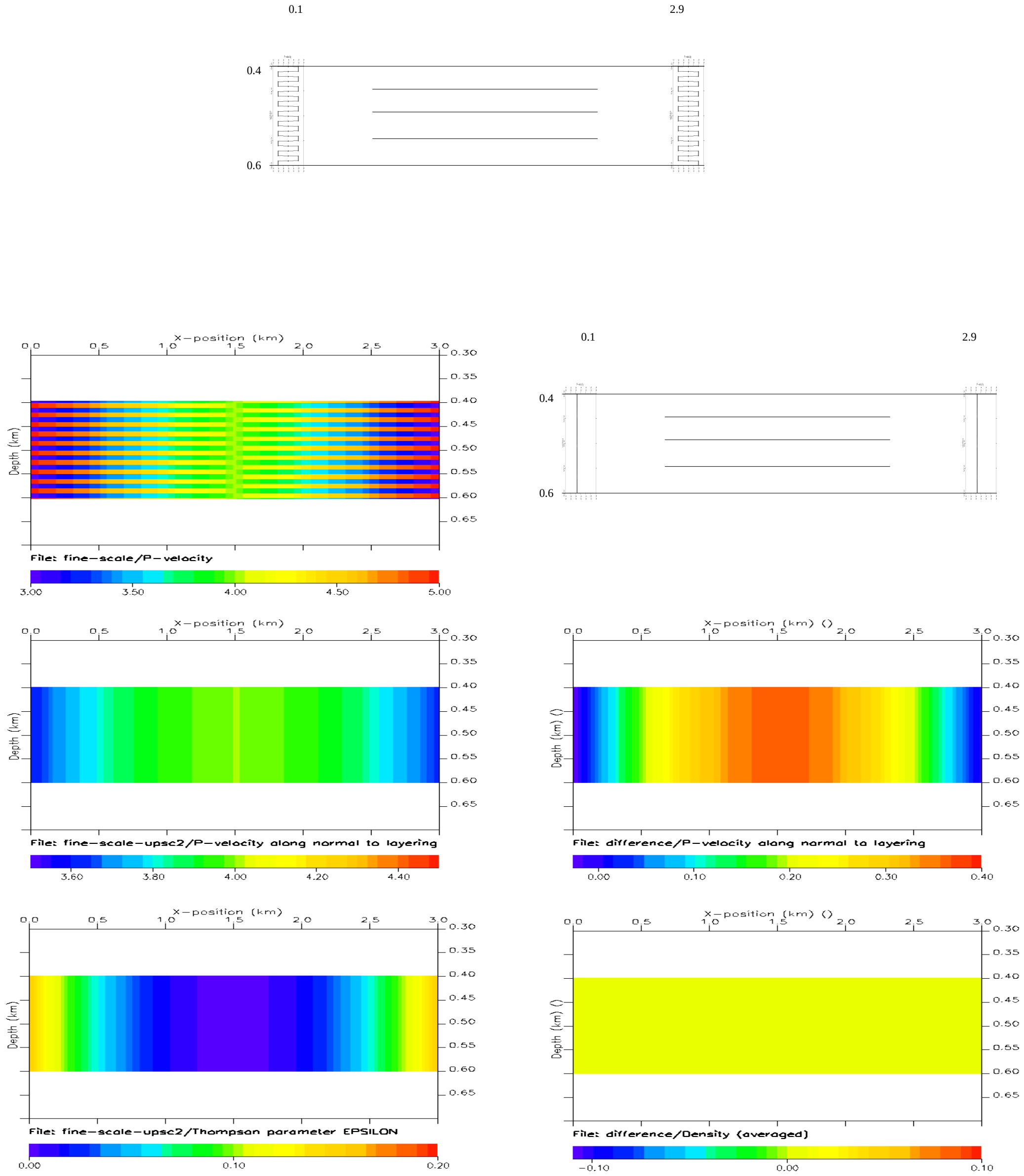

Figure 4.10: A patologic example of the effect of not upscaling before interpolation when log variations are present on a smaller scale than the accuracy of correlation.

On the other hand, all upscaling procedures causes some loss of information content in the given data, as the data is low pass filtered as part of the process. With respect to the purpose of the generated model, *i.e.* a seismic survey simulation, the information loss may be compensated by including additional parameters, such as the anisotropic Thomsen parameters. But still, the filtering makes the upscaling transformation non-reversable, *i.e.* the large scale properties are unique functions of the small scale properties while the opposite functions are underdetermined. Thus, the small scale properties cannot be uniquely estimated from the large scale representation. Since an infinite number of different small scale models may have identical large scale property values in some domain, *e.g.* that of elastic constants, while the same set of small scale models may produce a wide range of different property values in a different large scale domain, a transformation of parameters from one large scale domain to another, without additional knowledge about the small scale model, in most cases is not possible.

To produce a model that both agrees with measured data, *e.g.* a seismic survey, and that is reliable for prediction of properties in different domains not yet measurable, *e.g.* the production parameters of a reservoir not yet in production, the model should thus be constructed in the most fundamental parameter domain available. A small scale model, describing every tiniest feature unambiguously, from which all parameters in any domain could be calculated, would be the ideal, except from the unmanagable size of information such a description would require.

My suggested answer then to the question of what scale to interpolate and represent a model in, is to encourage a balance between on the one hand keeping the model on a fine scale, permitting subsequent unique transformations to the different large scale domains for various simulation purposes, and on the other hand performing the interpolation on a sufficient large scale to trust the hypothesis of correlation geometry and the validity of the selected interpolating functions.

4.5 An illustrative example

Many of the issues discussed in the previous sections, regarding correlation geometry, vertical extrapolation of properties, and scale and domain of interpolation, will be illustrated in a final constructed example.

The input data and different grids generated in the interpolation process are illustrated in figures 4.11 and 4.12.

The model to be generated is 100 meters wide and 35 meters deep.

Well data are provided from two vertical wells, each located five meters from the edges of the model, containing density, P- and S-velocity and dipmeter data for the entire vertical range with a sampling interval of 12.5 cm. The model is interpreted to consist of two different units. The upper unit ranging from 500 to 507 meters, while the lower from 507 to 535 meters. The two units are recognized in the well data by the character of property values and the dip of layering. Dipmeter logs indicate horizontal layering for the upper unit in both wells, while the lower unit is dipping down to the right in the left well, and down to the left in the right one. From the density data displayed in panel a) in figure 4.11, it can be observed that the property values in the upper part is more constant and generally lower than in the lower part of the model.

From interpreting the well data, the natural assumption is that the upper section is horizontally layered, while the lower section represents a syncline. Geometric information from seismic interpretation supports the horizontal assumption of the upper section, while structural information from seismic data indicates that the intermediate part of the lower section actually consists of two synclines separated by an anticline. The dividing interface between the two units is a horizontal unconformity. Thus the correlation geometry of the object is fully given by the two plotted lines in panel a). The straight upper line defines the unconformity interface between the two units and the corrrelation geometry of the upper section. Below this interface the correlation field is parallel to the curved lower line.

Since the object to be modelled consists of two separate units, the interpolation of the units should be performed independently. The generated parameter fields of the lower region should not be affected by the correlation lines and well data of the upper section and vice versa. Thus, only the well data from 500 to 507 meters and the horizontal correlation line is used as input for the interpolation of the upper part of the object, while the log segments below and the curved correlation line are used in the other interpolation procedure. The resulting grids are then spliced at the given interface at 507 meters.

The combined density grid from the two separate interpolation operations is displayed in panel b) in figure 4.11. Visually this grid clearly reflects the assumed correlation geometry. However, in the core of the synclines, the calculated properties appear to drift off from the property values in the given wells. The reason for this is the vertical extrapolation involved in assigning values to this area. In panel a) the reason for this becomes evident. The uppermost correlation line in the lower section that intersects both the corresponding segments of the wells, is the curved line displayed in this panel. This line thus represents the upper limit of the correlation field in the interpolation of the lower section, cf. the discussion of the extent of the correlation field in section 4.3. The values above this line are thus not directly corrrelated to the well data, but rather a result of an extrapolation of the skew grid in the last step of the generation of a regular grid. The problems with such extrapolation was discussed in the last part of section 4.11. In this case no constraints are put on this extrapolation, resulting in rather extreme values below the horizontal interface and above the displayed curved correlation line. The values here do not correspond with the expected medium properties, which are assumed to be similar to that of the underlying material.

At least three possible solutions exist to improve the model representation in the discussed area.

One solution is based on the assumption that the lower section has been eroded prior to the sedimentation of the upper section.

A reconstruction of the wells above the erosional surface to their pre-erosion state thus provides the necessary well data to extend the correlation field to also cover the internal upper part of the lower section.

Of course this extrapolation of well segments is not bound to succeed. Observing the variances in the lower sections of the two logs plotted in figure 4.11 a), to predict exactly how these sections should be extended upwards is not trivial. Both wells contain large scale trends in the data, as well as local variability, which have to be considered to produce a tenable pre-erosion model.

However, this process involves the extrapolation of only a couple of wells, which can be performed manually by a "copy and paste" procedure. Compared to letting a computer automatically perform an extrapolation on every column in the skew grid later in the correlation procedure, this manual extrapolation of the wells is preferable.

Figure 4.11 c) displays the result of assigning constant values to the top of the lower segments before interpolating. Clearly the failure to include the local variability in the well-log extrapolation produces an interpolated medium of a different character than the case would be if this variability is incorporated. While most of the lower model has a thin-layered appearance, that behaves like a transverse isotropic medium when propagated by low frequency waves, the generated "patch" to replace the mentioned vertically extrapolated values remain isotropic also for long wave-lengths.

This problem of getting a differing anisotropy property in the part of the unit that cannot be correlated directly from the original well data, can be avoided by upscaling the well log segments prior to the extension of these and following correlation. The low spatial frequencies contained in the upscaled data may more easily be extrapolated than the high frequency variations in the original data when extending the wells vertically.

Interpolating the upscaled and then vertically extrapolated wells along the correlation field generates a grid with similar properties in the entire unit, which is more what is requested than the state aquired in figure 4.11 c).

Figure 4.12 a) displays the density grid aquired by upscaling the well log segments by averaging over the entire intervals in the wells. The resulting log segments are then constant, making it trivial to extend the lower log-segments sufficiently upwards before the interpolation.

When correlating these upscaled well data, as noted in section 4.3, we might also choose a different correlation geometry than the one given by the curved horizon in figure 4.11 a). On large scale, a natural choice for the correlation geometry would be parallel to the horizontal interface, for two reasons. First, but not most importantly, the small scale curved correlation line might be interpreted as oscillating about the horizontal line, thus on a sufficient scale the correlation line may be considered to be straight. Second, when the wells are upscaled to the scale of no vertical variations within the layers, cf figure 4.12 a), and the interface between the two layers is horizontal, the partial derivative of the properties in the z-direction will be zero within the layers. Thus the natural choice of correlation geometry in this case will be in the direction parallel to the horizontal interface. Indeed, selecting an interpolation of property values along the curved correlation field, with the x-axis as the interpolator argument, cf. section 4.4.1, produces exactly the equivalent property field as interpolating linearly along a horizontal correlation field. By choosing the horizontal large scale interpolation geometry, there is no need to vertically extrapolate the lower well segments prior to correlation.

The Thomsen anisotropy parameters resulting from the upscaling of the provided wells are plotted in panel b) of figure 4.12. The grid in this panel displays the horizontally interpolated Gamma parameter, showing the relationship between shear wave velocities parallel and perpendicular to the symmetry axis of the medium.

The orientation of the symmetry axis in the 2D modelling case may be represented in a separate grid, plotting the angle of inclination between the vertical axis and the symmetry axis. The medium of the upper section, interpolated horizontally on both small and large scale, clearly has a vertical symmetry axis. Regarding the lower unit, a strong simplification would be to assume the symmetry axis to be vertical. However, if the oscillations in the small-scale geometry were smaller compared to the overall scale, this assumption might be justified. A second, and most accurate assumption, is to assume that the symmetry axis of the lower unit is perpendicular to the small scale undulating correlation field. A grid of this parameter is already produced in the process of generating the grid in figure 4.11 b). The inclination field is plotted in figure 4.12 c), where positive values indicate a dip down to the left, *i.e.* a rotation of the horizontal layering in the counter-clockwise direction.

Now imagine the different situation that the only input for the model construction is the two wells with its two correlated sections. In this case the correlation horizons displayed in 4.11 are not provided, and the only information about the layering orientation is given by the dipmeter logs. On large scale, the parameters may still be interpolated horizontally, but in this case, the orientation of the symmetry axis of the transverse isotropic medium between the wells is not given explicitly. In this case the symmetry orientation also has to be interpolated, and clearly, this interpolation will fail to represent the hidden crest between the wells. The best interpretation would be to assume the sediments to form a single syncline between the wells, constructing a simple curve, *e.g.* a parabola, to fit the positions and layering dip of *e.g.* the uppermost samples in the lower section, and use this line as the basis for determining the inclination of the symmetry axis. A different and more simple approach, is to interpolate the symmetry inclination values in the same manner as the other property values. Figure 4.12 d) shows the result of interpolating the inclination angle of the symmetry axis of the transverse isotropic upscaled wells linearly with respect to the x-axis between the wells. In such an interpolation, the choice of parameter to be interpolated and what interpolator function to be used is again an issue. That line is thought is not pursued here, however.

To conclude this section, three possiblities for interpolating the well data has been presented:

1. The data is interpolated on small scale according to the correlation geometry supplied from seismic interpretation. The resulting grids may subsequently be upscaled.

2. The data is upscaled before interpolation. While the symmetry orientation of the upscaled medium is given by the small scale correlation geometry, the large scale data may be interpolated horizontally according to a large scale correlation geometry.

3. Both the rock properties as well as the symmetry orientation are interpolated according to the large scale correlation geometry.

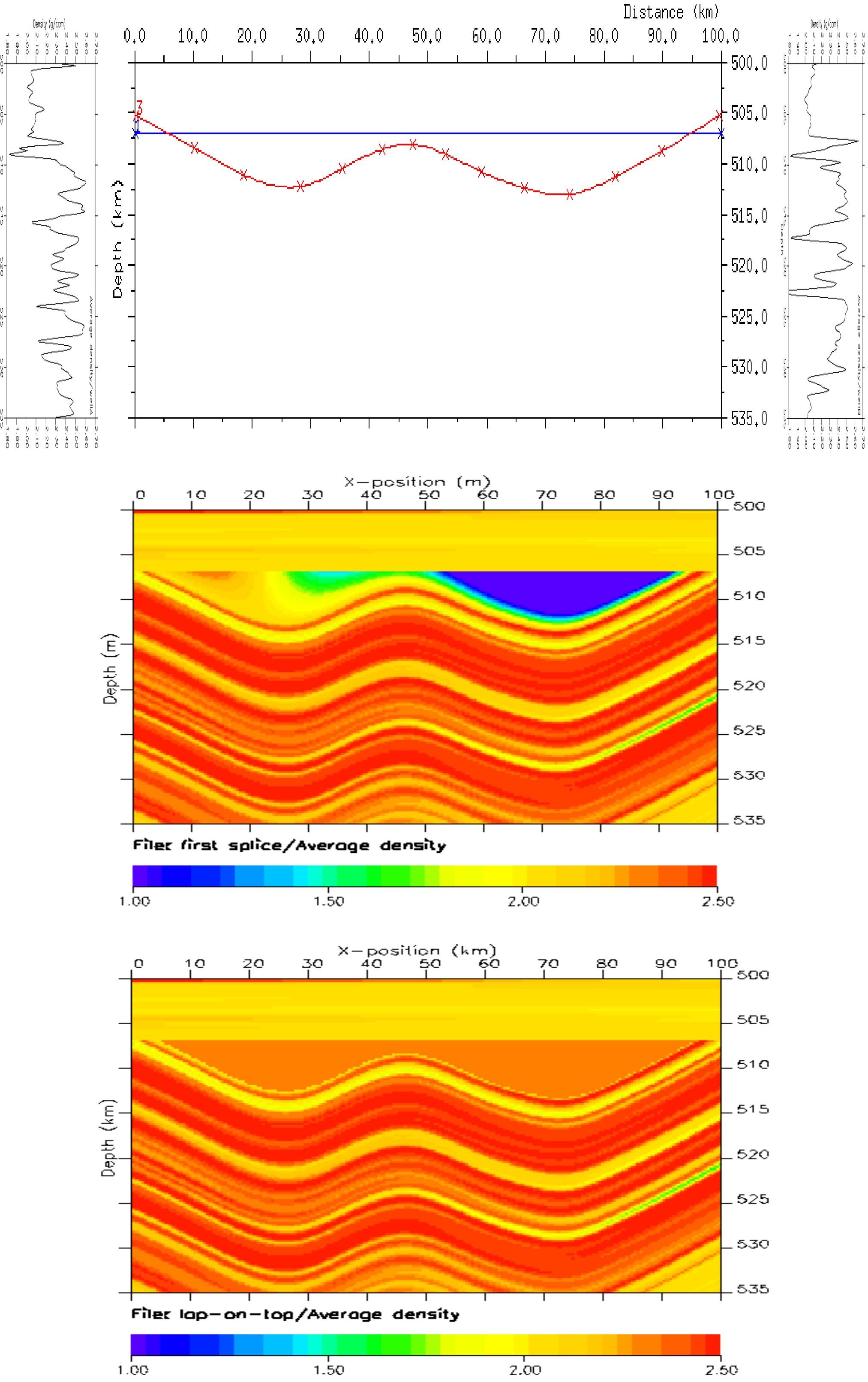

Figure 4.11: Interpolation between two wells without upscaling

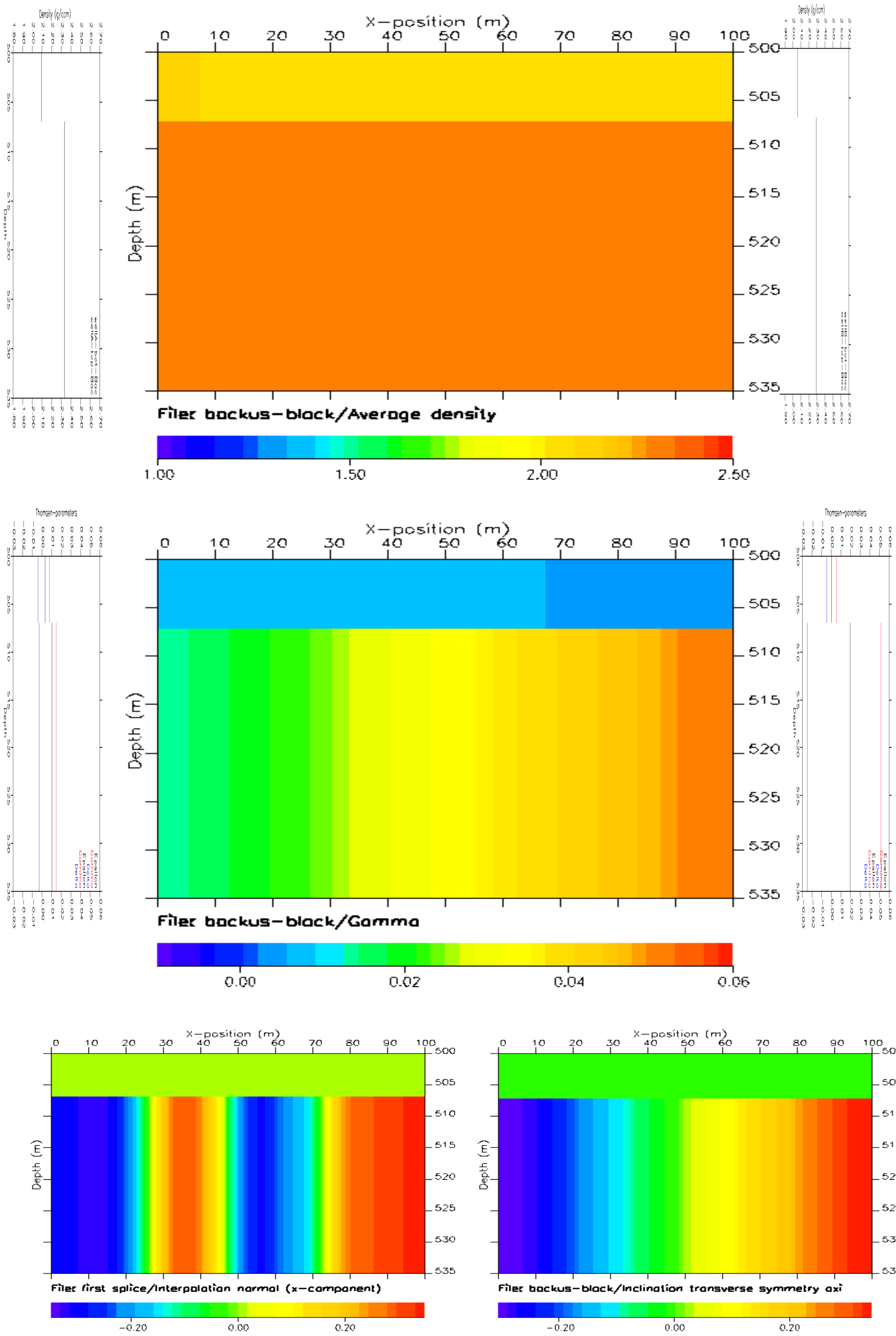

Figure 4.12: Horizontal interpolation of upscaled wells.

4.6 Conclusions

The theme of this chapter has been to correlate property values from locations of given data to locations with no measurements. The correlation is based on a set of well data and geometric information.

The conceptual basis for the interpolation is the assumpton of stratification. Though a real object might not be unambiguously layered on all scales, this principle is useful for correlation of properties laterally between separated wells.

The principles of a general correlation routine have been presented. The following correlational parameters are seen to affect the resulting model:

1. Correlation geometry:
    - Different correlation geometries reflects different sediment patterns, cf. figure 4.4.
    - The proper correlation geometry is scale dependent and may also be property domain dependent.
    - The shape of correlation geometry and the requested sampling density combined may require upscaling of data to prevent aliasing.
2. Interpolation function, *i.e.* the parameter domain and interpolator type. Different aspects here are:
    - The choice of parameter domain used as spatial argument for the property functions. When interpolating along a curved correlation line, the selection of horizontal x-coordinate versus curvelength s-coordinate as argument for the interpolation, may produce property differences at intermediate locations exceeding a tenth of the value difference between given input samples.
    - The choice of interpolator. Among an infinite number possible functions, two functions have been considered — the linear and spline function.
    - The choice of independent parameter domain to interpolate on, from which other rock properties are calculated. Interpolating elastic constants and then calculate velocities versus interpolating seismic velocities directly, using the same interpolator, may produce velocity differences at intermediate locations up to a tenth of the total velocity difference of the input samples.

- The relationship between property domain of interpolation and correlation geometry. The property domains with simple correlation geometries and functions should be selected.
- The choice of scale for parameter representation. The resulting model from interpolating on small scale and consequently upscaling versus interpolating already upscaled parameters may significantly differ.

Chapter 5

The main conclusions

The objective of the present work has been to estimate the effect of different upscaling and interpolation functions for assigning property values to a spatial seismic model on the scale appropriate for large scale seismic modelling. In addition to pointing to differences between the procedures, for the upscaling case my goal has been to find the upscaling functions that most accurately reproduce the behaviour of the small scale medium. This evaluation involves simulations of wave propagation, which require an understanding of the fundamentals of elasticity and wave field propagation in simplified media.

The necessary theory of elasticity was covered in chapter two, while upscaling and interpolation were discussed in chapter three and four respectively.

An important observation in chapter three concerned the validity of the proposed upscaling functions as a function of the wavelength to layer thickness ratio. The studied alternative functions either produced isotropic upscaled media by smoothing on seismic velocities, slownesses, wave modulii (Voigt averaging) or their inverse (Reuss averaging), or produced transverse isotropic media by Backus averaging. For thin-layered models with large λ/d-ratio (larger than 10), the Backus smoothed medium by far gave the best representation, especially for waves propagating non-parallel with the associated symmetry axis. However, for waves propagating normal to the layering, the Reuss averaged isotropic model also gave a good estimate of the wave velocity. For smaller λ/d-ratios, the slowness averaged medium gives the best large scale representation of the wavefield. It is also observed that since the S-wave has a smaller wavelength than the P-wave, the large scale models appropriate for modelling the P-wave may give wrong large scale properties for the S-wave and conversely.

The other important observation is from the experiment of two-step upscaling, where the small-scale medium was first upscaled to an intermediate scale, before being upscaled to a large scale. The observation here is that the upscaling procedure used on the smallest scale upscaling strongly affects the consequent large scale model. This must be taken into concideration when actual measurements or samples are taken of a medium, because any sampling involves some kind of upscaling of heterogeneities on a finer scale. For example, ignoring the transverse isotropy of the small scale medium will give notably different upscaled properties.

From chapter four a main observation is that the choice of parameter domain used to interpolate parameters, *e.g.* interpolating elastic properties in the seismic velocity domain versus in the stiffness tensor domain, causes the interpolated properties to differ at intermediate locations with up to 10 % of the difference in property values between the sample points being interpolated between. This raises serious questions regarding which domain that is the most appropriate to interpolate in. A similar observation is that the choice of scale for the parameter representation may affect the resulting interpolated model. For different scales, different correlation orientations may even be appropriate.

Both these chapters show that choices made when constructing a large scale model from a small scale parameterization of and spatially constrained data, considerately affects the large scale properties of the model. In *e.g.* reservoir monitoring, an accurate velocity parameterization is required for the successful use of the constructed model, and the issues of model construction should therefore be given its deserved attention. The large scale anisotropy caused by large λ/d-ratios between the propagating wave and the sediment structures, also has significance when interpreting data in a seismic survey, for example for AVO-analysis and depth conversion. A calculated depth with an error of 20 m may sometimes be crucial.

This thesis contains some loose threads that call for further investigations. For example, wave simulations should be performed in a model based on original and upscaled non-synthetic data to study the effect of different window shapes in the upscaling procedure by comparing wave fields. Related to this I would also suggest performing Backus smoothing on the transverse isotropic intermediate scale models to validate the relations between one- and two-step Backus upscaling. Someone woul maybe also like to look into the reasons why the Backus averaged well data in a few cases has a negative epsilon Thomsen parameter, which seems very peculiar. Regarding interpolation issues, now being aware of the effect of interpolating in different parameter domains, it would be natural to look more into aspects of interpolating *geologic* rock properties and study similar effects of variations by interpolating method in this set of domains.

Bibliography

[1] A. E. Adams, W. S. MacKenzie, and C. Guilford. *Atlas of sedimentary rocks under the miroscope.* Longman, Harlow, 1984.

[2] K. Aki and P. G. Richards. *Quantitative seismology: Theory and methods.* W. H. Freeman and Company, San Francisco, 1980.

[3] B. A. Auld. *Acoustic fields and waves in solids.* Robert E. Krieger Publishing Company, Malabar, 1990.

[4] G. E. Backus. Long-wave elastic anisotropy produced by horizontal layering. *Journal of Geophysical Research*, 67(11):4427 – 4440, 1962.

[5] O. Dubrule, M. Thibaut, P. Lanny, and A. Haas. Geostatistical reservoir characterization constrained by 3d seismic data. *Petroleum Geoscience*, pages 121 – 128, 1998.

[6] H. H. Haldorsen and T. V. Golf-Racht. Reservoir management into the next century. In R. E. Sheriff, editor, *Reservoir Geophysics*, pages 12 – 24. Society of Exploration Geophysicists, Tulsa, 1992.

[7] M. Haveraaen, H. Friis, and T. A. Johansen. Formal software engineering for computational modelling. *Nordic Journal of Computing*, pages 241 – 270, 1999.

[8] K. Helbig. Anisotropy and dispersion in periodically layered media. *Geophysics*, 49:364 – 373, 1984.

[9] K. Helbig. *Modeling the earth for oil exploration: Final report of the CEC's GEOSCIENCE I program.* Pergamon, Oxford, 1994.

[10] J. A. Hudson. Overall properties of heterogeneous material. *Geophys. J. Int.*, 107:505 – 511, 1991.

[11] E. H. Isaaks and R. M. Srivastava. *An introduction to applied geostatistics.* Oxford University Press, New York, 1989.

[12] T. A. Johansen. *Seminarserie: Bergartsfysikk.* Institute of solid earth physics, University of Bergen, 1997.

[13] H. D. Johnson and D. E. Krol. Geological modelling of a heterogeneous sandstone reservoir: Lower jurassic statfjord formation, brent field. Technical report, Paper SPE 13050, 1984.

[14] A. G. Journel. *Fundamentals of geostatistics in five lessons.* American Geophysical Union, Washington, D.C, 1989.

[15] A. K. Kvalheim. *Eksperimentell og numerisk studie av anisotropi i lagdelte materialer.* Institutt for den faste jords fysikk, Universitetet i Bergen, 1997. Cand. Scient. Thesis.

[16] G. M. Laslett. Kriging and splines: An empirical comparison of their predictive performance in some applications. *J. Acoust. Soc. Am.*, pages 391 – 400, 1994.

[17] D. Marion, T. Mukerji, and G. Mavko. Scale effects on velocity dispersion: From ray to effective medium theories in stratified media. *Geophysics*, 59(10):1613–1619, 1994.

[18] G. Mavko, T. Mukerji, and J. Dvorkin. *Rock physics formulas.* Stanford University, Stanford, 1993.

[19] W. Menke. *Geophysical data analysis: Discrete inverse theory.* Academic press, Inc., 1984.

[20] E. Mæland. *Signalteori.* Institutt for den faste jords fysikk, Universitetet i Bergen, 1993.

[21] R. F. O'Doherty and N. A. Anstey. Reflections on amplitudes. *Geophys. Prosp.*, 19:430 – 458, 1971.

[22] M. S. Sams and P. R. Williamson. Backus averaging, scattering and drift. *Geophysical prospecting*, pages 541 – 564, 1994.

[23] H. Stark, F. B. Tuteur, and J. B. Anderson. *Modern electrical communication.* Prentice Hall, New Jersey, 1988.

[24] R. H. Tatham. V_p/V_s and lithology. *Geophysics*, 47(3):336–344, 1982.

[25] L. Thomsen. Weak elastic anisotropy. *Geophysics*, 51(10):1954–1966, 1986.

[26] D. F. Winterstein. Velocity anisotropy terminology for geophysicists. *Geophysics*, 55(8):1070 – 1088, 1990.

[27] J. M. Yarus and R. L. Chambers. *Stochastic modeling and Geostatistics: principles, methods and case studies.* American Association of Petroleum Geologists, Tulsa, 1994.